申请上海交通大学硕士学位论文

低能核反冲在液氙暗物质探测器中的发光和电离效率

论文作者 慕　巍

学　　号 1110729003

指导教师 季向东　教授

专　　业 物理学

答辩日期 2014 年

Submitted in total fulfilment of the requirements for the degree of Master in Physics

Scintillation Efficiency and Ionization Yield of Low Energy Nuclear Recoils in Liquid-Xenon Dark Matter Detection

Mu Wei

Supervisor

Prof. Ji Xiangdong

Depart of Physics and Astronomy

Shanghai Jiao Tong University

Shanghai, P.R. China

Mar. 2014

上海交通大学
学位论文原创性声明

本人郑重声明：所呈交的学位论文，是本人在导师的指导下，独立进行研究工作所取得的成果。除文中已经注明引用的内容外，本论文不包含任何其他个人或集体已经发表或撰写过的作品成果。对本文的研究做出重要贡献的个人和集体，均已在文中以明确方式标明。本人完全意识到本声明的法律结果由本人承担。

学位论文作者签名：_____

日　期：_____年 ____月 ____日

上海交通大学
学位论文版权使用授权书

本学位论文作者完全了解学校有关保留、使用学位论文的规定，同意学校保留并向国家有关部门或机构送交论文的复印件和电子版，允许论文被查阅和借阅。本人授权上海交通大学可以将本学位论文的全部或部分内容编入有关数据库进行检索，可以采用影印、缩印或扫描等复制手段保存和汇编本学位论文。

保　密 □，在 _____ 年解密后适用本授权书。

本学位论文属于

不保密 □。

（请在以上方框内打“✓”）

学位论文作者签名：_____　　指导教师签名：_____

日　期：_____年 ___月 ___日　　日　期：_____年 ___月 ___日

低能核反冲在液氙暗物质探测器中的发光和电离效率

摘　　要

大质量弱相互作用粒子（weakly interacting massive particles WIMPs）是目前暗物质粒子的最具吸引力的候选之一。近二十年来，无数暗物质探测实验被开发用于 WIMPs 粒子的直接探测。其中，液氙探测器是所有直接探测试验中最有希望的一种。液氙探测器用来探测暗物质粒子（WIMPs）与探测器中原子发生弹性散射作用所引起的核反冲，从而达到对暗物质粒子的直接探测的目的。当液氙探测器中的某个氙原子与暗物质粒子发生弹性散射，该原子会获得大约几到几十千电子伏特（keV）的动能成为一个反冲原子。反冲原子在探测器介质中运动并减速，在此期间会激发或者电离探测器中其他原子，产生实验中容易探测到的瞬时发光信号（以下简称为发光信号）S1 或者电离正比发光信号（以下简称为电离信号）S2。其中发光信号是由激发电子退激发，或者被电离电子与负离子重新结合并退激发而产生，而电离信号则是由于被电离的电子在外加电场作用下，漂移到气态探测器室中而产生。

在液氙探测器中，有两个重要的参数，即相对发光效率（relative scintillation efficiency $\mathcal{L}_{\text{eff}}$）和电离效率（ionization yield $\mathcal{Q}_{\text{y}}$）。这两个参数有效地的将实验易探测到发光信号 S1 或者电离信号 S2 与暗物质粒子（WIMPs）在探测器中原子反冲的初始能量联系起来。如果 $\mathcal{L}_{\text{eff}}$ 或者 $\mathcal{Q}_{\text{y}}$ 能够精确的计算出来，那么结合实验对原子反冲所产生的发光信号 S1 或者电离信号 S2 测量，实验学家可以重构原子反冲的能量，从而对暗物质粒子的相关性质进行进一步分析。原则上讲，$\mathcal{L}_{\text{eff}}$ 和 $\mathcal{Q}_{\text{y}}$ 可以通过实验进行测量。然而这项任务在低能原子反冲区却很有挑战性。大多数实验通过中子源来产生核反冲，从而模拟暗物质粒子产生的原子反冲信号来测量 $\mathcal{L}_{\text{eff}}$ 和 $\mathcal{Q}_{\text{y}}$，但是实验的性质决定了核反冲的能量越低（keV 能量区域附近），该实验的系统误差就会越大。同时，由于轻暗物质粒子（WIMPs）的质量多数在几个吉电子伏特（GeV）左右，其产生的原子反冲

能量多数在数个千电子伏特（keV）。针对这种情况，本文对液氙探测器在低能区的发光和电离过程进行了详尽的研究和理论分析，并且对 $\mathcal{L}_{\rm eff}$ 和 $\mathcal{Q}_{\rm y}$ 在低能区的行为做出了相应的理论预测。

基于 Lindhard 的基本积分方程以及二体碰撞模型，我们开发了一个计算机程序来模拟原子反冲在液氙探测器中的减速过程。利用该程序，我们可以计算出原子反冲在减速过程中的电子能损的具体数值。通常来说，这个数值与原始原子反冲能量的比值被称为 Lindhard 系数（Nuclear Quenching Factor $q_{\rm nc}$）。从而可以进一步来计算发光信号和电离信号的数量。为了得到 $q_{\rm nc}$ 在低能区的精确值，我们对低能区的氙原子在液氙介质中的电子能损的过程，现存的理论模型，以及实验数据进行了分析，对传输截面法（Transport Cross Section）求电子能损 S_e 的方法做了修正，从而重新计算了 S_e。我们的理论结果与中等能量区域（40 到 100 千电子伏特）的实验结果符合得很好。为了进一步计算光信号和电离信号的数值，我们对电子与负离子的结合过程进行了分析，修正并推广了现有的 Thomas-Imel 模型。通过该修正，我们预测了电子与负离子在外场下的结合效率，从而能够精确计算出发光信号和电离信号的数值。

将我们所做的研究结合起来，我们得到 $\mathcal{L}_{\rm eff}$ 和 $\mathcal{Q}_{\rm y}$ 在低能区的理论预测值。我们对 $\mathcal{L}_{\rm eff}$ 和 $\mathcal{Q}_{\rm y}$ 的理论预测与中子散射实验的测量结果符合的很好。在无实验数据区域（低于 3 千电子伏特的区域），我们所预测的 $\mathcal{L}_{\rm eff}$ 迅速降低。该现象与之前文献中所做的假设相矛盾。我们所预测的 $\mathcal{Q}_{\rm y}$ 随着原子反冲能量的降低而升高，在 2 到 3 千电子伏特的区域达到最大值。这个预测结果可以将探测器的探测极限进一步降低到大约 1 千电子伏特左右。由于电离信号相对易于探测，该预测有可能被实验进一步证实或者证伪。

关键词： 液氙探测器　暗物质　发光效率　电离效率

Scintillation Efficiency and Ionization Yield of Low Energy Nuclear Recoils in Liquid-Xenon Dark Matter Detection

ABSTRACT

Liquid xenon (LXe) detectors, among many direct detection experiments which have been proposed and run in the last two decades, have shown particular promising in the detection of weakly interacting massive particles (WIMPs), an attractive candidate for Dark Matter (DM), by observing the atomic recoils after WIMPs' elastic scattering on nuclei. The elastic scattering will produce a recoiling xenon atom, also called nuclear recoil, with kinetic energy up to a few tens keV. It excites and ionizes xenon atoms, giving rise to scintillation signals S1 through the de-excitation of excitons and recombination of electron-ion pairs, and ionization signals S2 through the electrons escaping from recombination, respectively.

Two crucial properties of LXe detectors are the so-called relative scintillation efficiency $\mathcal{L}_{\text{eff}}$ and ionization yield $\mathcal{Q}_{\text{y}}$, which serve as bridges between the detected S1 and S2 signals and the deposited energy of the WIMPs in LXe detector. $\mathcal{L}_{\text{eff}}$ or $\mathcal{Q}_{\text{y}}$, together with the detected S1 or S2 signals, is used to reconstruct and calibrate the initial nuclear recoils energy, hence study the properties of the WIMPs. The biggest challenge for experiments to measure $\mathcal{L}_{\text{eff}}$ and $\mathcal{Q}_{\text{y}}$ lies in very low energy nuclear recoils, particularly at the detection threshold, where most of the recoiling events will be if the mass of WIMPs is around several GeV/c^2. In this thesis,the LXe scintillation and ionization process are analyzed in details and a state-of-art theoretical analysis of the $\mathcal{L}_{\text{eff}}$ and $\mathcal{Q}_{\text{y}}$ in the very low energy region has been performed.

Based on Lindhard's basic integral equation and the binary collision approximation, a computer program, which reflects our understanding on the slowing down process of the recoiling nucleus in liquid xenon, is developed to calculate how much nucle-

ar recoil energy is dissipated to electrons in the medium, hence produces scintillation and ionization signals at last, which is the so-called nuclear quenching factor $q_{\rm nc}$ or Lindhard factor. To obtain an accurate nuclear quenching factor at low energy region, existing theoretical models and experimental data for electronic energy dissipation: electronic stopping power S_e, are reviewed and analyzed. We improve transport cross section method and re-calculate the electronic stopping power at low energy region. The theoretical prediction for S_e in liquid xenon agrees with the experimental data very well. To evaluate the electron-ion pair recombination rate, the different behaviors for the electron-ion pair recombination process regarding electron recoils, alpha recoils, and nuclear recoils, are studied and the Thomas-Imel box model is generalized to describe the recombination behaviors regarding nuclear recoils. At last the recombination rate can be expressed as a function of nuclear recoil energy and the applied electric field.

Combining the electronic energy dissipation from the computer simulation and the generalized Thomas-Imel box model, we predict the $\mathcal{L}_{\rm eff}$ and $\mathcal{Q}_{\rm y}$ at low energy region. The predictions from this work agree well with the measured $\mathcal{L}_{\rm eff}$ and $\mathcal{Q}_{\rm y}$ from the neutron scattering experiments. The predicted $\mathcal{L}_{\rm eff}$ suggests a rapid drop when the recoiling energy comes below 3 keV where authors have pointed out the liquid xenon scintillation response should drop steadily at low energy. The predicted $\mathcal{Q}_{\rm y}$ increases with the decreasing of the recoiling energy and reaches the maximum value at 2$\sim$3 keV, which may be examined by experiment in the future and lower the energy threshold for nuclear recoils to $\sim$1 keV.

KEY WORDS: Liquid Xenon, Dark Matter, Scintillation Efficiency, Ionization Yield

目　　录

表格索引

插图索引

第一章　暗物质和液氙探测器对 WIMP 暗物质粒子的直接探测

伊萨克牛顿爵士发表了他的经典著作 “Philosophiae Naturalis Principia Mathematica” 之后，无数科研工作者为了探索宇宙的奥秘而努力。在过去的一个多世纪里，随着理论与技术方面的进步，物理学家们有更多机会来研究最微观和最宏观的世界：粒子物理和天体物理。通过理论物理学家和实验物理学家的努力，粒子物理的标准模型已然对基本粒子物理领域做出了精确的预测。与之相似，在天体物理方面，结合广义相对论的预测，通过实验对一些重要天文现象的观测，诸如银河系悬臂的旋转速度（galactic rotation curves），弱引力透镜（weak gravitational lensing），宇宙微波背景辐射（cosmic microwave background (CMB)），宇宙大尺度结构（Large Scale Structure (LSS)），以及 Ia 型超新星的观测（type Ia supernovae observations） [1–5]，天文物理学家们对宇宙现象也给出了一个标准模型。在这个标准模型中，所有的实验观测都显示，在现存的宇宙中存在大量的无法通过电磁作用直接观测的物质或者能量。结合理论预测和实验观测，当今公认的宇宙模型中，宇宙是由大约 72% 的暗能量（dark energy），23% 的非重子暗物质（non-baryonic dark matter）以及大约 4.6% 的宇宙的普通物质（baryons）所组成。

早在 1933 年，Zwicky 在测量了银河系中 Coma 簇边缘物质的速度时发现该速度与理论预测值发生很大的偏差。为了解释个偏差，Zwicky 提出了暗物质的假说。从那之后，对于暗物质粒子的性质的研究成为现代物理学中的一个引人入胜的基本问题。物理学家们投入大量的精力在标准模型之外去寻找合适的暗物质候选者。在所有的候选者当中，大质量弱相互作用粒子（weakly interacting massive particles WIMPs）脱颖而出，成为一类很有希望的候选。大质量弱相互作用粒子可以通过标准模型之外的几种物理模型自然导出 [6–8]。比如说，在超对称模型中（supersymmetric (SUSY)），最轻的超对称粒子可以满足绝大多数大质量弱相互作用粒子的性质 [9, 10]。理论上讲，大质量弱相互作用粒子是一种电中性的，质量范围在吉电子伏特（GeV）到梯电子伏特（TeV）之间，并且与普通物质之间可以发生与中微子类似的弱相互作用的基本粒子。

大质量弱相互作用粒子可以通过其与探测器中原子发生弹性散射之后产生的原子反冲信号而被直接观测。

在过去的二十几年时间里，暗物质粒子的直接探测实验蓬勃发展 [11]。在这些直接探测实验中，液氙探测器成为最有希望的一种探测器。最近的 XENON100 液氙探测实验在几乎所有的可能的 WIMP 的质量范围内，给出了最好的探测极限。该实验结果的灵敏度远远高于使用其他的探测介质 [12]。同时，一系列的液氙探测实验也将加入到暗物质直接探测中来，包括 XMASS，LUX，PandaX，以及 XENON1T。绝大多数先进的液氙探测器 [13–15] 都是双模工作，来同时探测光信号（有时被称为直接光信号，通常用 S1 表示）和电子信号（有时也被称为放大光信号，通常用 S2 表示)。光信号和电子信号与相对发光效率（relative scintillation efficiency ($\mathcal{L}_{\rm eff}$)）以及电离信号效率（ionization yield ($\mathcal{Q}_{\rm y}$)）相结合，可以被用于重构校准核反冲信号的能量。因此，相对发光效率和电离信号效率在 WIMPs 直接探测实验中是两个重要的参量。

在这一章中，我们首先回顾一些宇宙观测中所发现的非相对论性，非重子性的暗物质粒子存在的证据，同时说明为什么大质量弱相互作用粒子是最具吸引力的暗物质粒子候选对象。之后，我们会介绍暗物质直接探测的方法，液氙探测器的基本实现以及其重要的参数。在第二章中，我们会分析核反冲在探测器中的减速过程，并且说明我们是如何来计算核反冲的电子能损。在第三章中，我们首先回顾计算液氙介质中核反冲的电子能损的理论模型以及实验观测的数据，继而我们对现有理论模型进行分析并针对动量传输截面模型做了优化，从而理论预测低能区的液氙核反冲的电子能损值。在第四章中，我们详细讨论了双模液氙探测器中的发光和电离过程，然后对电子离子对的重新结合效率进行了理论分析和计算。最后，我们在第五章中给出了我们对于 $\mathcal{L}_{\rm eff}$ 和 $\mathcal{Q}_{\rm y}$ 的理论计算结果，并且指出一些潜在问题，以及未来可以优化的地方。

1.1 暗物质粒子存在的证据和候选对象

1.1.1 宇宙中消失的质量和暗物质假说

根据牛顿的万有引力定律，我们可以很容计算出一组球对称的有质量的物体，通过万有引力，在距离质心为 r 的位置处的旋转速度。该速度可以通过下

面的方程来显示：

$$v(r) = \sqrt{\frac{GM(r)}{r}} \tag{1–1}$$

在方程中 $M(r) = 4\pi \int \rho(r) r^2 dr$，而 $\rho(r)$ 是质量密度。然而上述方程 Eq. (1–1) 却很难解释银河系的旋臂的旋转速度。通过对银河系旋臂的旋转速度的观测，科学家发现可观测物质的质量明显无法满足银河系旋臂的旋转速度。这意味着一定有大量的物质是无法通过电磁作用被观测到的。实际上，大量的宇宙学观测都显示出在宇宙中，尤其是银河系中，一定存在大量的物质，具有质量却无法被直接观测 [16]。

早在 1933 年，当 Zwicky 开始研究银河系簇团的旋转的观测速度与理论预言速度的偏差的时候 [17]，他就发现银河系的旋臂的旋转速度，在大半径的情况，与物质质量之间的关系更接近正比关系 $M(r) \propto r$。这就意味着，如果万有引力定律 Eq. (1–1) 是正确的，那么至少有 10 倍于可观测质量的物质存在于银河系而不能为普通的光学观测所测量到。Zwicky 的结果预言，在银河系的可观测银盘周围存在一个光学手段观测不到的暗物质晕，该暗物质晕的密度与半径的平方成反比例关系 $\rho(r) \propto 1/r^2$。在 Zwicky 之后，越来越多的关于银河系中物质旋转速度与半径之间的关系的宇宙学观测都显示，螺旋型和椭圆型银河系的质量几乎随着半径的增加，而线性增长，该规律至少在半径到达 100 kpc 和 1012 $M_\odot$ 仍然成立 [18, 19]。所有这些观测结果无不显示我们所观测到的物质，只是银河系中所有物质中很少的一部分。在 1979 年，Faber 和 Gallagher 在一篇综述文章中对宇宙学观测做了回顾，并且给出了他们关于不同类型的银河系的可观测与不可观测质量之间比率的研究结果 [20]。在这篇综述文章中，Faber 和 Gallagher 总结了在银河系中存在大量不可光学观测的具有质量的物质的大量的令人信服的证据。到今天，大量暗物质广泛存在于我们所处的银河系中这一观点已经被广为接受 [21]。暗物质假说很好的说明了为什么现在的宇宙学观测中物质的旋转速度与牛顿万有引力定律不相符合。

很自然，仅仅银河系旋臂的引力效应的观测远不能广泛引起大量物理学家对暗物质的兴趣。暗物质假说同时还是用于解释很多其他宇宙学效应的关键因素，比如说在宇宙的质量密度 Ω_m 上的宇宙学约束就是其中之一。Friedmann 曾经提出过下面这样一组方程来构造由非相对论性的物质以及宇宙常数来约束的宇宙：

$$\frac{H^2}{H_0^2} \equiv \frac{1}{H_0^2}\left(\frac{\dot{a}}{a}\right)^2 = \Omega_m \left(\frac{a_0}{a}\right)^3 + \Omega_k \left(\frac{a_0}{a}\right)^2 + \Omega_\Lambda \,, \tag{1–2}$$

$$\frac{1}{H_0^2}\frac{\ddot{a}}{a} = -\frac{1}{2}\Omega_m \left(\frac{a_0}{a}\right)^3 + \Omega_\Lambda \,, \tag{1–3}$$

在这组方程，Ω_m 和 Ω_Λ 是宇宙中物质能量密度以及关于临界密度 $\frac{3H_0^2}{8\pi G}$ 的宇宙学常数。H_0 是今天的哈勃常数（70.8 km/s/Mpc），H 和 a 是在时间点为 t 的时候的哈勃常数和刻度系数。而 Ω_k 则是一项用于描述宇宙的空间曲率的参数。其中相对密度需要满足关系：$\Omega_m + \Omega_k + \Omega_\Lambda = 1$。通过这关系以及今天的方程 Eq. (1–2)，我们可以估量其中的各个参数。随着技术的进步，各种大型天文望远镜以及相关设备的发展，Friedmann 方程可以通过今天的宇宙学观测结果精确的检验。同时，宇宙的加速膨胀以及宇宙微波背景辐射（CMB）的各向异性的性质能以前所未有的精度来度量。根据最近的对于 Ia 型超新星，银河系，以及宇宙微波背景辐射的观测，宇宙学常数 Ω_Λ 被确定为 ~0.7，而宇宙的质量密度 Ω_m 大约在 0.3 左右。图1–1（图片来自于 http://supernova.lbl.gov/Union/）所显示的即为宇宙学观测的结果。而宇宙中普通物质的密度从通过大爆炸核合成和宇宙背景辐射来观察，结果为 5% 左右。因此一定有大约 23% 左右的物质非普通物质。

另外通过弱引力透镜观测，科学家也可以更好的测量确定物质密度，从而进一步验证暗物质的存在性。通过一个弱引力透镜，从遥远的星系传播而来的光，因为在引力场的作用下会被扭曲。通过对观测到的光路扭曲，以及光路上的可观测到的物质的质量，科学家可以估算在光路上有多少具有质量的物质没有被观测到。通常情况下，强引力透镜会使光线发生严重偏转，从而形成远方星系的重影。而弱引力透镜与之不同，光线的扭曲只是微弱的。通过对大量的弱引力透镜成像的研究，科学家可以精确推导出相关弱引力透镜的质量。在综述文章 [22] 中，我们可以了解到弱引力透镜的相关性质。Clowe 等科学家曾经在 [23] 一文中，展示了一个弱引力透镜的实例：1E 0657-558Ref. [23]，该实例可以作为一个暗物质存在的直接证据。

宇宙大尺度结构也可以作为暗物质存在的另一个证据。宇宙结构形成于质量稠密区域，它可以用于研究早期的宇宙物质密度的涨落，同时可以作为暗物质性质研究的一个线索。引力的不稳定性以及早期宇宙密度场的微小涨落会最终导致今天得大尺度结构上的宇宙结构以及星系在今天的宇宙中的分布。因此，对于星系团在大尺度结构上的分布的研究，可以用于来确定早期宇宙的质量密度。一些大型的实验，比如说斯隆数字巡天（Sloan Digital Sky Survey），已经揭示了宇宙的大尺度结构，甚至超大尺度结构。从所观测到的大尺度结构

的演化，物理学家可以重构早期的宇宙质量密度。结果显示，暗物质粒子，特别是非相对论性的暗物质粒子 [24]，是早期宇宙必不可少的组成部分。

1.1.2　暗物质和大质量弱相互作用粒子

正如上一节中所言，宇宙学观测中的大量证据告诉我们宇宙的组成成分如下：大约 4.6% 的组成普通物质的重子，23% 左右的具有质量却无法通过光学手段观测的暗物质粒子，以及大约 72% 的真空能，通常也被称作暗能量。显而易见的是，暗物质一定广泛存在于我们所处的宇宙当中。然而因为至今我们还没有直接观测到暗物质，因此暗物质粒子的自然属性对于我们来说仍然是一个迷。因为现有的粒子物理的标准模型所预言的粒子已经通过各种手段被发现，因此如果我们通过直接的实验观测发现宇宙中这些无法通过光学手段观测的暗物质粒子，我们距离新的物理现象就不会太远，也许我们可以通过对暗物质粒子的研究而突破当今的物理前沿。在所有的暗物质粒子的理论预测模型当中，有两类粒子比较令人振奋：一是轴粒子，即一种假设的亚原子粒子（axions），另外一种就是大质量弱相互作用粒子。在本文当中，我们将更多的精力放在大质量弱相互作用粒子上面。读者如果对于轴粒子感兴趣，可以阅读综述文章 [25]。

如果我们假定，暗物质粒子是宇宙大爆炸的遗迹，那么大质量弱相互作用粒子假说将会基于现有理论而自然涌现。假设存在一种粒子 χ，该粒子具有质量 M_χ，其湮灭的散射截面为 σ_a。在早期的宇宙当中，当温度能标远大于该粒子的质量的时候，即 $T \gg M_\chi$，这些粒子将与其他较轻的粒子相类似，具有相同的丰度，并处于热平衡状态。当年轻的宇宙逐渐冷却到温度能标低于该粒子质量的时候，即 $T < M_\chi$，该粒子热平衡数量 n_χ^{eq} 将会下降。该类粒子的数密度应该满足下列方程：

$$\frac{dn_\chi}{dt} = -\langle\sigma_a v\rangle[(n_\chi)^2 - (n_\chi^{eq})^2] - 3Hn_\chi\,, \tag{1–4}$$

在该方程中，$\langle\sigma_a v\rangle$ 是热平均温度与粒子湮灭截面的乘积。方程 Eq. (1–4) 的右边的第一项显示 n_χ 以某一速率接近 n_χ^{eq}，而该速率由湮灭截面与粒子的通量的乘积所决定。而方程右边的第二项则显示因为空间膨胀而引起的 n_χ 的下降。因为早期的宇宙是由辐射所决定的，所以方程中膨胀系数 H 是独立确定的。在粒子湮灭刚刚开始的时候，方程由右边第一项所确定。但是当宇宙逐渐膨胀，

粒子的数密度开始下降，方程右边的第二项开始变得越来越重要。当粒子湮灭停止的时候，剩下的粒子逐渐冷却，并保持一个相对恒定的密度。根据热动力学以及膨胀动力学的物理理论 [26]，我们可以计算出该粒子在冷却之后，其质量密度与 M_χ 想独立，同时反比于 $\langle\sigma_a v\rangle$。我们假设该粒子是稳定的，那么该粒子的遗迹密度将依旧存在于今天的宇宙当中。我们假定该粒子的湮灭截面与粒子物理中的弱相互作用相类似，那么我们可以得到下面的方程 [26]:

$$\langle\sigma_a v\rangle = \alpha^2(100\text{GeV})^{-2} \sim 10^{-25}\text{cm}^3\text{s}^{-1} \tag{1–5}$$

我们可以得到该粒子的遗留密度约等于 0.1，即 $\Omega_\chi \sim 0.1$。该密度的数量级恰好与我们所观测到的暗物质粒子相符合。换句话说，如果大质量弱相互作用粒子是稳定存在的，它将是一类密度正好是，或至少接近，我们现在进行的宇宙学观测的暗物质粒子。

从另外一方来说，在粒子物理当中，为了统一自然界中存在的四种众所周知的基本作用，科学家曾提出超对称理论假说。超对称理论指出，标准模型中的任何一个基本粒子都有一个超对称粒子。而大质量弱相互作用粒子正好与超对称理论所预言的最轻的超对称粒子（LSP）相类似。两种粒子都是稳定的，电中性的。因此，大质量弱相互作用粒子也可以说是超对称理论的一个自然结果。如果能够直接探测到大质量弱相互作用粒子，科学家也可以对超对称理论假说进行证伪或者证明。

1.2 大质量弱相互作用粒子的直接探测方法和液氙探测器技术

1.2.1 大质量弱相互作用粒子的直接探测方法

通过第1.1节中提及的各种宇宙学观测，我们几乎可以确信暗物质的确存在于我们身边的宇宙中，同时我们也有足够理由相信大质量弱相互作用粒子应该是一个很有吸引力的暗物质粒子的候选。然而由于缺乏直接的观测，暗物质粒子的各种自然属性我们还一无所知。为了能够进一步研究暗物质粒子，实验物理学家们正致力于去直接探测暗物质粒子，其中多数直接探测实验被设计用来探测大质量弱相互作用粒子。根据粒子物理的理论，我们知道，弱相互作用的力程非常短，因此大质量弱相互作用粒子与普通物质的作用截面也相应特别小。所以大多数的暗物质粒子直接探测实验都致力于观测大质量弱相互作用粒

子被探测器中的原子，特别是原子核，所散射之后产生的原子反冲或者原子核反冲信号。

早在 1985 年，Goodman 和 Witten 就曾在 [27] 一文中详细探讨了大质量弱相互作用粒子的直接探测的可能性。我们可以假定地球和银河系中的暗物质晕都在银河系中运动。当地球上的暗物质探测器被暗物质晕中的某个大质量弱相互作用粒子所击中，那么被击中的原子将会从大质量弱相互作用粒子那里获得高达几十千电子伏特（keV）的动能 [28]。由于大质量弱相互作用粒子与普通物质的作用截面极小，当它被暗物质探测器中某个原子核所散射之后，几乎不会继续跟其他原子核发生作用而逃离探测器，但是被击中目标原子核却变成了一个反冲原子核，继续与探测器中其他的原子发生作用。如果这个核反冲的所引起的信号可以被探测到，我们就可以认为这种信号算是大质量弱相互作用粒子被直接探测到的信号。当然了，大质量弱相互作用粒子也可能被探测器中的原子的核外电子所散射，但是，我们认为这时候所产生的信号非常微弱，很难被探测到。因此我们在本文中会忽略这种效应。

对于大质量弱相互作用粒子直接探测实验来说，最大的一个挑战是如何区分那些被大质量弱相互作用粒子所引起的核反冲信号和宇宙射线以及探测器实验材料的自身放射性，比如说 γ 射线，所引起的其他信号区分开。举例来说，来自于放射性的 γ 射线，或者来自于中子辐射源的中子，会在探测器中产生相应的电子反冲信号和核反冲信号，其中中子引起的核反冲信号与大质量弱相互作用粒子所引起的核反冲信号极其相似。在实践中，实验物理学家通常用下面两种方法来区分这些信号：

- 由于大质量弱相互作用粒子与普通物质的作用截面极小，当它被暗物质探测器中某个原子核所散射之后，几乎不会继续跟其他原子核发生作用而逃离探测器，而其他穿透探测器的粒子或射线，比如说中子射线或者 γ 射线，都会与探测器中的原子发生多次散射。另外，暗物质探测也通常被置于一些地下实验室，从而能够利用地壳的厚度来屏蔽部分的宇宙线的干扰；

- 由于多数的放射性将会在探测器中引起电子反冲，并将部分能量传递给探测器中电子。与之不同，大质量弱相互作用粒子基本只会引起核反冲。因此，如果实验上能够区分核反冲信号和电子反冲信号，那么大质量弱相互作用粒子的信号就可以被挑选出来。

1.2.2 基本液氙探测器

大质量弱相互作用暗物质粒子的基本自然属性决定了暗物质直接探测实验需要探测器具有极高的灵敏度，同时可以区分核反冲信号与电子反冲信号。根据这些理论需求，液氙暗物质探测器成为一种最有可能发现大质量弱相互作用粒子的探测器。在过去二十年里，大量的暗物质探测器都选用液氙作为探测介质 [11]。在这一节中，我们讲首先回顾使用液氙作为暗物质探测器探测介质的优点，然后我们会具体描述基本的双模液氙探测器（LXe TPC）的属性。

由于大质量弱相互作用粒子与普通物质的作用截面极小，暗物质探测器的灵敏度为探测器的体积和质量所制约。暗物质探测器质量越大，体积越大，捕获到暗物质粒子的可能性就越高。与其他类似于碘化钠（NaI）或者锗半导体（Ge）晶体发光体探测器相比较，液氙探测器更容易被做成更大体积，更大质量。这比起制造更大的晶体发光体探测器更加经济，并且技术上容易实现 [29]。正如我们上文所说，暗物质探测器应该有能力来区分电子反冲信号和核反冲信号，而双模液氙探测器可以很容易做到这点。首先，由于氙是一种惰性气体原子，其化学性质十分稳定，液氙很容易被提纯，同时具有很强的自屏蔽外来辐射的能力。而且，氙没有长半衰期的同位素，因此液氙本身的背景辐射可以被控制得非常低。其次，液氙是一种性质非常优良的发光体，同时如果在液氙探测器上加上漂移电场，液氙中可以有足够多的电离信号被捕获到。因为在惰性气体元素中，核反冲与电子反冲所产生的电离密度是不同的，实验物理学家可以通过同时观测液氙探测器的光信号和电离信号来讲背景辐射的信号从有用的信号中区分出来。通常来说，我们把这种液氙探测叫做双模液氙探测器，当今最优良的高级液氙探测器都是工作在双模模式下。在这种双模液氙探测器中，光信号通常通过液氙探测中光电倍增管（photo-multiplier tubes (PMTs)）来探测。当光信号产生之后，置于液氙探测器中的光电倍增管可以直接检测到相应的光子，包括光子数量，强度等信息。而电离信号的捕获稍微复杂一点。通常是在液氙探测器外加上一个漂移电场，这样当液氙原子被电离后，所产生的自由电子在外加电场的作用下，漂移到一个充满氙气的空腔中，在该空腔中，电子会与其中的氙气原子发生总用产生光子，该光子同样被光电倍增管捕获，而产生信号。因此，虽然电离信号是由于电子产生，但是最终捕获的却是光子。因为这种探测器同时使用液态的氙和气态的氙作为探测介质，所以我们称之为双模探测器。但是为了说明方便，我们在本文中通常称其

为双模液氙探测器。

通常情况下，光电倍增管被用来探测度量 S1 信号。在液氙探测器中，大量的光电倍增管被置于探测器探测介质的上方和下方，用以探测液氙介质被激发所产生的光信号。对于电离信号，由于液氙介质因电离所产生的自由电子数量较少，很难通过电荷测量设备所捕获到，因此在双模液氙探测器中，液氙电离出来的自由电子通常通过外加电场 E_d 的引导漂移到一个充满氙气的云室，自由电子在云室中发光。当自由电子到达云室之后，自由电子通过电场加速，与云室中其他原子发生作用，从而信号被放大 [30]，从而产生放大的光信号 S2。放大的光信号也是 175 纳米（nm）的光子，用同样的光电倍增管来进行探测。对于由大质量弱相互作用粒子或者中子引起的核反冲，以及由伽马射线等宇宙背景辐射所引起的电子反冲来说，S2 信号和 S1 信号之间比率，S2/S1，是不相同的。正是 S2/S1 的不同，实验物理学家可以很高精度的区分核反冲信号和电子反冲信号。现在的技术可以保证从所有信号中以 99.5% 剔除电子反冲信号，并且以 50% 保证核反冲信号不被摒弃。同时由于 S1 信号和 S2 信号产生的时间不同，我们也称这种探测器为时间投影室（“time projection chamber” (TPC)）。

在当今的实验中，采用这种双模工作模式的液氙探测器包括日本的 XMASS 实验 [31]，英国的 ZEPIN 实验 [32]，美国的 XENON 实验 [33]，以及中国四川的 PandaX 实验 [34]。

1.2.3　双模液氙探测器的发光效率和电离效率

正如我们上文所说，多数的液氙暗物质直接探测器都工作在双模模式，可以同时测量 S1 信号和 S2 信号。而 S1 信号和 S2 信号与相对发光效率（$\mathcal{L}_{\text{eff}}$）以及电离效率（$\mathcal{Q}_{\text{y}}$）相结合，可以用来重新构建或者校准核反冲信号的初始能量。因此，$\mathcal{L}_{\text{eff}}$ 和 $\mathcal{Q}_{\text{y}}$ 作为连接 S1，S2 信号与核反冲初始能量的关键参数，在暗物质探测实验中起着举足轻重的作用。

所谓的发光效率所指的是液氙暗物质探测器所探测到的光信号 S1 与大质量弱相互作用粒子粒子在暗物质探测器中所沉淀的能量，即核反冲能量之间的比值。当大质量弱相互作用粒子与液氙探测器中的某个原子核发生弹性散射，该原子核成为一个具有几十千电子伏特（keV）动能的反冲原子。该反冲电子在液氙探测器中的减速过程中，会最终耗尽其所获得动能，从而使探测器中的

电子激发或者电离，同时使探测器中介质的温度发生微小变化，即热效应。由于液氙探测器通常质量和体积都是极大的，一个反冲原子核所引起的液氙温度的变化几乎可以忽略不计，因此该反冲原子核所产生的光信号和电离信号是实验中重点探测的信号。液氙探测器的发光效率通常定义为核反冲能量中，最终导致光信号的能量与初始核反冲能量的比率。在实验上，通常使用与具体探测器无关的相对发光效率（*Relative Scintillation Efficiency* $\mathcal{L}_{\rm eff}$）来度量液氙探测器的发光效率。液氙探测器的相对发光效率被定义为 [12]：

$$\mathcal{L}_{\rm eff}(E_{\rm nr}) = \frac{S_{\rm ee}}{S_{\rm nr}} \frac{S1(E_{\rm nr})}{E_{\rm nr}} \frac{1}{L_y} \,, \tag{1–6}$$

其中 $S1(E_{\rm nr})$ 是从具有初始能量为 $E_{\rm nr}$ 的核反冲事件中所产生的光信号数量，而 L_y 是从初始能量为 122 千电子伏特（keV）的电子反冲事件（该事件通常产生于 ^{57}Co 放射源所产生的单能 γ 射线）中所产生的光信号数量与 122 千电子伏特的比值。其中的系数 $S_{\rm ee}/S_{\rm nr}$ 与具体的探测器有关，用来修正在特定外加电场条件下的光信号数量。因此，我们可以认为液氙暗物质探测器的相对发光效率（$\mathcal{L}_{\rm eff}$）是一个在零外加电场条件的发光效率，即与电场无关。从相对发光效率的定义我们可以看出，$\mathcal{L}_{\rm eff}$ 的数值实际上是核反冲事件的发光效率和电子反冲事件的发光效率的比值。通常来说，这个比值应该与具体的探测器无光。

同样的，液氙暗物质探测器的电离效率也可以连接可探测的电离信号 S2 与大质量弱相互作用粒子粒子在暗物质探测器中所沉淀的能量。液氙探测器的电离效率（*Ionization Yield* $\mathcal{Q}_{\rm y}$）指的是实验所能观测到的自由电子数量与核反冲能量的比值（e^-/keV），可以用下面的方程来表示：

$$\mathcal{Q}_{\rm y}(E_{\rm nr}) = \frac{Q(E_{\rm nr})}{E_{\rm nr}} \,, \tag{1–7}$$

方程中，$Q(E_{\rm nr})$ 是从初始能量为 $E_{\rm nr}$ 的核反冲事件中所产生的自由电子，最终漂移到云室中的电子的数量。与发光效率类似，液氙探测器的电离效率也被认为与具体的探测器实现无关。

为了了解 S1 信号或者 S2 信号与核反冲初始能量之间的关系，在过去几年里，实验物理学家们利用单能中子源，开展了一系列的实验 [15, 35, 36] 来实验探测液氙探测器的发光效率（$\mathcal{L}_{\rm eff}$）和电离效率（$\mathcal{Q}_{\rm y}$）。然而从这些实验都要求精确测量中子流在液氙探测器中的散射，如果要产生低能核反冲事件，必须要求中子流的散射角极小，从而引起测量精度上问题。可以说，通过实验来测量

发光效率（$\mathcal{L}_{\text{eff}}$）和电离效率（$\mathcal{Q}_{\text{y}}$）对于低能核反冲是非常困难的。而且通过不同的实验我们也可以看出，产生的核反冲能量越低，实验结果中的系统误差也就越大，在不同实验在低能核反冲去的测量结果甚至产生了冲突。从现在的实验结果来看，实验测量到的最低的发光效率大约在 3 千电子伏特（keV）附近 [36]。低于 3 千电子伏特（keV），只能通过人工外推的方式来实现 [12]，这就造成了发光效率在低能核反冲区域的不精确性。对于实验探测的电离效率（$\mathcal{Q}_{\text{y}}$）来讲，实验数据更少一些。到现在，实验测量的最低核反冲能量区域大约在 4 千电子伏特（keV）左右。对于更低能的区域，物理学家们只能通过一些计算机程序进行模拟计算。

而根据推测，轻暗物质粒子（WIMPs）会具有大约 10 吉电子伏特（GeV）的质量。而该质量的暗物质粒子在液氙探测器中所产生的核反冲信号的初始能量应该在 2 千电子伏特（keV）左右，甚至更低 [37–39]。恰恰这个能量区域，液氙暗物质探测器的发光效率（$\mathcal{L}_{\text{eff}}$）和电离效率（$\mathcal{Q}_{\text{y}}$）却无法通过实验来精确测量。而实验外推通常认为在低能区域，液氙探测器的发光效率是一个恒定值。通过外推实验观测结果得出的发光效率或者电离效率充满争议。比如说 Collar 和 McKinsey 曾经指出液氙探测器的发光在低能区域应该是稳步下降的，因为当核反冲初始能量低于某个定值的时候，核反冲将无法引起液氙的激发电离 [40]。同时，Collar 和 McKinsey 引用通过广谱中子源测定的液氙探测器的发光效率，指出当核反冲事件的初始能量在低于 20 千电子伏特（keV）之后，液氙探测器的发光效率会变低 [41, 42]。当然该实验也是有争议，在最新的 XENON100 [43] 实验的测量结果就与上述实验结果不一致。

显然，仅仅依靠实验测量，我们很难得到精确而准确的液氙探测器的发光效率 $\mathcal{L}_{\text{eff}}$ 和电离效率 $\mathcal{Q}_{\text{y}}$。在接下来的章节中，我们就会具体研究反冲原子核在液氙探测器中的减速过程，以及液氙的发光和电离过程。然后我们进一步分析如何计算核反冲事件所产生的发光和电离数量。最后我们可以给出液氙探测器的发光效率 $\mathcal{L}_{\text{eff}}$ 和电离效率 $\mathcal{Q}_{\text{y}}$ 的理论值。

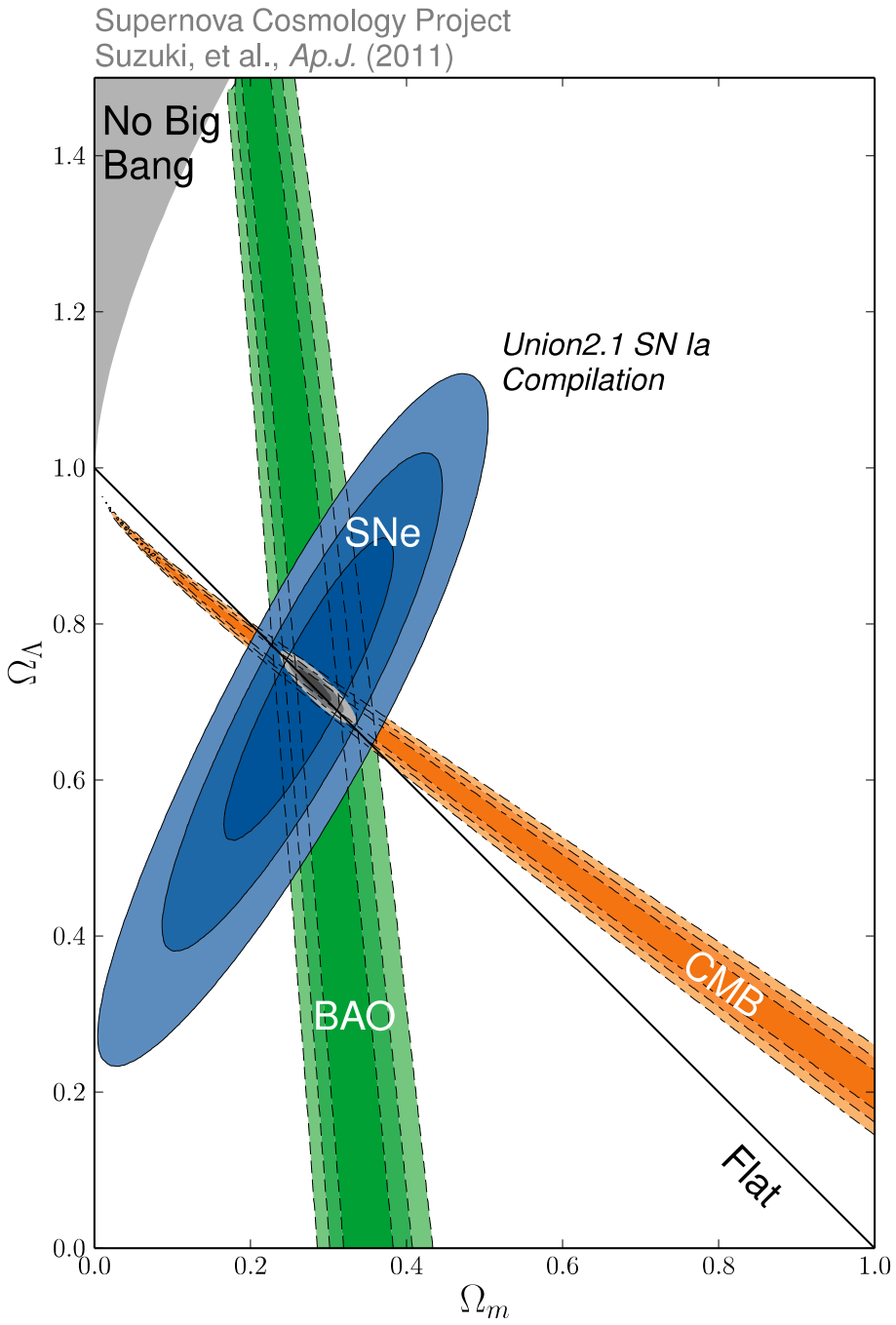

图 1–1 宇宙学上对 Ω_m 的约束

第二章　反冲核在液氙探测器中的能量损失过程

理论上讲，要计算液氙探测器的发光效率 $\mathcal{L}_{\rm eff}$ 和电离效率 $\mathcal{Q}_{\rm y}$，通常的做法是先计算出所谓的 Lindhard 系数，（又叫做 nuclear quenching factor $q_{\rm nc}(E_{\rm nr}) = \eta(E_{\rm nr})/E_{\rm nr}$） [44]。通过 Lindhard 系数来计算有多少初始的核反冲能量在反冲核的减速过程中传递给了介质当中的电子 $\eta(E_{\rm nr})$。然后根据能量 $\eta(E_{\rm nr})$ 来估算会产生多少激发原子和电离的电子，最后再计算发光效率 $\mathcal{L}_{\rm eff}$ 和电离效率 $\mathcal{Q}_{\rm y}$ [45–47]。另外也可以通过一些计算机模拟程序，比如说 TRIM [48] 或者 EANT4 [49]，来计算能量 $\eta(E_{\rm nr})$，然后计算发光效率 $\mathcal{L}_{\rm eff}$ 和电离效率 $\mathcal{Q}_{\rm y}$。而现在问题是，不管是被广泛引用的 Lindhard 系数还是计算机模拟程序都没有在核反冲低能区域校准过。这就会相应引起人们对由此而来的发光效率 $\mathcal{L}_{\rm eff}$ 和电离效率 $\mathcal{Q}_{\rm y}$ 的疑问。虽然说 Lindhard 的基本积分方程 [44] 可以很完美的描述反冲核在介质中的减速过程，同时给出了一个理论计算或者计算机模拟的算法，然而这中间存在着大量的不清楚的物理图像，或者待定自由常数。比如说在不同的文献中所引用的 Lindhar 系数 $q_{\rm nc}$ 就不尽相同，具体可以参阅文献 [45–47]。同时，在计算机模拟软件中，一些诸如位移能之类的参数都是人为设定的，缺乏实践性。因此为了得到更加精确而正确的发光效率 $\mathcal{L}_{\rm eff}$ 和电离效率 $\mathcal{Q}_{\rm y}$，我们决定自己来研究反冲核的减速过程，从而计算出更符合实际的 Lindhard 系数 $q_{\rm nc}$。

在这一章中，我们首先会分析反冲核在液氙介质中的减速过程。之后，我们花一定篇幅介绍 Lindhard 的基本积分方程，因为这个积分方程给出了反冲核在介质中的减速过程的清晰的物理图像，同时也为计算机模拟算法提供线索。最后我们会说明我们是如何通过计算机模拟程序来计算 Lindhard 系数 $q_{\rm nc}$。

2.1　反冲核在介质中的减速过程

2.1.1　不同粒子在液氙介质中的减速过程

众所周知，不同的粒子，比如说 γ 射线，α 粒子，中子，以及重离子等等，在液氙介质中的反应为完全不同的物理图像所反映。读者如果有兴趣可以参考 Knoll 相关领域的经典著作 [50]。本文在介绍反冲核的减速过程之前，对各种

不同的粒子在液氩探测器中的反应过程稍作涉猎，以便于读者可以更好的识别不同的物理过程。

作为带两个正电荷的氦原子核，α 粒子流穿过一个介质的时候，会通过库伦相互作用与介质中原子的核外电子云发生作用。其中结果之一就是，如果电子云中的某个电子从与 α 粒子的相互作用中获得了足够的能量，这个电子就会被激发到更高的原子能级，甚至直接从该原子的电子云中被剥离出来，从而成为自由电子。一束高能的 α 粒子流在介质中穿行的时候，在其运行的轨道上会不断的重复上述的过程。于是原来的 α 粒子所携带的动能最终转化成为介质中电子的激发或者电离能量。最终，α 粒子的逐渐减速至热运动的速度。与氦原子核相比，单个电子的质量如此之微小，以至于当 α 粒子在电子云中穿行的时候，电子根本无法改变其运动方向。而电子对 α 粒子所施加的库伦力，仅仅相当于沿着 α 粒子运动轨迹的一个微小的摩擦力。最终结果就是 α 粒子在介质中的运行轨迹几乎是一条直线。

对于电子流，我们需要用另外一个物理图像来描述。与 α 粒子流不同，电子流的轨迹通常显得扭曲无比。这是因为当电子穿过介质时，电子与介质中的原子的核外电子同样发生库伦作用，但是由于不同电子质量相同，电子云中的电子完全有能力完全改变电子流中的电子的运动轨迹。也因为如此，电子流在介质穿行过程中，能损较慢。与 α 粒子流相比，电子流的轨迹要长得多。

而 γ 射线的减速过程就更加复杂了。通常来说，γ 射线与介质之间的反应有三种不同的类型：光电子吸收（即光电效应），康普顿散射（Compton scattering），正负电子对产生。其中光电子吸收现象多数发生于低能 γ 射线。当 γ 射线的能量完全被一个原子吸收，某个原子的核外电子获得能量从束缚态中脱离出来，变成自由电子。这时候，通过探测器可以探测到自由电子。我们之前说的 122 千电子伏特（keV）的从 ^{57}Co 放射性同位素所发出的 γ 射线即主要发生此种反应。康普顿散射通常在入射的 γ 射线能量比较高的情况下发生。当入射 γ 射线的能量比较高，一方面入射 γ 射线传递部分能量给电子云中的电子，一方面被反射。在这种反应中，通过探测器也可以探测到自由电子。能量在大约 1 兆电子伏特（MeV）的 γ 射线通常会发生这种反应，比如说说 622 千电子伏特（keV）的从 ^{137}Cs 放射性同位素所发出的 γ 射线。正负电子对产生过程通常发生在高能 γ 射线入射的情况。当入射 γ 射线的能量超过两倍的电子静止质量（1.02 MeV）的时候，入射 γ 射线会在介质中生成正负电子对。此时

如果使用探测器进行探测，会发现正电子。这种效应只在 γ 射线的能量较大时(大约数个兆电子伏特）发生。

根据能量的不同，中子流在介质中表现出不同的性质。对于快中子流，核反冲事件会被激发，这与大质量弱相互作用粒子（WIMP）所产生的核反冲事件类似。因此，实验上经常用快中子流来产生核反冲时间，从而测量液氙探测器的发光效率 $\mathcal{L}_{\text{eff}}$ 和电离效率 $\mathcal{Q}_{\text{y}}$。如果中子流的能量更高一些，那么中子的非弹性散射有可能发生。这时候就会发生核聚变或者核裂变反应。原子弹，中子弹等核武器的原理尽在于此。这时候，中子流的能量在核受到激发，退激发之后最终转化为高能 γ 射线。而慢中子流，通常发生的反应是与介质中的原子核的弹性散射。当我们提及慢中子的时候，大多只是的是热中子，即在室温环境下，能量在 0.025 电子伏特（eV）的中子。

当我们谈及重核粒子，或者反冲核的时候，问题变得更加复杂。我们在此直接回归主题，来看一下在液氙暗物质探测器中的反冲核的减速情况。当一个氙原子核被一个大质量弱相互作用粒子击中之后，这个原子核会获得大约几十千电子伏特（keV）的动能，从而变成一个反冲核。当这个反冲核在液氙介质中穿行的时候，它会与介质中其他的原子核发生弹性散射。我们可以用经典物理里面的二体碰撞模型来描述这一过程。而我们知道，二体碰撞发生时，入射粒子的轨道通常会发生改变。在与其他原子核发生弹性碰撞的同时，反冲核还会与介质中原子云中的电子发生非弹性碰撞，从而传递动能给介质中的电子。该反应的直接结果就是，介质中的电子可能会被激发或者电离。与此同时，更复杂的是，由于反冲核与介质中其他原子核的弹性碰撞，其他原子核也会获得部分动能而成为能量较低的反冲核，我们把这一个过程叫做碰撞级联。这些反冲核也会在液氙介质中穿行，重复初始反冲核在液氙介质中的减速过程。因此，对于核反冲来说，一个核反冲会引起一系列的次级核反冲，每个核反冲都有可能激发或者电离介质中的电子。最终，当所有的核反冲，包括初始核反冲和次级核反冲，在液氙介质中逐渐减速至热运动的速度的时候，整个过程可以认为停止下来。而此时，一个核反冲事件会引起电子电离，电子激发，原子核热运动。原则上将，整个过程是一个包含多体效应的非常复杂的过程，需要用基本量子散射理论进行求解。

2.1.2 Lindhard 基本积分方程

为了计算重离子或者反冲核在介质减速过程中的损失给电子的能量，Lindhard 等科学家曾经根据能量守恒定律提出一个基本积分方程。该方程可以较好的描述在碰撞级联过程中的能量传递过程 [44]。对于核反冲，这个基本积分方程可以通过下面的一些假定和简化来导出：

- 初始的反冲核具有的动能为 E_{nr}；
- 碰撞级联过程开始的时候，反冲核传递给介质中电子的能量 η 为零；
- 碰撞级联反应结束之后，反冲核传递给介质中电子的平均能量为 $\eta(E_{\mathrm{nr}})$；
- 数值 $\eta(E_{\mathrm{nr}})$ 是可加的，即 $\eta(E_{\mathrm{nr}})$ 可由碰撞级联过程中的所有单独的核反冲减速过程的损失给电子的能量 η 相加而得来；
- 一些效应，比如说介质的物理状态，产生的自由电子和负离子重新结合等等，可以忽略；

于是，对于初始能量为 E_{nr} 的反冲核，其传递给介质中电子的平均能量 $\eta(E_{\mathrm{nr}})$ 可以通过下面的递归过程表述：

- 假设反冲核在介质中穿行一段距离 dR，而介质中的原子的数密度的平均值为 N；
- 假设在一次碰撞中传递能量为 T_n 的碰撞可能性为 $NdRd\sigma_{n,e}$，而该碰撞过程中一部分能量 T_{ei} 被传递给了介质中的电子；
- 假设通过一次碰撞，反冲核的动能由 E_{nr} 降低到 $E_{\mathrm{nr}} - T_n - \sum T_{ei}$，即反冲核现在可以传递给介质中电子的总的平均能量从 $\eta(E_{\mathrm{nr}})$ 减少为 $\eta(E_{\mathrm{nr}} - T_n - \sum T_{ei})$；
- 假设通过一次碰撞，产生了二级反冲核，该二级反冲核具有动能 T_n。于是该二级反冲核可以传递给介质中电子的总的平均能量为 $\eta(T_n - U)$，其中 U 是二级反冲核脱离平衡位置所需要损失的能量；

最后，核反冲损失给电子的能量可以用另外一个量来表示 $\eta_e(E_{\rm nr})$，并且该能量最终在 $\eta(E_{\rm nr})$ 量的贡献为 $\sum \eta_e(T_{ei}-U_i)$。在表达式中，U_i 是相应的电子电离能。上述的碰撞可能性与总的反冲核可以传递给介质中电子的总的平均能量 $\eta(E_{\rm nr})$ 的乘积可以给出最终的 $\eta(E_{\rm nr})$ 值。于是我们可以对所有的碰撞进行积分。在此我们需要注意，当反冲核在介质中穿行 dR 距离的时候，该反冲核有一定概率不与其它原子核发生碰撞。该概率可以用 $1-NdR\int d\sigma_{n,e}$ 来表示。如果此类事件发生，那么反冲核可以传递给介质中电子的总的平均能量 $\eta(E_{\rm nr})$ 仍然是 $\eta(E_{\rm nr})$。

综合上述的过程，我们可以可到一个针对于初始反冲核的可以传递给介质中电子的总的平均能量 $\eta(E_{\rm nr})$ 的积分方程。该方程可以表述如下：

$$\begin{aligned}\eta(E_{\rm nr}) = \quad & NdR\int d\sigma_{n,e}\{\eta(E_{\rm nr}-T_n-\sum T_{ei})+\eta(T_n-U)+\sum\eta_e(T_{ei}-U_i)\} \\ & +(1-NdR\int d\sigma_{n,e})\eta(E_{\rm nr})\,, \end{aligned} \tag{2–1}$$

通过对这个方程进行化简，我们可以得到 Lindhard 的基本积分方程：

$$\int d\sigma_{n,e}\{\eta(E_{\rm nr}-T_n-\sum T_{ei})-\eta(E_{\rm nr})+\eta(T_n-U)+\sum\eta_e(T_{ei}-U_i)\}=0\,. \tag{2–2}$$

根据 Lindhard 基本积分方程 Eq. (2–2)，物理学家们推导出下面 Lindhard 系数的表述方程，来近似表达反冲核在减速过程中，传递给电子的能量与反冲核初始动能之间的比例关系 $q_{\rm nc}(E_{\rm nr})=\eta(E_{\rm nr})/E_{\rm nr}$，该系数也可以叫做 nuclear quenching factor：

$$q_{\rm nc}(E_{\rm nr})=\frac{\eta(E_{\rm nr})}{E_{\rm nr}}=\frac{kg(\epsilon)}{1+kg(\epsilon)}\,, \tag{2–3}$$

在上述表达式中，$\eta(E_{\rm nr})$ 是当反冲核初始能量为 $E_{\rm nr}$ 是，反冲核在减速过程中传递给介质中电子的总的能量。$g(\epsilon)$ 是一个经验公式，有兴趣的读者可以在 Lewin 等人的文献 [28] 中找到具体的形式。另外表达式中的 k 是一个不确定的量，它用来表示反冲核在单位距离上传递给电子能量 $(dE/dx)_{\rm el}$ 与反冲核速度之间的比例系数。对于氙，Lindhard 的计算结果是 $k=0.166$ [44]。而考虑到核反冲在液氙中的特殊的运行轨迹，Hitachi 对该值进行了重新计算，该值比 Lindhard 的结果要小，大约是 $k=0.110$ [45]。然而，根据实验数据来看，他们两个的结果都过高估计了反冲核可以传递给介质中电子的总的平均能量 $\eta(E_{\rm nr})$。根据分析，我们认为这是因为他们忽略了单位距离上传递给电子能量

$(dE/dx)_{\mathrm{el}}$ 在低能区域快速下降的现象。该现象曾被 Fukuda 等人在 1981 年通过实验验证 [51]。

从另外一个方面来说，一些计算机模拟程序，比如说 TRIM [48]（TRansport of Ions in Matter），也可以被用于计算反冲核可以传递给介质中电子的总的平均能量 $\eta(E_{\mathrm{nr}})$。但是这些程序通常对于高能重离子比较适用。对于低能区域的重离子在介质中的减速过程，有许多重要的参数是无法事先确定的，只能通过人工设定。而这些参数对低能核反冲最终的结果影响重大。同时，类似的计算机模拟程序通常认为介质中的原子是均匀分布的。因此，这些计算机模拟程序在低能区并没有被校准过。到现在为止，在低能核反冲区域（核反冲初始能量大约在千电子伏特左右），还没有理论上特别可行，特别精确的方法来计算 Lindhard 系数 q_{nc}。

2.2　核反冲减速过程的计算机模拟

为了得到液氙暗物质探测器中更加精确的 Lindhard 系数 q_{nc}，我们必须针对液氙探测器考虑更多的细节。比如说，我们需要考虑液氙探测器中的原子的微观分布，我们应该使用一些争议较少的参数等等。在这一节中，我们讲介绍我们如何通过一个蒙特卡洛（Monte Carlo）程序来模拟反冲核在液氙探测器中的减速过程，同时计算在碰撞级联过程中，核反冲是如何传递能量给液氙中的电子的过程。

通常来说，通过计算程序来模拟粒子在介质中的穿行过程在几十年前就已经开始了。比如说，大家熟知的 Ziegler 等人开发的 SRIM 程序包，每隔几年就会根据最新的实验和理论数据进行更新 [48]。然而这些程序包多数是通用程序，针对液氙探测器，目前尚且没有特定的程序。在本文中，我们针对暗物质的直接探测实验，尽量改进之前的计算机模拟程序，使其适应低能核反冲的物理图像（大约在几个千电子伏特的能量区域）。当然，所有这些计算机模拟程序，包括我们的，都不是严格意义上的从头计算（*ab initio*）。比如说，介质中电子的激发电离过程就是一个复杂的过程，只有通过量子散射理论才能描述，而当反冲核在介质中穿行的时候，反冲核的带电情况也时刻变化，十分复杂。所有这些任何计算机模拟程序都很难完全模拟成功。而且由于氙原子大量的核外电子（54 个）的存在，整个反冲核的减速过程是一个复杂的多体问题，如何去处理具体的细节已经超出了我们的计算能力范围，我们在此只能对这个过

程做一定简化，使相应的过程能够比较清晰，且易于模拟。对于我们来讲，重要的是上面所阐述的一些效应，可以通过一个平均化量，即电子单位距离能损 $(dE/dx)_{\mathrm{el}}$ 来简化。同时通过与实验数据对比，我们发现我们的模拟在相当程度上接近真实物理过程。

2.2.1 核反冲减速过程的简化

通过第一节的分析我们知道，电子反冲的减速过程中，几乎所有电子反冲的动能最终都传递给了介质中电子。与电子反冲不同，核反冲的减速过程中的能量传递就要复杂得多。一旦液氙探测器中的一个氙原子核被一个大质量弱相互作用粒子所击中，并且在液氙介质中反冲运动的时候，液氙中的原子会产生扰动，电子会被激发或者电离。原则上讲，这是一个量子多体问题，现阶段是不可能精确求解的。因此我们要对这个过程进行相应的简化，从而求出核反冲能量中传递给介质中电子的能量值，该能量值应该与电子反冲的能量相似并且具有可比性，因为二者都是传递给介质中电子的能量。与之前的计算机模拟程序相类似，我们的简化模型中，也认为反冲核在液氙中的运动具有经典的轨道。这是因为氙原子的德布罗意波长在 0.5 到 25 千电子伏特（keV）的能量区间里面还不到 0.0025 埃，这远远小于氙原子的尺度，以及液氙介质中氙原子核之间的距离（大约在 3.5 到 6.2 埃之间)。因此我们可以将反冲核的量子效应忽略掉。更进一步说，我们允许液氙的反冲核在液氙中沿着一条经典的轨道穿行，这个轨道由液氙原子之间的相互作用势 $U(r)$，反冲核的初始动能 E 以及入射反冲核相对目标核的碰撞参数 b 所决定。同时，在反冲在液氙介质中穿行的时候，反冲核与液氙原子的电子云中的电子之间相互作用可以看做是沿着反冲核穿行轨迹的微小的摩擦力。这样做是因为电子的质量远远小于反冲核的质量，因此电子对反冲核的作用远不能改变反冲核的运动方向，而能引起少量的能量损失。因此，我们可以看到，反冲核与液氙中原子核发生作用的时候，几乎可以看做是弹性散射，会引起碰撞级联，同时改变初始反冲核的运动方向，而反冲核与液氙中的电子发生作用的时候，反冲核运动方向几乎不受影响，但是会损失动能给电子，从而引起电子的激发或者电离。这个效应可以看做电子对反冲核的一个微小扰动。在某种意义上上来说，这个跟量子力学中著名的 Born-Oppenheimer 近似相类似。

显然，一个反冲核在液氙探测器中的减速过程中会引起一系列的碰撞，从

而引起次级的反冲核，整个过程类似于一个碰撞级联过程。因此，当我们使用计算机程序模拟反冲核在介质中的减速过程的时候，我们不但需要考虑最初的反冲核，同时还要考虑次级反冲核，甚至更低级的反冲核。在计算机模拟程序中，每一个反冲核都会有一个初始的动能，具有确定的位置以及确定的运动方向。这些我们是在一系列特定约束的情况下随机产生的。我们会在接下来的章节中详细讨论哪些物理条件约束这些模拟参数的的生成。在上一段中我们讲到，一个反冲核在介质中的运动，可以被看做近乎沿着一条直线运动，直到这个反冲核碰到介质中另外一个原子的原子核。当两个原子核发生碰撞时，由于反冲核的速度较低，我们认为该碰撞不会引发核反应，因此两原子核之间的碰撞可以被认为是弹性碰撞。当两原子核发生二体弹性碰撞的时候，初始的反冲核的运动方向会发生改变，同时传递部分的动能给靶原子核。最终结果就是，初始反冲核运动方向改变，动能降低，而靶原子核获得动量，开始在介质中沿一定方向运动，从而成为一个新的次级的反冲核。在此过程中，我们可以近似的认为该碰撞过程，动量传输是在极短的时间内发生的，因此可以认为动量传输是一个离散的过程。而在发生原子核间二体碰撞的同时，原子核外的电子也会与反冲核发生库伦作用，这些核外电子会从反冲核中获取一部分动量，从而被激发或者电离，而反冲核的动量也相应有一定损失。正如我们前文所述，由于核外电子的质量与反冲核的质量非常悬殊，核外电子对反冲的运动方向的影响几乎可以忽略不计，在此我们仅仅将其作为反冲核运动路径上的微小摩擦力来看待。这个摩擦力的大小恰好可以用电子单位距离能损 $(dE/dx)_{\mathrm{el}}$ 来度量。最终，在这两种叠加效应的共同作用下，一个反冲核逐渐减速，最终降低到分子热运动的速度。至此，我们认为反冲核已经与介质中其他的原子核相同，剩下的动能只是热运动的动能。

我们之所以要来模拟反冲核的减速过程，最终是为了计算在核反冲的减速过程中，反冲核的初始动能中，有多少是传递给了介质中的电子。因此，在我们的模拟程序中，我们不去追踪每个反冲核的具体的运动轨迹，而把重点放在反冲核减速过程中的能量损失过程。更进一步说，我们只要记录每一次原子核二体碰撞过程中，反冲核因为核外电子带来的摩擦力而损失的动能。将所有的原子核二体碰撞过程中损失的能量全部加起来，就是最终反冲核损失给介质中电子的能量。根据这个逻辑，我们的程序通过对电子单位距离能损 $(dE/dx)_{\mathrm{el}}$ 沿着反冲核运动路径的积分来计算一次原子核二体碰撞中的电子能损，之后对

所有的能损进行求和，

$$\eta(E_{\rm nr}) = \sum_{i=0}^{N} \int_{0}^{\lambda(E_i)} S_e(E_i) dx \ , \tag{2–4}$$

在上面表达式中，$\lambda(E_i)$ 是一个动能为 E_i 的反冲核两次碰撞中的自由程。而 $S_e(E_i)$ 是电子单位距离能损 $(dE/dx)_{\rm el}$，N 是一个初始动能为 $E_{\rm nr}$ 的反冲核所能够引起的原子核二体碰撞的总次数。很显然，这仅仅是一个简化的模型，因为电子单位距离能损 $(dE/dx)_{\rm el}$ 是一个统计意义上的值，或者说是一个电子与反冲核相互之间量子作用的平均。

2.2.2　原子核二体碰撞的动力学研究

在我们的简化模型中，反冲核传递动能给靶原子的过程是通过原子核二体碰撞模型来模拟的。我们可以把两个原子核想象成弹性玻璃球，在碰撞过程中，一个玻璃球可以击中另外一个玻璃球，从而改变运动方向，而被击中的玻璃球获得了一定速度而运动。当我们具体计算二体碰撞中的能量传递的时候，我们采用经典的弹性散射近似。正是通过弹性散射，反冲核通过动量传输，不断引起新的反冲核，而反冲核本身不断减速，最终形成一个碰撞级联过程。通过二体碰撞的动力学示意图 2–1，我们很容易计算出在一个二体碰撞中，初始反冲核传递给靶原子的能量大小 [52]:

$$T = E_0 \sin^2(\theta_c/2) \ , \tag{2–5}$$

在上面的方程中，T 和 E_0 分别是在实验室坐标系里面，靶原子所获得的动能 (或者说反冲核传递给靶原子核的动能) 以及反冲核的初始动能。图中的散射角 θ_c 可以通过下面的方程求解，为了简便起见，我们求解 θ_c 的时候使用了质心坐标系 [52]

$$\theta_c = \pi - 2b \int_{r_0}^{\infty} \frac{1}{r^2 \sqrt{1 - U(r)/E_c - b^2/r^2}} dr \ , \tag{2–6}$$

方程中，b 是两原子核发生二体碰撞时候的碰撞参数，E_c 是在两原子核在质心坐标系中的能量。积分的下限 r_0 表示的是两原子核二体碰撞过程中的核间最短距离，这个距离可以通过下面的方程来求解:

$$1 - \frac{U(r)}{E_c} - \frac{b^2}{r_0^2} = 0 \ . \tag{2–7}$$

其中的 $U(r)$ 是原子间的屏蔽库伦势，在我们的计算中，我们采用下面形式的屏蔽库伦势，

$$U(r) = \frac{Z^2 e^2}{r} \Phi\left(\frac{r}{a}\right) , \tag{2–8}$$

在上式中，$\Phi(\frac{r}{a})$ 是 Hartree-Fock 屏蔽函数，其中 $a = \frac{1}{2}(\frac{3\pi}{4})^{2/3} \frac{a_0}{2Z^{0.23}}$ 是针对两个氩原子核的 Hartree-Fock 屏蔽半径。在这里 a_0 指的是波尔半径（Bohr radius）。而屏蔽函数也有一个如下所示的经验表达式，该表达式是 Ziegler 拟合了大量的实验数据之后得到的 [48],

$$\Phi(x) = 0.1818e^{-3.2x} + 0.5099e^{-0.9423x} + 0.2802e^{-0.4028x} + 0.02817e^{-0.2016x} . \tag{2–9}$$

在我们的模拟程序中，碰撞参数 b 是根据氩原子在液氩中的空间分布而随机生成。具体的做法我们稍后会详细展开。而二体碰撞的散射角 θ_c 以及动能传递量 T 是根据上面所提到的方程 Eq. (2–6) 和 Eq. (2–5) 来计算的。

两次连续原子核二体碰撞之间的反冲核的运动距离是我们计算反冲核电子能损过程中的另外一个重要的参数。由于核外电子对反冲核的作用力极小，反冲核的运动近似于一条直线，但是会因为两个原子之间相互作用的屏蔽库伦势的作用而稍有弯曲。因此为精确计算反冲核的运动距离的时候，我们需要对反冲核在两次碰撞过程中的运动路径进行曲线积分。在积分之前，我们首先需要确定该路径的起点和终点。在我们的计算程序当中，我们选取了这样两点：我们把路径起点选取在反冲核与上一次碰撞过程中的靶原子核之间距离最短的点，而路径终点选取在反冲核与本次碰撞过程中的靶原子核之间距离最短的点。这样在连续的碰撞中，不会有路线被重复计算，也不会有路线被忽略掉。这样，我们根据两个原子核之间二体碰撞的运动方程，可以通过曲线积分求出。下面的曲线积分反映的就是上述逻辑。其中积分上限 $r = R$ 是两个原子核的初始距离，我们后文会继续讨论，而 $r = r_0$ 是两个原子核所能达到的最近距离。

$$\lambda = \int_{r_0}^{R} \sqrt{dr^2 + r^2 (d\chi)^2} , \tag{2–10}$$

表达适中，$\chi = \theta_c/2$ 是极角。根据方程 Eq. (2–6)，我们可以将 λ 记作：

$$\lambda = \int_{r_0}^{R} dr \sqrt{1 + \frac{b^2}{r^2(1 - U(r)/E_c - b^2/r^2)}} . \tag{2–11}$$

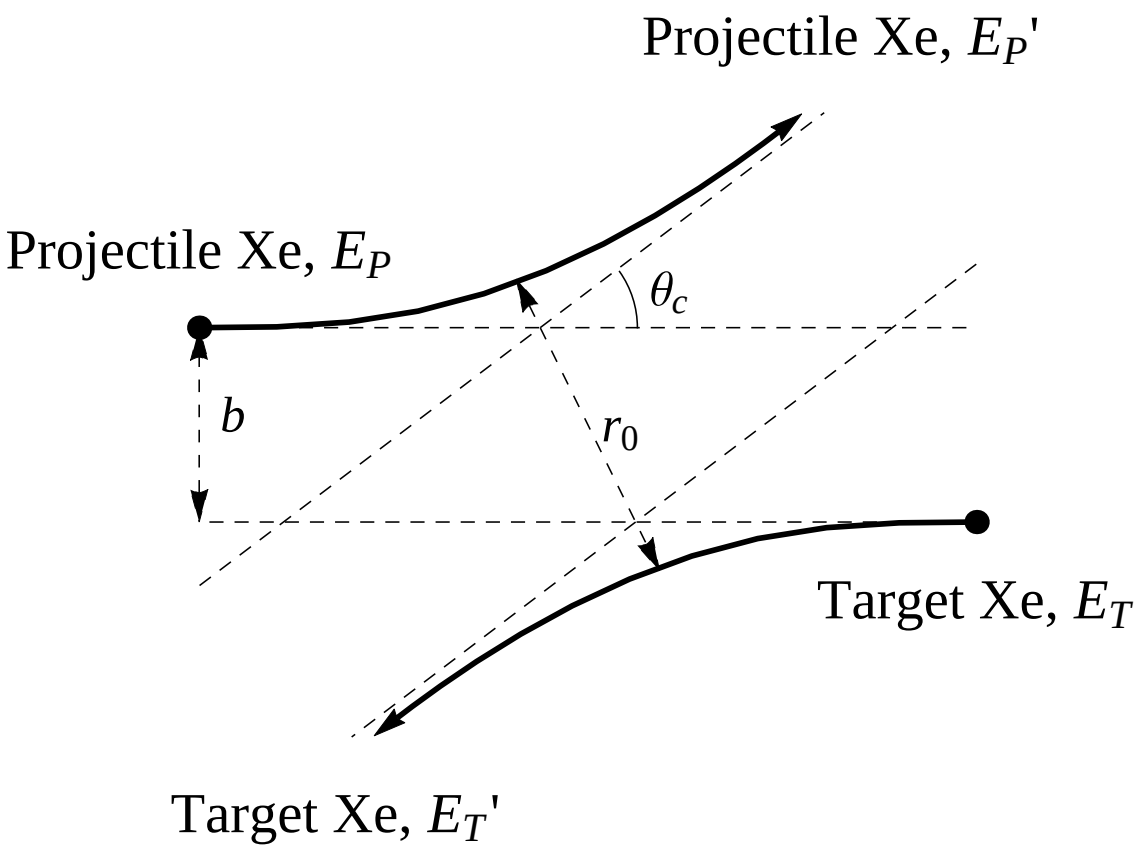

图 2–1 质心坐标系中的原子核二体碰撞的动力学示意图

2.2.3　液氙的径向分布函数

在诸如 GEANT4 [49] 和 TRIM [48] 之类的通用计算机模拟程序中，介质通常被简化为均一的。这些模拟程序根据均匀分布平均生成介质中的原子或者分子。在我们的工作中，我们考虑到液氙介质中原子的空间分布的特殊性，根据液氙的径向分布函数（pair correlation function (PCF)）来生成原子及其相邻的原子。通常来说，径向分布函数分布函数，又叫对关联函数 $g(r)$，由原子间相互作用以及环境温度决定。该关联函数可以通过分子动力学模拟来理论计算，或者通过中子散射实验来测量。在本文中，我们采用的液氙的径向分布函数 $g(r)$ 是来自于文献 [53]。图 2–2显示的就是液氙的径向分布函数 $g(r)$。

我们假设液氙探测器中的某个氙原子突然获得了一个初始动量，该初始动量可能是从一个大质量弱相互作用粒子暗物质粒子处通过弹性碰撞获得，也可

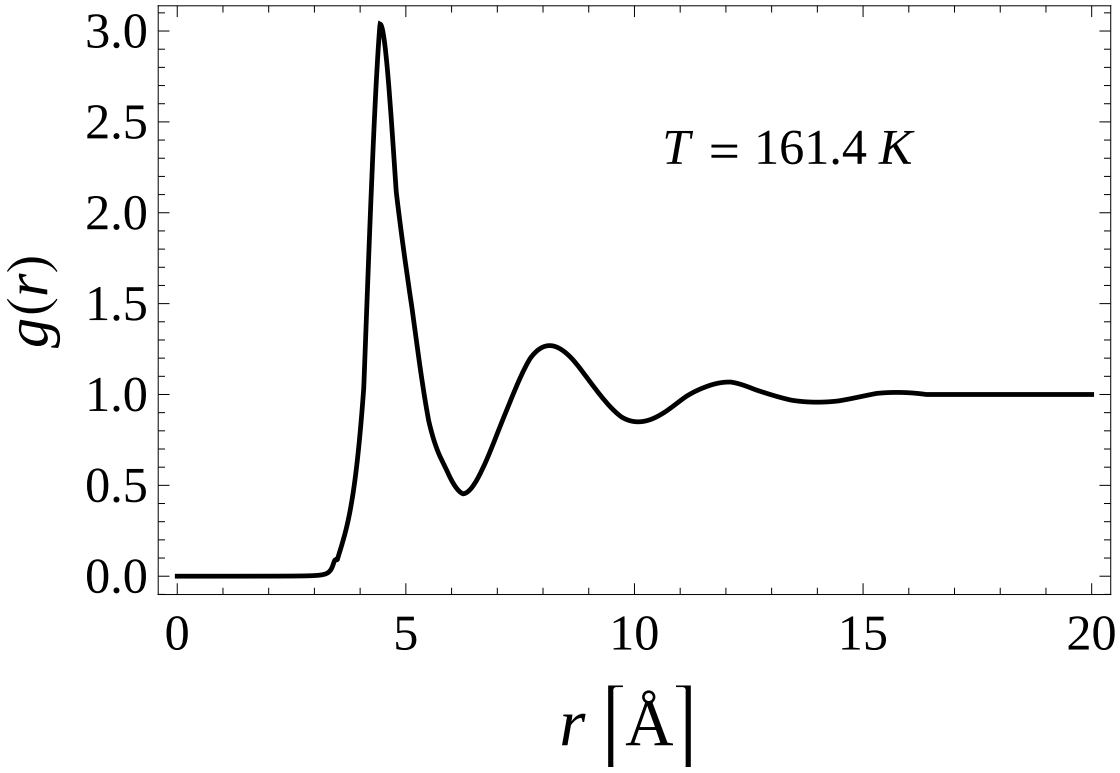

图 2–2 液氩中氩原子的径向分布函数

能是是从另外一个反冲核通过原子核间的二体弹性碰撞获得。于是该氩原子随即变成一个反冲核，从而在液氩探测器中穿行，在穿行过程中会引起原子核间的二体碰撞，以及原子核与电子之间的能量传递。我们先考察这个反冲核发生下一次原子核间二体弹性碰撞的靶原子核。根据液氩中氩原子的空间分布，我们知道，液氩中一个氩原子周围有 11 到 12 个氩原子，因此，在一个反冲核的运动方向前面会有 5 到 6 个氩原子。我们就从这 5 到 6 个氩原子当中挑选这个反冲核下一次原子核间二体弹性碰撞的靶原子核。为了模拟该反冲核运动方向上的 5 到 6 个氩原子，对于每个氩原子，我们至少需要两个参数来确定一个是该氩原子核与反冲核的距离 R，另外一个是该氩原子核与反冲核连线与反冲核运动方向的夹角 Θ。在这里，由于我们假定反冲核是从一个静止位置开始运动，因此我们可以通过液氩中原子空间分布，即径向分布函数 $g(r)$，来确定。在我们的程序中，我们用根据对关联函数 $g(r)$，采用舍选法来随机生成一组原子间的距离。而氩原子核与反冲核连线与反冲核运动方向的夹角 Θ，我们根据

液氙总体的各向同性分布的性质来生成。这里需要注意的是，针对某次原子核间的二体弹性碰撞而言，Θ 角其实是有更强的约束，需要通过对关联函数 $g(r)$ 精确求解。但是对于大量的原子核间的二体弹性碰撞而言，平均效应将弱化上述的约束，因此可以说，我们采用了对 Θ 角采取了一个取巧的算法。这样，通过一组参数对（R，Θ），我们可以成功模拟该反冲核运动方向上的 5 到 6 个氙原子，在我们的程序中，我们选择距离该反冲核最近的氙原子核作为该反冲核下一次二体碰撞的靶子。一旦确定了下一次原子核间二体碰撞的对象，我们很容易根据参数对（R，Θ）来计算这次碰撞的碰撞参数：

$$b = R\sin\Theta\,. \tag{2–12}$$

我们可以看出，我们可以通过程序模拟反冲核运动方向上的 5 到 6 个氙原子，我们选出了下一次原子核间二体碰撞的对象，不断让计算机重复上述过程，我们就可以模拟整个碰撞级联过程。当反冲核被靶原子散射，反冲核的动能部分传递给靶原子核，同时运动方向改变。这样一个反冲核促生了两个反冲核的生成，继而进一步产生更多的反冲核。在两个原子核的二体碰撞过程中，核外电子和反冲核的相互库伦作用也是反冲核速度降低，并且使核外电子获得部分动量。其中核外电子激发或者电离的具体过程，有兴趣的读者可以参阅 Eichler 的专著 [54]，我们在此不作赘述，因为我们采用了一个统计量：电子单位距离能损 $(dE/dx)_{\mathrm{el}}$ 来计算电子能损。需要注意的是，我们并没有关注在此过程中反冲核所带电荷的具体变化，而只是简单的假设反冲核携带着大部分核外电子，这样我们才可以用原子间相互作用势来求解相应的参数。同样因为我们使用统计量电子单位距离能损 $(dE/dx)_{\mathrm{el}}$，希望这是一个好的近似。

另外一个对于模拟很重要的问题是，什么时候认为反冲核是停止的，即当反冲核的动能低于某一预定数值的时候，反冲核不可能继续引起介质中的电子的激发或者电离。这就是一个动力学截断问题，同时之所以一些实验结果被 Collar 等人所质疑 [40]，就是因为没有详细讨论截断能量。在 Collar 的文章 [40] 中，Collar 认为液氙的能带能量差 $E_g = 9.3\ eV$，电子只有在获得高于此能量的情况下才可能被电离。而反冲核与电子相互作用的时候，传递给电子的能量如果可以用经典的二体弹性碰撞来估算，要使电子获得高于 E_g 的能量，反冲核的速度必须要高于 $v_{th} = E_s/2m_e v_F$（在此 m_e 是电子的质量，而 v_F 是液氙中电子的 Fermi 速度）。因此他们估算，当液氙中，反冲核的能量如果低于 20∼40 千电子伏特（keV）的时候，反冲核就无法引起液氙中的电子激发或

者电离。实际上在 Collar 的文章 [40] 中所讨论的截断能量过高了，因为电子的激发或者电离不是简单的经典物理中的弹性碰撞问题，而需要我们考虑量子效应。Ficenec 等人在研究电子被超慢质子激发的时候，曾经讨论过这一量子效应 [55]。他们发现简单通过经典物理中的弹性碰撞模型来估计截断能量，会大大的高估该值。实际上 Ficenec 等人发现，即使质子的能量大大低于通过二体撞模型估计截断能量的时候，仍然会有电子被激发。而 XENON100 也在反冲核能量远远低于 20∼40 千电子伏特（keV）的情况下观测到了液氙的激发和电离现象。

上述所有的争议表明，使用经典的方法来看待一个量子过程是无法得出正确的问题答案的，在将量子物理离散的能量传递，转化为经典物理中连续能量图像的时候，我们必须使用一些统计的手段 [56]。因此，这里的截断能量可以通过我们上文中提到的物理量：电子单位距离能损 $(dE/dx)_{\text{el}}$ 来反应。在我们的程序中，我们使用一个在低能核反冲区快速下降的 $(dE/dx)_{\text{el}}$ 来反应这一物理量的效应，我们会在后文中具体讨论我们所使用的 $(dE/dx)_{\text{el}}$。同时因为我们使用的的 $(dE/dx)_{\text{el}}$ 本什么没有一个截断能量，我们还是要人为的设置一个截断能量。我们是这样来设置的：首先，如果一个初始反冲核的动能低于液氙的能带能极差能带能量差 $E_g = 9.3\ eV$，我们认为该反冲核不可能产生液氙的电离和激发；其次，对于一个已经开始的核反冲过程，我们会认为当反冲核的动量低于液氙的热运动能量（0.021 eV）的时候，该反冲核不在继续产生碰撞级联，从而终止该反冲核的运动，其剩余能量即为热能。

第三章 核反冲的电子能量损失

在介质中穿行的粒子，包括原子或者离子，能够引起介质中电子的激发或者电离，从而损失部分动能，这部分能量损失可以使用一个叫做电子单位距离能损 $(dE/dx)_{\mathrm{el}}$ 的物理量来描述，或者叫做线性能量传输（linear energy transportation），该值等于电子单位距离能损除以介质的密度。正如第二章中所描述的，在计算反冲核在介质中损失给电子的能量的时候，电子单位距离能损 $(dE/dx)_{\mathrm{el}}$（在有些文献中也称之为电子阻止本领，在本文中我们统一称其为电子单位距离能损）是一个非常重要的物理量。原则上讲，电子单位距离能损 $(dE/dx)_{\mathrm{el}}$ 是反冲核的动能的函数。物理学家可以通过实验来进行精确测量。然而，跟发光效率或者电离效率相类似，低能区的实验难度极大，而且实验精度很难保证，所以现有的针对液氙的电子单位距离能损 $(dE/dx)_{\mathrm{el}}$ 的实验数据多数在高能区，只有少数在中等能量区域（大约在 100 千电子伏特左右）。而液氙暗物质探测器所关注的领域恰恰是在低能量区域。因此，在我们的计算当中，我们只能结合理论分析，以及有限的在中等能量区域的实验数据，去估算电子单位距离能损 $(dE/dx)_{\mathrm{el}}$。因为这是我们计算当中一个可能引起较大误差的物理量，我们专门拿出一个章节来讨论这个问题。

在这一章中，我们首先回顾历史上关于电子单位距离能损 $(dE/dx)_{\mathrm{el}}$ 的理论研究，以及存在的理论模型，并拿这些理论模型计算液氙的电子单位距离能损 $(dE/dx)_{\mathrm{el}}$ 同时与实验数据相比较。之后，我们会进一步研究电子单位距离能损 $(dE/dx)_{\mathrm{el}}$，并且修正现有的理论模型，使其预言更加接近实验所观测到的数值。同时我们也给出了我们在计算机模拟当中所使用的电子单位距离能损 $(dE/dx)_{\mathrm{el}}$ 是怎样确定的。

3.1 电子单位距离能损的理论模型

运动的粒子在稠密介质当中穿行，会损失能量给介质。这已经是一个广为关注的问题。一般来说，运动粒子在介质中的能量损失可以分成两部分：一部分是运动粒子损失给介质中原子核的能量，另外的是损失给介质中电子的能量。为了反应这两个量，在物理上引入了原子核单位距离能损 $S_n = (dE/dx)_{\mathrm{nl}}$

(或者被称为核阻止本领) 以及电子单位距离能损 $S_n = (dE/dx)_{\text{el}}$ 两个物理量。通常来说，原子核单位距离能损 S_n 只存在于重离子或者反冲核的情况。而运动粒子损失给电子的能量可以通过电子单位距离能损 $S_e = (dE/dx)_{\text{el}}$ 来表达，为了对比不同密度的介质中的电子单位距离能损，也有人使用线性能量传输这一物理量来表述。该物理量等于电子单位距离能损除以介质的密度，因此与介质的密度无关。早在一个多世纪以前，很多物理学家就已经开展了针对运动粒子在介质中的电子单位距离能损 $(dE/dx)_{\text{el}}$ 的研究 [57]。关于这个课题，科学家们发表了大量的文献，从经典的理论，到量子理论，以及半经典半经验理论等等。从最早的波尔 (Bohr) 的理论开始，相关研究已经得到了极大的进步，包括屏蔽效应，大电荷 (high-order-Z) 以及壳 (shell) 修正，高速量子理论，相对论修正，运动粒子的激发和电离等等，详细的叙述读者可以参考 Sigmund 的综述文章 [58]。综合这些理论，物理学家发明了一个被称之为二体阻止本领理论的方法，该方法能够在比较宽的能量领域比较好的描述实验数据。

然而我们所关心的能量区域很低，我们希望运动氙原子的动能在 1 到 100 千电子伏特 (keV) 之间。在这个能量区间，物理过程变得异常复杂，因为此时我们已经不能使用微扰理论来求解这个问题。在历史上，为了研究低速粒子在介质中的减速过程，科学家们发展出几套简化模型，来计算电子单位距离能损 $(dE/dx)_{\text{el}}$。其中比较有名的是线性响应理论 [59] 和动量传输截面理论 [60]。这两个模型都将介质中的电子想象为均匀的电子气体 [61]，该电子气体符合费米分布。当运动粒子在介质中穿行的时候，运动粒子在发生原子核间的二体碰撞的同时，在均匀电子气体中运动。基于这两种方法的理论计算都给出这样的关系：电子单位距离能损 $(dE/dx)_{\text{el}}$ 正比于运动粒子的运动速度。为了求得更精确的结果，Brandt 等人研究了运动粒子电荷变化的情况，发展出了等效电荷理论 [59]，Echenique 等人研究了运动粒子的核外电子分布，发展出了非线性密度泛函理论 [60]。不管是哪种理论，最终结果都是电子单位距离能损 $(dE/dx)_{\text{el}}$ 正比于运动粒子的运动速度。

3.1.1 动量传输截面理论

为了更好的描述那些运动速度低于介质中电子的费米 (Fermi) 速度的粒子在介质中的减速过程，科学家们提出了所谓的动量传输截面模型。在这个模型中，运动粒子在介质中的运动速度 v 大大低于介质中电子的费米速度 (Fermi

velocity v_F)，同时运动粒子与介质中电子的相互作用可以看做电子被运动粒子的库仑场所散射。由于运动粒子的速度远远小于介质电子的速度，为简化运算，可以近似认为运动粒子的速度为零。这样，由于电子被运动粒子的库伦势场所散射，电子会获得动量，从而引起了运动粒子的动量损耗，而该部分动能损耗可以认为是损失给了介质中的电子。根据这个模型，电子单位距离能损 $(dE/dx)_{\text{el}}$ 可以通过下面的表达式表示：

$$S_e = n_0 v_F \sigma_{tr}(v_F) v \,, \tag{3–1}$$

方程中，n_0 是介质中电子的数密度。该值与介质中电子的费米速度（Fermi velocity v_F）有关，可以通过 v_F 表示：

$$v_F = \frac{(3\pi^2 n_0)^{1/3}\hbar}{m_e} \,. \tag{3–2}$$

在方程 Eq. (3–1) 中，$\sigma_{tr}(v_F)$ 是通常所说的动量传输截面，可以用下面的表达式给出：

$$\sigma_{tr}(v_F) = \int (1-\cos\theta) d\sigma = \frac{4\pi}{k_F^2} \sum_{l=0}^{\infty} (l+1) \sin^2(\delta_l(v_F) - \delta_{l+1}(v_F)) \,, \tag{3–3}$$

方程中，θ 是散射角，而 δ_l 是费米面上的电子被运动粒子的屏蔽库伦势所散射过程中，第 l 分波的相移。如果假定电子气是均匀电子气，即如果电子的数密度 n_0 是一个常量，那么电子单位距离能损 $(dE/dx)_{\text{el}}$ 就正比于运动粒子的速度。

根据动量传输截面模型，同时考虑到运动粒子核外电子的分布情况，Echenique 等人利用非线性密度泛函的方法计算了运动粒子的屏蔽库伦势 [60]，从而计算了不同的运动粒子的电子单位距离能损 $(dE/dx)_{\text{el}}$。他们的结果显示，不同运动粒子电子单位距离能损 $(dE/dx)_{\text{el}}$ 随着运动粒子的核电荷数而发生振荡，这一现象已经被实验所证实。可以说动量传输截面模型对实验给出了精准的预测。

同样的，Lindhard 和 Scharff (L-S) 应该也是根据动量传输截面模型以及经典的散射假定，对低能区的运动粒子的电子单位距离能损 $(dE/dx)_{\text{el}}$ 做了计算 [62]。他们给出了电子单位距离能损 $(dE/dx)_{\text{el}}$ 相对简洁易于计算的表达式：

$$S_e = \sqrt{8}\pi e^2 a_0 \zeta_0 Z N_0 \frac{v}{v_0} \,, \tag{3–4}$$

表达式中，a_0 和 v_0 分别是波尔半径和波尔速度（Bohr radius and Bohr velocity）。ζ_0 是一个经验参数，在 Lindhard 的文章中该参数被设定为 $\zeta_0 = Z^{1/6}$。当然这个参数是与具体模型相关的，不同的模型会导致不同的结果。N_0 是介质中的原子的数密度。需要注意的是，上述的表达式是针对运动粒子和介质是相同的元素的情况，同时介质中的电子分布使用 Thomas-Fermi 分布来估算的。

另外，利用半经典的非弹性能量损失，Tilinin 考虑到碰撞原子核之间的库伦斥力会大大降低运动粒子在介质中的电子能损 [63]。而此时，多数的原子核间的碰撞都是大碰撞参数碰撞，即运动粒子多数被介质中的原子核小角度散射。考虑到这些因素，他修正了 Lindhard 的理论，引入了一个与运动粒子能量相关的参数 $\tau(E)$ 来修正 Lindhard 的表达式，并得到新的电子单位距离能损 $(dE/dx)_{\text{el}}$。根据他的计算结果，电子单位距离能损 $(dE/dx)_{\text{el}}$ 在低能区的随运动粒子动量的下降而迅速降低，电子单位距离能损 $(dE/dx)_{\text{el}}$ 近似于与运动粒子速度的三次方 v^3 而不是运动速度 v 成正比。

3.1.2　线性响应理论

当一个运动粒子在由原子的外层电子组成的电子气中穿行的时候，运动粒子会对电子气体产生微小的扰动，从而形成一个电子密度的局部不均匀化，即电子密度局部发生涨落。由于运动粒子周围的电子气变得不均匀，其中运动电荷运动方向的电子密度会相对比较稠密，因此，在运动粒子周围就会感应形成一个电场。在这个感应电场的作用下，运动粒子沿着运动方向运动需要克服电场力做功，从而运动粒子的动能产生损失。线性响应理论就是基于上述假设，其中运动粒子克服感应电场的电场力所做的功可以认为是运动粒子的动能损失给了介质当中的电子。

基于线性响应理论，理论物理学家们做了大量的计算，其中被广为引用的是 Brandt 和 Kitagawa （B-K）在此基础上所做的改进，即有效电荷理论 [59]。在 Brandt 和 Kitagawa 的文章中，他们对电子单位距离能损 $(dE/dx)_{\text{el}}$ 引入了一个粒子有效电荷的概念。通过有效电荷的概念，一般重核粒子在某介质中的电子单位距离能损 $S_e(Z_1, Z_2; v)$ 可以通过相同速度的质子在相同介质当中的电子单位距离能损 $S_p(Z_2; v)$ 进行估算：

$$S_e(Z_1, Z_2; v) = [Z_1^*(v)]^2 S_p(Z_2; v)\ , \tag{3–5}$$

方程中，Z_1 是要求解的运动重核粒子的原子数，而 $Z_1^*(v)$ 是当运动重核粒子的运动速度为 v 的时候的有效电荷。另外，Z_2 是介质的原子数。因此，只要知道了质子在不同速度下某一介质中的电子单位距离能损 $(dE/dx)_{\text{el}}$，就可以通过 Brandt 和 Kitagawa 的有效电荷理论去计算任何重核粒子在相同介质中的电子单位距离能损 $(dE/dx)_{\text{el}}$。

3.1.3 理论预测与实验数据的对比

虽然理论物理学家们花费了大量的时间精力来研究计算不同粒子在不同介质当中的电子单位距离能损 $(dE/dx)_{\text{el}}$，各种不同理论对电子单位距离能损 $(dE/dx)_{\text{el}}$ 的预言在低能区却不能与实验测量值很好的符合。比如说 Fukuda 等人在 1981 年曾经对惰性气体元素粒子在惰性气体中的电子单位距离能损 $(dE/dx)_{\text{el}}$ 做了实验测量，该测量结果与各种理论预言产生了重大的偏离 [51]，尤其是在能量较低的区域（100 千电子伏特或者更低)。而根据大量的实验数据和不同的理论预测，Ziegler 等人做了大量工作，他们对不同元素的电子单位距离能损 $(dE/dx)_{\text{el}}$ 做出了一个半经验的推荐结果 [48]。他们的结果被集成到一个叫做 SRIM（Stopping/Range Table）的软件包里面。他们的所给出的电子单位距离能损 $(dE/dx)_{\text{el}}$ 结果虽然也跟粒子的运动速度成正比，但是更接近实验数值一些。我们讲不同的理论预测结果和实验数据，包括 L-S 理论，B-K 理论，以及 SRIM 的数据，放到一起，绘制了一副图表：图 3–1。从图中我们可以看出 SRIM 的数据要比 L-S 和 B-K 的预言低得多，但仍然比实验数据要大一些，尤其是在低能区域。而 Tilinin 的计算结果似乎又下降得过快，我们看出该结果远低于实验测量值。总起来说，没有哪个理论结果很好的预言了电子单位距离能损 $(dE/dx)_{\text{el}}$ 在低能区的行为。

3.2 动量传输截面理论的修正

3.2.1 等效电子密度

我们先假设一个慢速运动的粒子在一个电子数密度为 n_0 的电子气体中，以远低于电子气中电子费米速度 v_F 的速度 v 穿行。在这个运动粒子的轨迹上，运动粒子通过库伦作用传递部分动量给电子气中的电子，从而发生了电子能损。而这个运动粒子的轨迹会因为运动粒子与介质中的原子核发生二体弹性碰撞给改变。由于电子屏蔽效应，我们认为运动粒子的轨迹只有在于靶原子接近

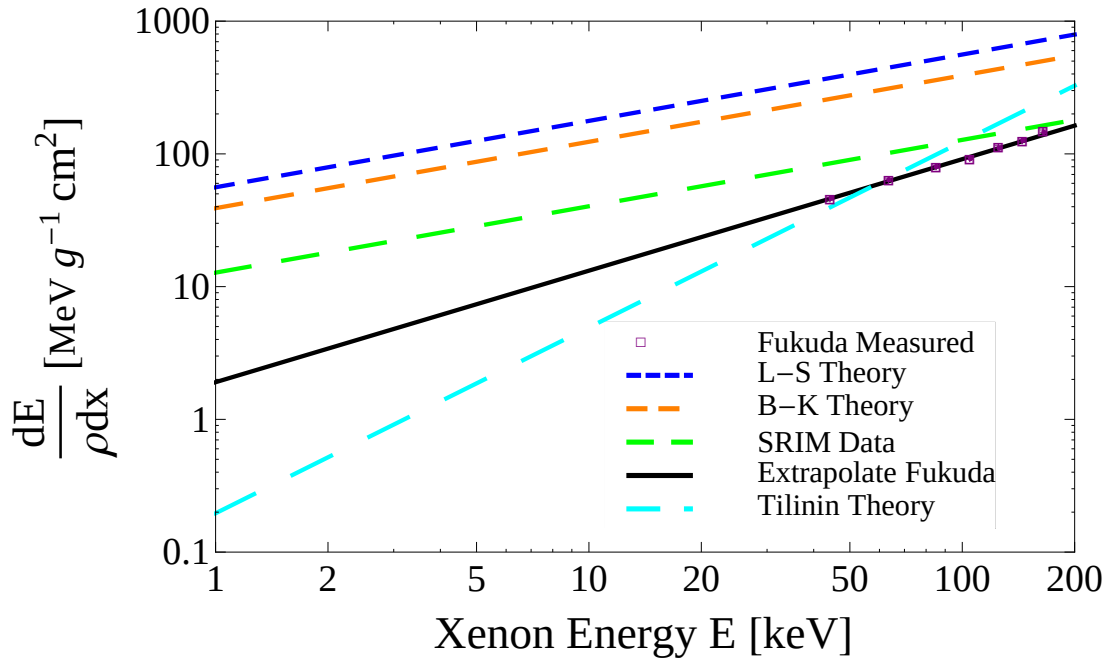

图 3–1 电子单位距离能损的不同理论预言与实验数据的对比 1

到最近距离的时候才显著改变。我们考虑电子气中的电子是被运动粒子本身的库仑场所散射，而电子的动量增加可以通过所谓的动量传输截面 $\sigma_{\mathrm{tr}}(v_F)$ 来计算。通过这个模型，我们可以推导出形如方程 Eq. (3–1) 的电子单位距离能损 $(dE/dx)_{\mathrm{el}}$ 的表达式。如果电子数密度为 n_0 是一个常量，那么动量传输截面理论就可以推导出电子单位距离能损 $(dE/dx)_{\mathrm{el}}$ 与运动粒子的速度 v 成正比。这个结果与其他的理论预言相类似。

对于像金属一样的导体介质来说，其间存在大量自由运动的电子，从而形成基本均匀的电子气，因而动量传输截面理论模型可以对电子单位距离能损 $(dE/dx)_{\mathrm{el}}$ 给出恰当的理论预言。比如说动量传输截面理论模型所预言的电子单位距离能损 $(dE/dx)_{\mathrm{el}}$ 随着运动粒子的原子数发生 Z_1-振荡（Z_1-oscillation） [60, 64]。这是一项了不起的理论预言。然而对于像液氙这样的绝缘体介质，我们是否可以直接使用动量传输截面理论模型来计算电子单位距离能损 $(dE/dx)_{\mathrm{el}}$ 呢？显然我们必须要更加慎重。首先，我们必须思考两个问题：

- 在液氙之类的绝缘体中，电子是否可以被当做均匀电子气来处理？

- 我们应该怎样来估算液氙绝缘体中电子气的电子数密度？换句话说，当一个反冲核在液氙介质中穿行的时候，介质中有多少电子参与到与反冲核之间的反应中来了？

首先，对于类似液态惰性气体的绝缘体，它本身只有少量的自由电子存在(即液氙本身也有能带结构)，大多数的电子都是单个原子的束缚电子。显然，对于被束缚在原子核周围的电子云形成的电子气体，其密度随着电子距离原子核的远近而变化。越靠近原子核的地方，电子气的密度就会越高。其次，当能量较低的反冲核在液氙中穿行，当反冲核与靶原子核发生二体碰撞的时候，低能反冲核所能穿透的电子云深度比高能反冲核要浅。因此，当我们使用动量传输截面理论模型来计算反冲核在液氙中的电子单位距离能损 $(dE/dx)_{\mathrm{el}}$ 的时候，我们应该考虑反冲核所能穿透的电子云的深度，因为只有沿着反冲核路径的电子才会强烈收到反冲核的影响。这样我们就需要根据反冲核的路径，重新计算电子数密度。现在问题的物理图像变得清楚一点：对于类似液氙的绝缘体，要确定动量传输截面理论模型中的电子数密度，我们必须要考虑束缚电子的壳层结构和低能反冲核在液氙中相对靶原子的运动路径。

为了确定绝缘体原子的电子数密度，现存的最基本的模型是 Hartree-Fock (HF) 模型，该模型也被称为自洽场模型（self-consistent field method (SCF)）。但是这种方法非常复杂，使得我们要得到精确的结果，需要投入大量的运算力。因此，我们需要用相对比较容易计算，并且结果比较精确的方法。这里我们可以通过泊松（Poisson）方程来计算束缚电子的电子云的密度分布：

$$\rho(r) = \epsilon \nabla^2 \Phi(r) \,, \tag{3–6}$$

上述方程中，$\Phi(r)$ 是介质中原子周围的势能函数。不管我们将来选用什么势能函数的形式，我们可以看出，电子的数密度讲依赖于电子与原子核之间的距离。距离远远，电子的数密度越小。如果可以选用较为精确的势能函数的形式，我们可以相对精确的计算出电子云的密度分布。

另外，由于低能反冲核很难穿透到深层电子云，我们可以假定原子的核外电子中，只有部分参与到与反冲核的反应中来。考虑到这种情况，我们着重考虑只有沿着反冲核经过的路径上的电子，才会被反冲核显著影响到，从而反冲核的大部分电子能损都是由于这些电子造成的。通过这个假设，我们就可以回答我们上面的问题 2。现在来看，问题变得清晰一点，当一个反冲核在液氙介

质中运动，反冲核的运动路径由原子核之间的二体弹性碰撞确定。而二体弹性碰撞可以由原子间势 $U(r)$，反冲核的动能 E_p，以及二体碰撞的碰撞参数 b 确定下来。同时由于单个电子对于反冲核的作用比较小，我们可以认为反冲核的路径可以由下列方程来确定 [52]:

$$\frac{d\theta}{dr} = -\frac{b}{r^2}\left(1 - \frac{2U(r)}{E_p} - \frac{b^2}{r^2}\right)^{-1/2} . \tag{3–7}$$

注意，这个方程是在极坐标中 $\theta - r$ 的二体碰撞方程。

通过方程 Eq. (3–7) 可以看出，我们可以求解方程 $1 - \frac{2U(r)}{E_p} - \frac{b^2}{r^2} = 0$，求得两个发生二体碰撞的原子核之间的最短距离 r_0。假定在介质中原子的半径是 R，那么运动粒子所能穿透靶原子的电子云的部分为一个半径在 R 到 r_0 之间的一段球壳。我们认为这段球壳中电子会被运动粒子显著影响。于是我们有理由假定，我们求解动量传输截面模型中电子数密度的时候，应该考虑这部分电子。于是我们通过方程 Eq. (3–6) 来计算这些电子的平均密度，我们在本文中称之为该绝缘体在动量传输截面模型中的等效密度。

初始核反冲能量 E_p，以及原子间的作用势 $U(r)$ 我们可以认为是已知的，现在对于运动粒子唯一的遗留问题就是如何确定它与靶原子核的碰撞参数 b。究竟应该选择什么作为求解等效电子密度的碰撞参数 b 呢？显然，对于一个运动方向任意的粒子，不存在某个特定的碰撞参数 b，我们只知道，该碰撞参数不能小于 0，但也不能大于原子在介质中的半径 R。因此，在我们的模型中，我们对于任意的运动粒子的初始能量 E_p，对其计算所有可能的碰撞参数情况下的等效电子密度，然后对之求平均。然后将这个平均的等效电子密度，作为最终的等效电子密度。看来这是可行的近似办法。

3.2.2　氙的电子单位距离能损

现在我们可以根据修正之后的动量传输截面理论模型来计算氙原子在液氙中的电子单位距离能损 $(dE/dx)_{\text{el}}$。在我们的工作中，我们用氙的范德华半径（Van der Waals radius）216 皮米（pm）作为氙原子的半径 R。而为了确定两个原子核二体碰撞的最短距离 r_0，我们使用 Moliere 势作为原子间的相互作用势 $U(r)$。两个原子核发生碰撞的时候，由于运动粒子方向任意，我们认为碰撞参数在 0 到 R 之间均匀分布。基于上述的参数选择，我们可以计算出液氙当中电子气的电子数密度 n_0，从而求出电子气的平均费米速度（Fermi velocity）

v_F。而我们在求解动量传输截面的时候，我们在薛定谔方程中（Schrödinger equation）使用 Moliere 势来计算分波的相移。

最终，我们计算出初始能量在 1 到 100 千电子伏特（keV）的氩反冲核在液氩中的电子单位距离能损 $(dE/dx)_{\text{el}}$。使用指数关系来对计算数据进行拟合，我们得到如下的电子单位距离能损 $(dE/dx)_{\text{el}}$ 表达式：

$$S_e(E_p) = \begin{cases} 2.85 \times E_p^{0.78} & E_p \text{ <50 keV} \\ 5.53 \times E_p^{0.61} & E_p \text{ >= 50 keV} \end{cases} \tag{3–8}$$

我们把相关的计算结果与相应的实验数据进行了对比，我们的计算结果也绘制在图 3–2中。除了我们的结果，我们还绘制了其他一些理论预测结果以及实验数据。其中，蓝色的间断线是 Lindhard-Scharff （L-S）的理论值 [62]；橘色间断线是 Brandt-Kitagawa （B-K）的理论预测值 [59]；绿色和青色的剪断线分别是 SRIM [48] 和 Tilinin 的计算结果 [63]。而红色的点是 Fukuda 在 1981 年的实验数据 [51]。很显然在低能区，电子单位距离能损 $(dE/dx)_{\text{el}}$ 下降的非常迅速。

3.3 实际的电子单位距离能损

虽然如图 3–1所示，我们经过修正动量传输截面理论模型所得出的电子单位距离能损 $(dE/dx)_{\text{el}}$ 与实验测量数据非常接近 [51, 65]，我们仍然希望更加清楚知道理论和实验之间的误差所在。因此我们对实验测量进行了分析。Fukuda 等人在 1981 年的实验中，测量的是在低能区域（40 keV 到 200 keV），氩原子在氩气中的电子单位距离能损 $(dE/dx)_{\text{el}}$。在他们的实验中，氩离子通过 Cockcroft 和 Walton 类型的加速器加速，之后穿过一个充满纯度在 99.9% 以上的氩气的空腔。当氩离子横穿目标之后，他们测量一个静电能量分析仪以此来计算氩原子在氩气中的电子单位距离能损 $(dE/dx)_{\text{el}}$。他们的实验中，氩离子可能发生的多次散射，以及氩离子可能的与氩原子核之间的作用都已经考虑进来。我们把实验的原始数据列在表格 Table (3–1) 里。

自然的，我们需要的是氩原子在液氩中的电子单位距离能损 $(dE/dx)_{\text{el}}$。针对介质的不同形态，许多科研人员曾经做过研究 [66–68]，尤其是对于一些金属气体。根据他们的研究通常来说粒子在气体介质中的电子单位距离能损 $(dE/dx)_{\text{el}}$ 要比其在液体中大大约 50-70%，当然我们剔除了密度因素的影响。

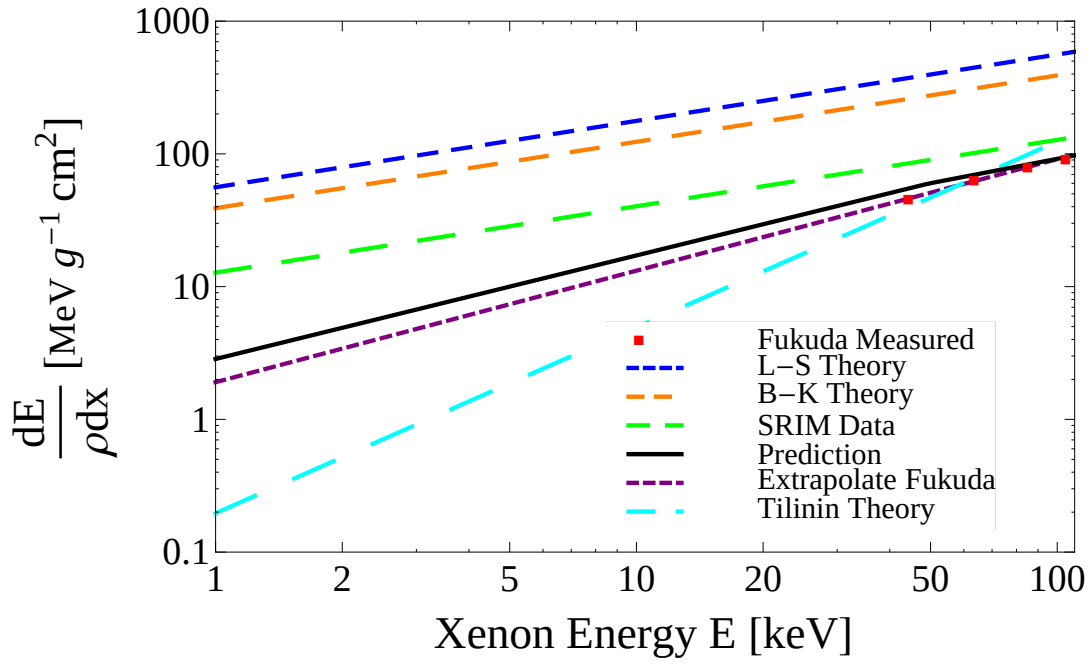

图 3–2 电子单位距离能损的不同理论预言与实验数据的对比 2

然而对于惰性气体元素，由于原子间的范德华力非常的微弱，以至于在不同形态中，惰性气体元素的电子单位距离能损 $(dE/dx)_{\text{el}}$ 几乎不受影响 [48]。因此我们也假定对于氙反冲核，其在氙气或者液氙中的电子单位距离能损 $(dE/dx)_{\text{el}}$ 基本一致。自此我们认为 Fukuda 等人的实验室精确的。

为了计算的精确性，我们假定在我们需要的能量区间（1 到 25 千电子伏特），氙反冲核的电子单位距离能损 $(dE/dx)_{\text{el}}$ 与在实验观测区间的下降趋势相一致。这样使用指数规律 E^{α}，我们对实验数据进行拟合，并把相关的表达式外推到更低的能量区间，这样我们得到实际的氙反冲核在液氙中的电子单位距离能损 $(dE/dx)_{\text{el}}$ 的表达式：

$$S_e(E) = 1.906 \times E^{0.84}\ \text{MeV} \cdot \text{g}^{-1} \cdot \text{cm}^2\ . \tag{3–9}$$

这个结果同样也被绘制于图 3–1中，其中黑色的实线就是这个结果，它位于 Ziegler 和 Tilinin 的结果之间。同时为了估算拟合带来的系统误差，我们采用下面的两种方式：

Gas	Xe^+ energy (keV)	Stopping Power (10^{-15} eV cm^2 atom^{-1})
Xe	44.22	9.98±0.20
	63.43	13.85±0.27
	85.07	17.43±0.35
	104.68	20.18±0.40
	124.89	24.62±0.48
	144.68	27.34±0.54
	164.54	32.26±0.63

表 3–1 实验测量的动能为 40-200 keV 的氙离子在氙气中的单位距离电子能损

方法 A，随机选择误差在 2σ 范围内的点，然后针对这些点做拟合。下面是具体步骤：

- 对于每一个试验点，在实验误差的 2σ 区间内随机生成 10,000,000 数字。举例来说，对于 44.22 千电子伏特（keV）的试验点，其电子单位距离能损 $(dE/dx)_{\text{el}}$ 是 45.77 MeV$\cdot$g$^{-1}\cdot$cm^2，而 2σ 误差范围是 $\pm$1.84 MeV$\cdot$g$^{-1}\cdot$cm^2。于是我们在 45.77+1.84 和 45.77-1.84 之间随机生成 10,000,000 个数字；
- 从上述生成的 10,000,000 数字中，我们对每个试验点随机挑选一个数字，这样组成一组新的数据；
- 对第二步中生成的新的一组数据进行数据拟合，并且得到新的电子单位距离能损 $(dE/dx)_{\text{el}}$ 表达式；
- 重复上述步骤 1,000 次，从而获得 1,000 个电子单位距离能损 $(dE/dx)_{\text{el}}$ 表达式；
- 讲上述生成的 1,000 个电子单位距离能损 $(dE/dx)_{\text{el}}$ 表达式绘制在一起，从而得到电子单位距离能损 $(dE/dx)_{\text{el}}$ 的 2σ 误差区域我们将结果绘制在图 3–3中。

方法 2，使用 χ^2 分布来做误差约束。下面是具体步骤：

- 根据我们的测试以及理论预测，电子单位距离能损 $(dE/dx)_{\text{el}}$ 表达式中的指数 N 应该在 0.5 到 1.5 之间，而系数 K 应该在 1 和 3 之间。这样我们

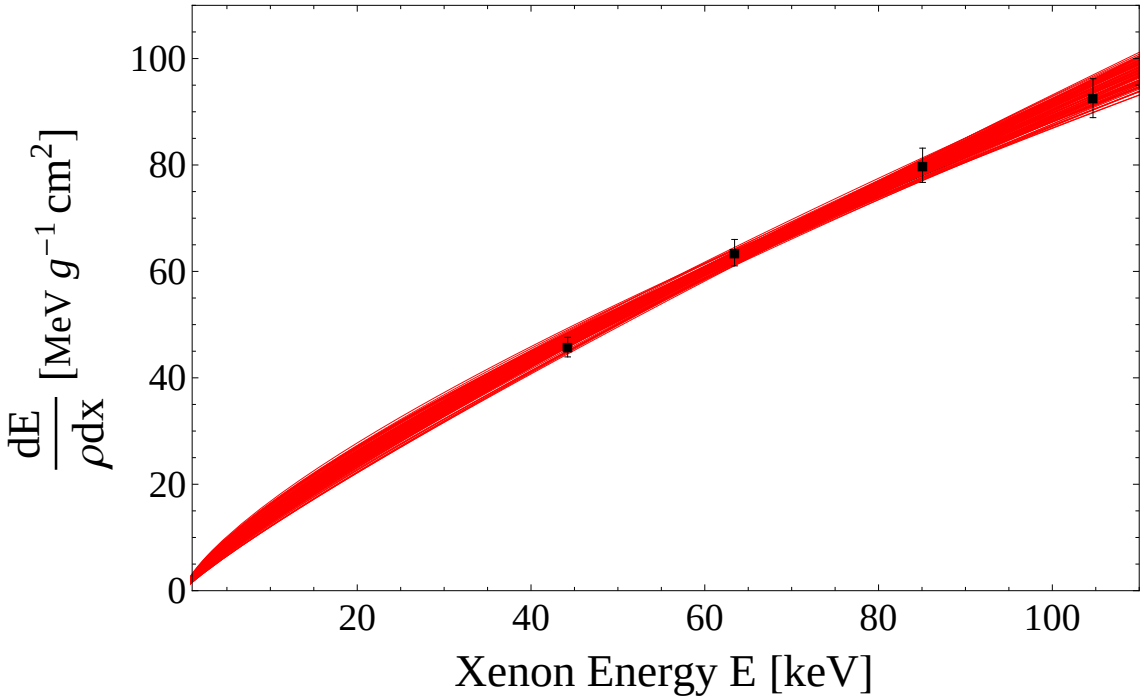

图 3–3 电子单位距离能损的 2σ 误差 1

在 0.5 到 1.5 之间为 N 随机生成 10,000,000 个数字，而在 1 和 3 之间为 K 也随机生成 10,000,000 个数字；

- 从上面随机生成的数据中，随机挑选一组值，组成新电子单位距离能损 $(dE/dx)_{\text{el}}$ 表达式；
- 使用 χ^2 分布来检验新生成的电子单位距离能损 $(dE/dx)_{\text{el}}$ 表达式是否在实验测量的 2σ 误差区间。
- 重复上述步骤 100,000 次，我们获得大约 600 个电子单位距离能损 $(dE/dx)_{\text{el}}$ 表达式的表达式都满足实验测量的 2σ 误差区间。我们把满足条件的 K-N 组合绘制在图3–4中；
- 我们把所有满足条件的电子单位距离能损 $(dE/dx)_{\text{el}}$ 表达式绘制在图 3–5中；

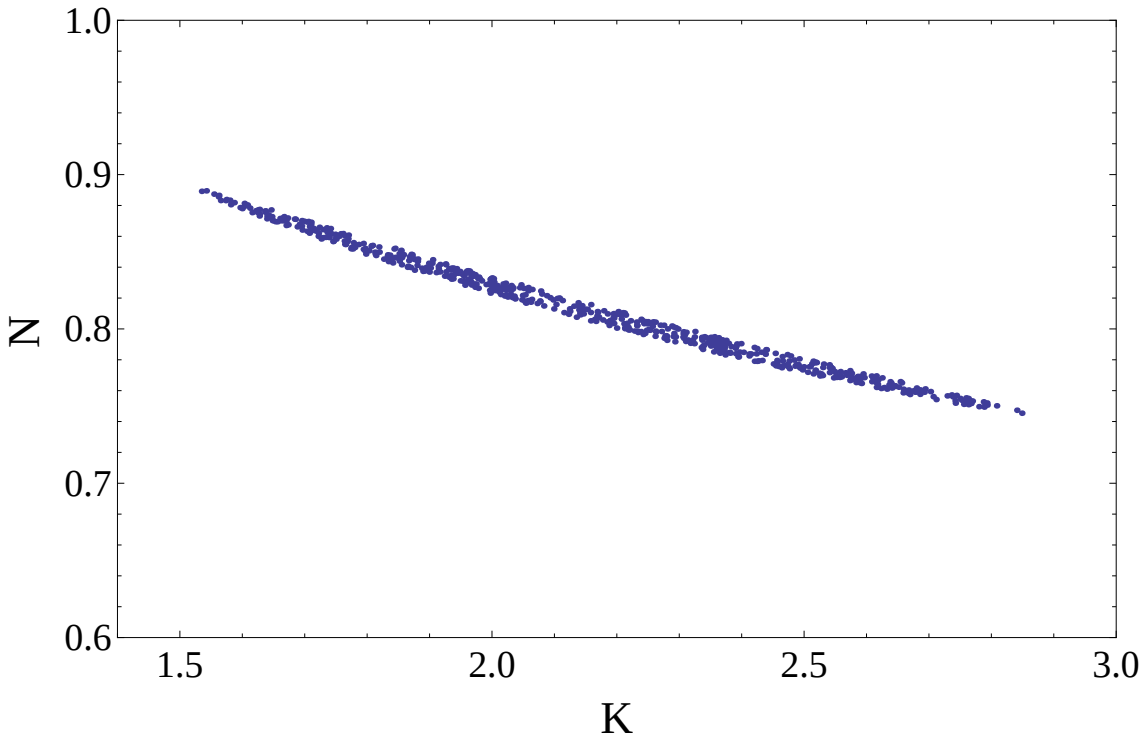

图 3–4 满足 2σ 误差范围的 K-N 分布和关联

进一步来看，我们把图 3–3和图 3–5叠放在一起，我们发现通过两种方法得到的电子单位距离能损 $(dE/dx)_{\mathrm{el}}$ 的 2σ 误差区间几乎是相同的。这个结果现在在图 3–6中。

在本文中，我们的模拟程序采用的电子单位距离能损 $(dE/dx)_{\mathrm{el}}$ 表达式就是由实验数据拟合而来，而上述的 2σ 误差区间作为电子单位距离能损 $(dE/dx)_{\mathrm{el}}$ 的系统误差来看待。

3.4 电子能损和 Lindhard 系数

一旦我们有了电子单位距离能损 $(dE/dx)_{\mathrm{el}}$ 的表达式，我们掌握了反冲核在液氙中的运动轨迹，我们就可以计算反冲核在液氙中每一次二体碰撞的的电子能损。把所有的二体碰撞中的电子能损加起来，我们最终可以得到一个反冲核在液氙中总的电子能损 $\eta(E_0)$。

通过我们上一章和本章前面的结果，我们可以通过蒙特卡洛模拟来计算

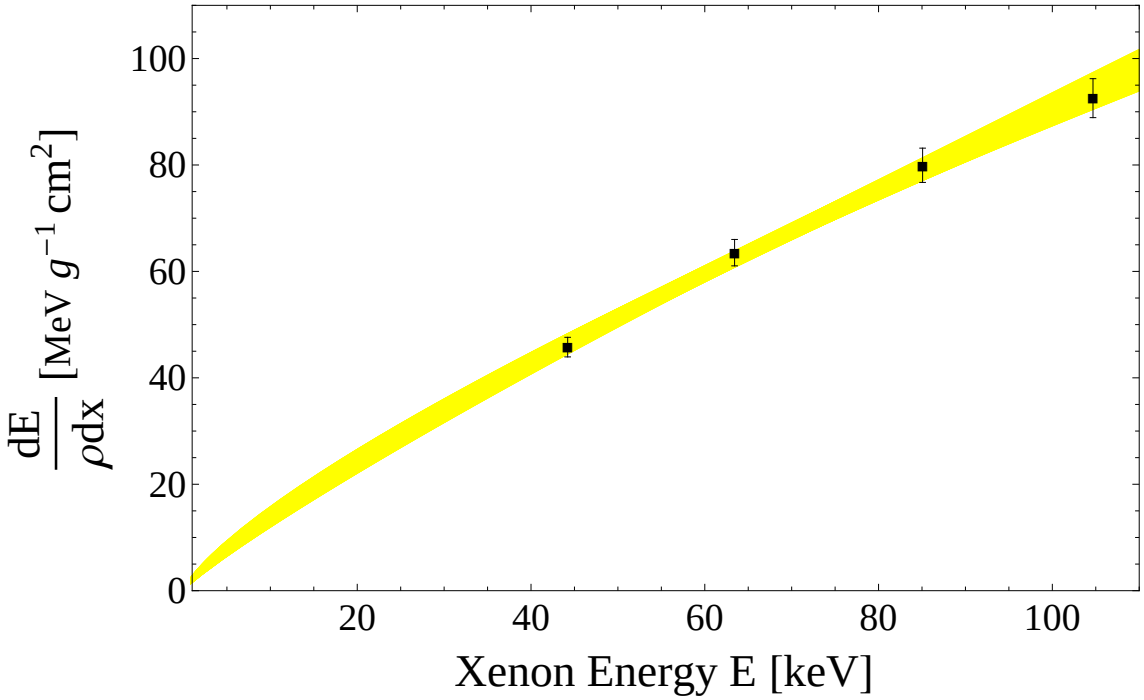

图 3–5 电子单位距离能损的 2σ 误差 2

Lindhard 系数 q_{nc}。在我们的计算中，我们模拟了 10,000 次的核反冲时间，从而得到一个 0.5 到 25 千电子伏特（keV）之间的 Lindhard 系数 q_{nc} 的平均值，其与反冲核的初始能量之间的关系可以用下面的表示来反应：

$$q_{\mathrm{nc}}(E_{\mathrm{nr}}) = \frac{e^{-0.033E_{\mathrm{nr}}^{-0.958}}}{1 + 13.789E_{\mathrm{nr}}^{-0.189}} \,. \tag{3–10}$$

我们将我们计算所得到的 Lindhard 系数绘制在图3–7中。其中黑色实线是我们的结果，而实线周围的阴影区域是我们的 2σ 系统误差。为了校准我们的程序，我们曾经使用 SRIM 的相应参数来复现 TRIM 的结果。我们把相关的工作也绘制在图3–7中。其中绿色的间断线是 TRIM 的结果，而紫色的间断线是我们复现的结果。二者之间的微小差异应该来自于我们使用了相对真实的液氙原子的空间分布。同时，我们也把其他科研人员经常引用的 Lindhard 系数 [45–47] 绘制在一起。图中蓝色的间断线就是令 $k = 0.166$ 的结果。可以看出，我们所计算的 Lindhard 系数 q_{nc} 是最小的。这个从原则上是更接近事实。因为我们的 Lindhard 系数 q_{nc} 比试验观测的液氙的相对发光效率 $\mathcal{L}_{\mathrm{eff}}$ 要低，这

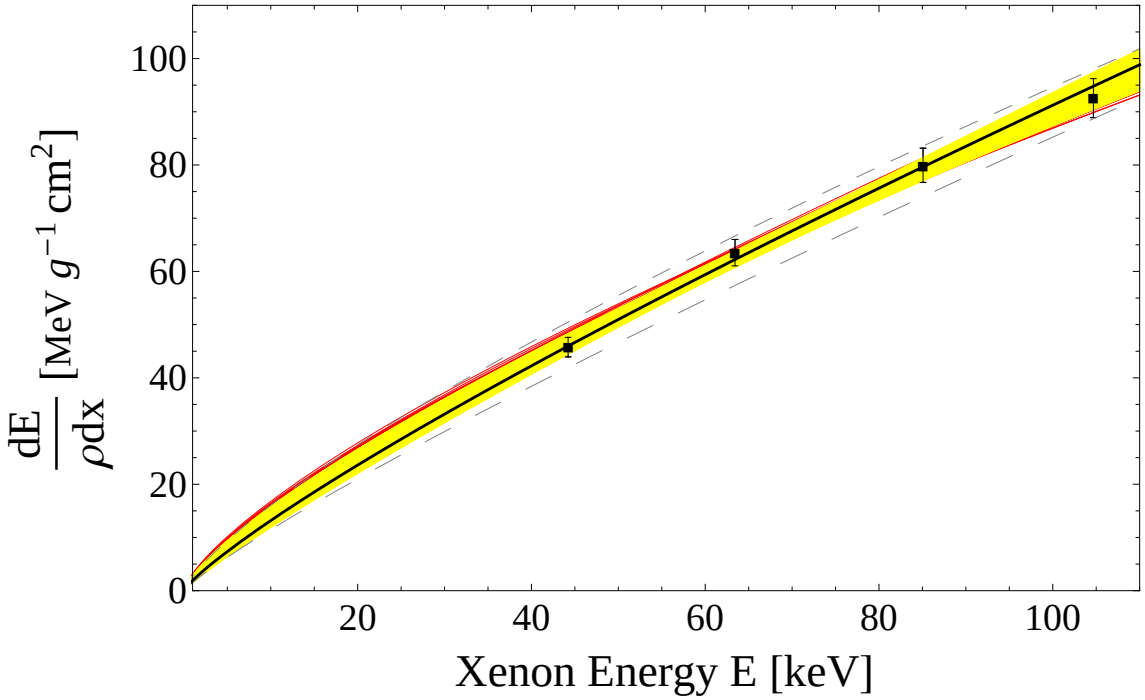

图 3–6 电子单位距离能损的 2σ 误差区域

个与核反冲的发光效率要高于电子反冲的发光效率这一事实相符合。这一现象我们将在后文给出更具体的说明。

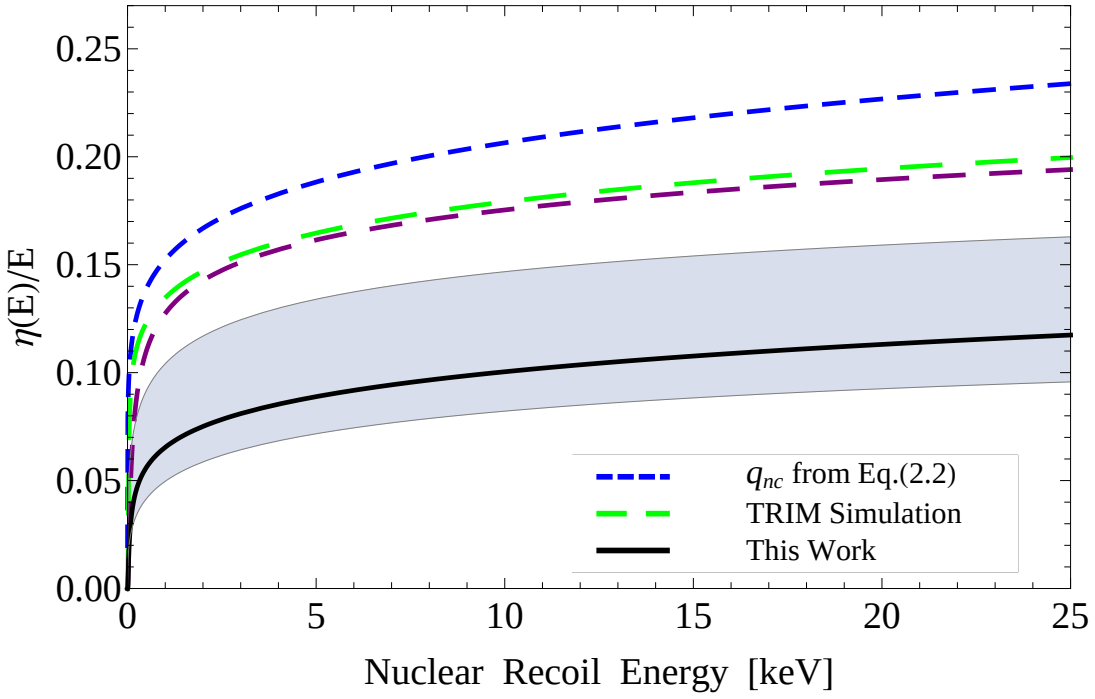

图 3–7 不同理论模型下液氙探测器的 Linhdard 系数 q_{nc}

第四章　液氙探测器中的电子和正离子的重新结合

显然根据前面两章的讨论，通过计算机模拟，我们已经可以顺利获得液氙探测器中，具有一定动能的反冲核的等效电子能量。现在我们需要考虑的问题是液氙探测器的发光和电离过程。只有在了解了这个过程之后，我们才可以具体计算液氙探测器的核反冲事件的光信号 S1 和电离信号 S2 的大小。

在这一章当中，我们首先分析液氙探测器的发光和电离产生的过程。之后我们对液氙探测器中光信号和电离信号的反向关联现象作了研究，发现该现象是由探测器中电子和正离子的重新结合而导致的。之后，我们对探测器中电子和离子的结合过程做了进一步研究，并对现有的 Thomas-Imel 理论模型做了推广，使其可以解释核反冲信号产生的电子和离子对的结合过程。

4.1　液氙探测器的发光和电离过程

4.1.1　激发原子，自由电荷和 Platzman 方程

对于任何在介质中穿行的运动粒子而言，当其最终在介质中减速至热运动的速度时，该运动粒子会在介质中激发电离部分电子，生成一定数量的激发原子，自由电子和正离子对。早在 1961 年，Platzman 就曾经根据能量守恒定律提出过一个方程用以解释这个过程中产生的激发原子，自由电子和正离子对 [69]。Platzman 假定所有的电子能损可以分成三部分，分别用于产生电离的电子和正离子对，被激发的激发原子，以及一些热电子（sub-excitation electrons）：

$$E^{ee} = N_i E_i + N_{ex} E_{ex} + N_i \epsilon \,, \tag{4–1}$$

在方程中，E^{ee} 表示运动粒子在介质中损失给电子的能量，对于电子反冲事件，该量为电子反冲的能量，而对于核反冲事件，该值等于核反冲的初始动能与 Lindhard 系数的乘积，即我们所说的核反冲的电子能损。N_i 是所生成的电子和正离子对的数量，而每生成一对电子和正离子对，平均需要耗费大小为 E_i 的电子能损。同样 N_{ex} 是所生成的激发原子的数量，而每生成一个激发原子，平

均需要耗费大小为 E_{ex} 的电子能损。ϵ 是热电子的平均动能，在实际计算中，该值经常被吸收到 E_{ex} 和 E_i 当中。

这个方程最早是为高能射线所提出，在其原始的文献当中，Platzman 并没有对各个物理量的具体值进行分析，而只是给出了一个大致的估计值。而随着技术的发展，在液氙中物理量 E_{ex} 和 E_i 可以被许多实验通过光学手段精确测量出来。然而对于物理量 N_{ex} 和 N_i 的大小至今仍然存在争议。就比值关系 N_{ex}/N_i 而言，一些文献中声称对于电子反冲事件，其理论值约为 0.06 [70]，而有实验测量该值约为 0.2 [71]。而对于核反冲事件由于 Lindhard 系数的不确定性，一些研究人员给出其值大约为 1 左右 [29, 72]。但是这个结果更多的是来自于较大的 Lindhard 系数 q_{nc} 的结果，而这与我们所分析的 $q_{nc} \leq \mathcal{L}_{\mathrm{eff}}$ 相矛盾。当今的主流观点认为，N_{ex}/N_i 是一个与反冲事件类型相独立的值，即无论电子反冲或者是核反冲，N_{ex}/N_i 应该是相同的 [71]。当然，由于核反冲事件的电子能损无法直接测量，对于这种说法也没有强有力的实验支持。无论如何，所有通过电子反冲实验测量的 N_{ex}/N_i 值都在 0.06 到 0.2 之间。

现在我们可以来研究发光和电离的过程。在理想条件下，每个激发原子通过退激发，可以产生一个光子，而每一个被电离的自由电子，在外加电场的作用下，会漂移到云室而产生一个自由电子事件。然而真实的物理过程却相对复杂，我们发现，即使加上足够高的外加电场，总是有部分被电离的自由电子，会与液氙介质当中的正离子重新结合，形成激发态的氙，自由电子产生了光子。这个过程可以用下面的方程来表示 [29]:

$$\begin{aligned}
&\mathrm{Xe}^{+} + \mathrm{Xe} \rightarrow \mathrm{Xe}_2^{+}, \\
&\mathrm{Xe}_2^{+} + \mathrm{e}^{-} \rightarrow \mathrm{Xe}^{**} + \mathrm{Xe}, \\
&\mathrm{Xe}^{**} \rightarrow \mathrm{Xe}^{*} + \mathrm{heat}, \\
&\mathrm{Xe}^{*} + \mathrm{Xe} + \mathrm{Xe} \rightarrow \mathrm{Xe}_2^{*} + \mathrm{Xe}, \\
&\mathrm{Xe}_2^{*} \rightarrow \mathrm{Xe} + \mathrm{Xe} + \mathrm{h}\nu.
\end{aligned} \tag{4–2}$$

因此，在实验上应该可以观测到发光信号 S1 和电离信号 S2 的反关联的现象。

4.1.2 S1 和 S2 信号的反关联现象

看起来在知道了 Platzman 方程之后，我们可以很容易求得所产生的光子或者电子的数量。事实却并非如此，真实的物理过程远非这么简单。当反冲核在

液氙介质中停止运动之后，从氙原子中电离出来的电子会在相互静电作用下发生扰动，而随机运动。这样带相异电荷的电子和正离子就有机会相互靠近，当两者接近到一定程度之后，便有机会重新结合成为一个中性的但是激发状态的氙原子。当然，如果此时有外加电场的存在，在外加电场作用下，电子和正离子会向相反方向运动，从而相互结合的概率会大大降低。外加电场越高，电子和正离子相互结合的概率就会越低。但是无论外加电场强度有多大，总会有部分的电子和正离子会相互结合。也即使说，电子漂移脱离正离子与电子和正离子相互结合两个事件同时存在。于是，如果增加外加电场，液氙探测器的发光信号 S1 会减弱，而电离信号 S2 会增强。反之，发光信号 S1 会增强，而电离信号 S2 会减弱。我们称此现象为 S1 和 S2 信号的反关联现象。

因此液氙探测器的光信号和电离信号是互相影响的，从而给我们的具体计算带来巨大的麻烦。最早在 2007 年，Aprile 等人曾经对液氙探测器的 S1 和 S2 信号的反关联现象做过研究 [73]，之后 Sorensen 曾在文献 [74] 中对此现象做了进一步分析。要确切知道二者之间的关系，我们需要做进一步的研究。

4.2　电子和正离子对结合的理论研究

要想分别精确估算液氙探测器的发光信号 S1 和电离信号 S2 的产生，我们必须深刻理解自由电子和氙正离子在液氙探测器当中的结合过程。只有这样，我们才能正确的解读液氙探测器中所产生的各种数据。然而直到今天，科研人员还无法彻底理解自由电子和氙正离子在液氙探测器当中的相互结合过程。唯像的说，我们可以把液氙探测器中的这个相互结合过程大致分为如下的三类：

- 初始结合（Initial Recombination）初始结合指的的是当一个电子从一个原子中激发出来之后，介质中产生一个自由电子和一个氙正离子。自由电子在介质中随机运动，又重新与原来的氙正离子重新结合成为中性激发原子的过程。如果液氙探测器没有外加的电场，多数的电子和氙正离子相互结合都是初始结合；

- 批量结合（Bulk Recombination）批量结合指的是当有限空间里面存在一定数量的自由电子和氙正离子，这样自由电子的随机运动会与该空间里面的氙正离子随机结合，而形成中性激发原子的过程。这类过程发生的几率通常与该空间里面自由电子和氙正离子的密度直接相关；

- 定向结合（Columnar Recombination）定向结合指的是当外加电场存在的情况，自由电子和氖正离子向相反的方向漂移，而漂移过程中自由电子和氖正离子有可能相互接触而相互结合。因为这种结合方式通常发生在能量相对较高的运动粒子产生的一束密度较大的电离带中，因此又被称作圆柱结合。

唯象的，我们对自由电子和氖正离子的结合有了一定了解。接下来我们来回顾一下历史上关于这个过程的一些理论假说。事实上，大多说相关的理论都是唯象的，需要引入若干自由参数。一百多年来，大量的科研人员对这个问题做出了研究，包括 [75–81]，并提出若干理论模型。在所有这些理论模型中，Thomas 和 Imel 针对液态惰性气体元素氩和氖做了特定的研究 [79]，他们给出的理论预言结果很好的符合了实验测量的电子反冲事件以及 α 反冲事件中产生的可收集到的电子数量。

4.2.1 对于电子反冲事件的 Thomas-Imel 模型

最早的正离子和电子的扩散方程是由 Jaffe 在 1940 年提出的 [77]。基于这组基本方程，Thomas 和 Imel 对如果求解方程做了进一步的近似和假设：

$$\begin{aligned} \partial_t n_i^+ &= -\mu_+ \vec{E}_d \cdot \nabla n_i^+ + d_+ \nabla^2 n_i^+ - \alpha n_i^- n_i^+ \,, \\ \partial_t n_i^- &= -\mu_- \vec{E}_d \cdot \nabla n_i^- + d_- \nabla^2 n_i^- - \alpha n_i^+ n_i^- \end{aligned} \tag{4–3}$$

方程中，$\mu_\pm$ 分别是正离子和电子在外加电场下的平均移动性能，$d_\pm$ 和 α 分别是针对正离子和电子的扩散和结合系数，这些参数都是无法先验确定的。为了简化方程的求解，Thomas 和 Imel 忽略了方程中的扩散相关的项，同时他们认为由于氖正离子的质量远远大于电子的质量，因此氖正离子的漂移项也可以忽略不计。同时，Thomas 和 Imel 给方程一个特定边界条件，最终他们得到了如下的结论：

$$\frac{Q}{Q_0} = \frac{N_i^{\mathrm{esc}}}{N_i} = \frac{1}{\xi}\ln(1+\xi); \qquad \xi = \frac{n_i \alpha}{4a^2 \mu_- E_d} \,, \tag{4–4}$$

上述表达式中，$\alpha/(4a^2\mu_-)$ 是一个由介质的介电常数，电子的移动性能以及电离的空间分布来决定的常数。

因为这个结论是在忽略了所有的扩散过程而得出的，对于较高电场的情况相对比较较精确。而对于电场不那么高的情况下，实验观测到仍然有大量的电子因为扩散作用而脱离于氖正离子的结合。

方程 Eq. (5–2) 大致可以描述液氙介质中，自由电子和氙正离子的相互结合的概率与外加电场之间的依赖关系。正如我们所阐述的，这个结论忽略了电子因为扩散作用而脱离于氙正离子的结合。在液氙中，当某个电子从价带被激发或者电离到导带，这个电子成为了自由电子，并且在外加电场的作用可以自由漂移。在低电场的条件，电子的漂移速度 v_d 几乎与电场强度 E_d 成正比，其中电子的移动性能 μ 是二者之间的比例系数，即 $v_d = \mu E_d$。在高电场的条件下，对于液氙大约是 10 kV/cm [82]，电子的漂移速度达到一定值之后开始变得与外加电场强度无关，即饱和现象产生了。但是在低电场条件下，除了电子的漂移现象，电子同时会发生扩散，我们可以认为其平均速度为 v_0。通过扩散作用，自由电子仍然有可能脱离于氙正离子的结合。因此为了得到更加精确的结果，在应用 Thomas 和 Imel 的结果的时候，我们应该在 ξ 中加上关于电子扩散的项 μ_E_d。同时，我们使用电子单位距离能损 $(dE/dx)_{\text{el}}$ 或者线性能量传输 LET 作为电荷密度的一个估计，我们可以得到修正后的 Thomas 和 Imel 方程中的 ξ 的如下结果：

$$\xi = \frac{n_i \alpha}{4a^2(\beta v_0 + v_d)} \equiv \frac{K_1}{1 + K_2 \times E_d} \left(\frac{dE}{dx}\right)_{\text{el}}, \tag{4–5}$$

表达式中，β 是一个不确定的参数。

假定 K_1 是一个与电场强度无关的参数，通过实验测量的液氙中光子数量与 LET 之间的依赖关系的数据 [83]，我们可以得到 $K_1 = 2.53\ \text{MeV}^{-1}\cdot\text{g}\cdot\text{cm}^{-2}$。然后，我们可以通过实验测量的电子反冲或者 α 反冲事件中产生的光子和电子数量 [13]，我们可以得到 $K_2 = 3\ \text{KV}^{-1}\cdot\text{cm}$。我们把结果绘制在图 4–1中。

从图 4–1中，我们可以清楚的看出，不管是具有较低 LET 值的电子反冲事件，或者具有较高 LET 值的 α 反冲事件，所产生的电子数量都与外加电场直接相关。Thomas-Imel 方程成功的预测了这个电场依赖关系。方程表明，电子反冲或者 α 反冲事件在液氙探测器中产生的电子数，与外加电场，与反冲事件的电子单位距离能损 $(dE/dx)_{\text{el}}$ 直接相关。

4.2.2　对于核反冲的 Thomas-Imel 模型的推广

然而当我们对核反冲事件应用 Thomas-Imel 方程的时候，我们发现结果变得不那么美好。实验观测发现，核反冲事件在液氙探测器中产生的电子数与反冲事件的电子单位距离能损 $(dE/dx)_{\text{el}}$ 的相关性仍然存在，但是与外加电场的相关性却变得不那么明显 [13]。因此，在 Thomas-Imel 模型当中，一定有一些

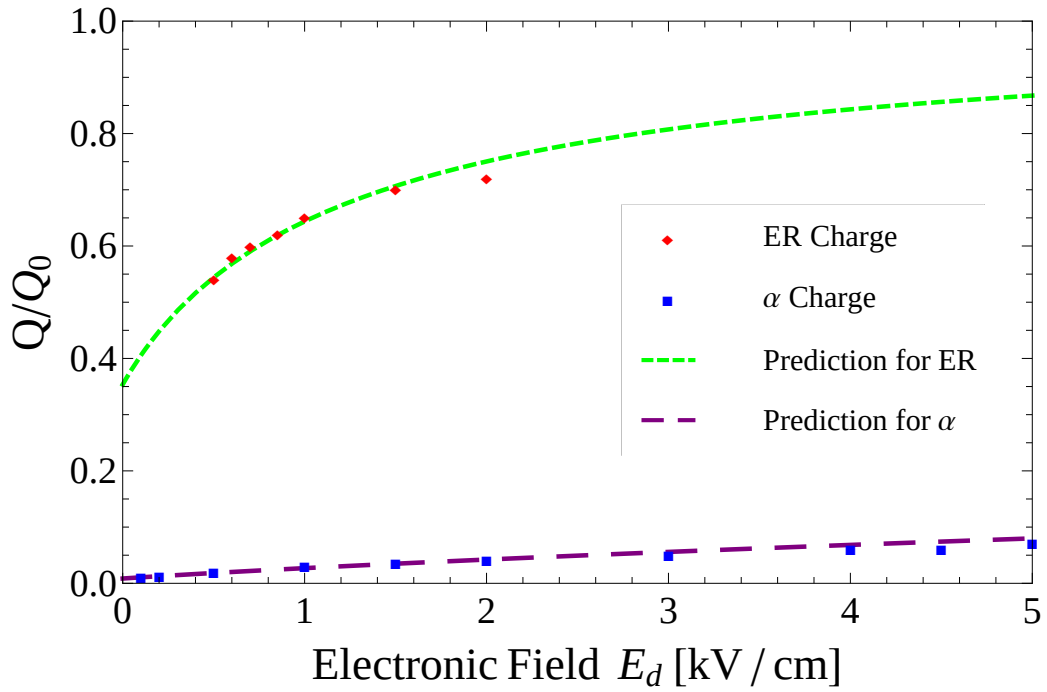

图 4–1 电子反冲核 α 反冲事件电离效率

物理效应没有被考虑进来，而这些物理效应有可能会减弱核反冲事件在液氙探测器中产生的电子数外加电场的相关性。

Chepel 等人分析过电子反冲和 α 反冲事件的路径的结构 [84]。他们发现，无论电子反冲还是 α 反冲，在液氙探测器都具有一条线状（或圆柱状）的路径。如果在液氙探测器上外加电场，沿着反冲粒子的路径上的电子很容易就脱离该路径，而漂移到云室当中。但是对于核反冲事件，反冲核路径的精确结构我们还不太清楚。但是公认的是，核反冲事件中，反冲核的路径更加类似于一个树状的结构，而不像一条线。这些可以被计算机模拟来显示出来 [48, 85]。由于大量的次级反冲核的存在，这些次级反冲核的路径围绕在初始反冲核的路径周围。虽然次级反冲核的路径上面产生的自由电子的密度远低于初始反冲核的路径上自由电子的密度，但是正如静电屏蔽现象，这些相对比较稀薄的电子可能会强烈的屏蔽了初始反冲核的路径上大量自由电子对外加电场的反应。而这恰恰可能就是核反冲事件在液氙探测器中产生的电子数外加电场几乎无关的主要原因。当初 Thomas-Imel 在求解扩散方程的时候，采用的边界条件是一个

盒装的体积元。在该体积元里面存在着电子和氙正离子。这个边界条件对于电子反冲和 α 反冲都比较恰当。但是对于核反冲事件，这就忽略了反冲核路径的空间分布。根据这个假设，我们通过在 ξ 中引入一个电场屏蔽系数 S 的方式来对 Thomas-Imel 方程进行修正：

$$\xi = \frac{K_1}{1 + K_2 \times E_d^{1/S}} \left(\frac{dE}{dx}\right)_{\text{el}} \tag{4–6}$$

在上述方程中，我们假定屏蔽指数 S 与核反冲的路径的空间分布直接相关。如我们所知，核反冲的路径之所以在空间分布上更为分散，主要在于大量的次级核反冲。因此我们可以认为是次级的核反冲决定了核反冲路径的空间分布状态。于是我们用物理量原子核单位距离能量损失 $(dE/dx)_{\text{ncl}}$（即单位距离上反冲核损失给目标原子核的能量）来度量屏蔽指数 S。在本文中，我们假定 $S = K_3 \times (dE/dx)_{\text{ncl}}$。最终，我们把 Thomas-Imel 模型推广到核反冲事件：

$$\frac{Q}{Q_0} = \frac{N_i^{\text{esc}}}{N_i} = \frac{1}{\xi}\ln(1+\xi); \qquad \xi = \frac{K_1}{1 + K_2 \times E_d^{1/(K_3 \times (dE/dx)_{\text{ncl}})}} \left(\frac{dE}{dx}\right)_{\text{el}} \tag{4–7}$$

将实验数据带入上面的表达式，我们可以反向求解得到表达式中的未定参数 K_1, K_2 以及 K_3。我们会在下一章中继续对上述参数进行详细的讨论，并且将该模型的预测与实验数据进行对比。

第五章　低能核反冲在液氙探测器中的发光和电离效率

前面几章里面我们详细研究了反冲核在液氙探测器中的减速过程，电子单位距离能损 $(dE/dx)_{\mathrm{el}}$，以及自由电子和氙正离子的结合过程。结合这些物理分析，我们在这一章中可以进一步来计算反冲核在液氙探测器中的发光效率 $\mathcal{L}_{\mathrm{eff}}$ 和电离效率 $\mathcal{Q}_{\mathrm{y}}$。

在这一章里面，我们会说明怎样将核反冲在液氙探测器中的电子能损与自由电子和氙正离子的结合过程联系起来，而计算反冲核在液氙探测器中的发光效率 $\mathcal{L}_{\mathrm{eff}}$ 和电离效率 $\mathcal{Q}_{\mathrm{y}}$。并且，我们会给出我们的计算结果与实验数据的比较。最后，我们会回顾我们的工作，并给出未来如何才能进一步提高计算的精度。

5.1　液氙探测器中的相对发光效率

我们在第四章中的研究指出，并非所有的自由电子都可以在外加电场的作用下，漂移到云室而生成电离信号。而自由电子和氙正离子的结合，会使液氙探测器的发光效率得到相应提高。同时，如果被激发的氙原子密度过大，也有可能两个激发态的氙原子相互碰撞而减少激发原子的数量，这个效应又会使得发光效率被削弱。历史上对相关现象通常用 Birks 饱和定律来估算。当然，对于低能反冲核，我们在此不考虑这个效应。如果反冲核的初始动能很低，所产生的激发原子和自由电子的浓度相对都比较低，因此我们着重考虑自由电子脱离氙正离子而形成电离信号的过程。在这一节中，我们就用我们修正的 Thomas-Imel 模型来计算低能反冲核在液氙探测器中的发光效率 $\mathcal{L}_{\mathrm{eff}}$。

在这一节中，我们把自由电子逃离与氙正离子的效应作为发光效率不如预期大的主要原因，把这个效应标记为 q_{sc}。通常来说，这个效应在实验上可以通过测量液氙探测器产生的光子数和反冲核的电子单位距离能损 $(dE/dx)_{\mathrm{el}}$ 之间关系来考量。结合我们之前计算的反冲核在液氙探测器中的电子能损 $\eta(E\mathrm{nr})$，

我们可以知道，低能反冲核在液氙探测器中的发光效率可以表示为：

$$q(E_{\mathrm{nr}}) = \frac{\eta_{\mathrm{sc}}(E_{\mathrm{nr}})}{E_0} = \frac{\eta(E_{\mathrm{nr}})q_{\mathrm{sc}}(E_{\mathrm{nr}})}{E_{\mathrm{nr}}} \,. \tag{5–1}$$

显然，相类似的效应对于电子反冲事件也是存在的。因此当我们具体计算相对发光效率 $\mathcal{L}_{\mathrm{eff}}$ 的时候，对于电子反冲事件也要把这个效应考虑进来。

因为我们通常所说的相对发光效率 $\mathcal{L}_{\mathrm{eff}}$ 指的是在零电场情况下，因此在方程 Eq. (4–7) 中，自由参数 K_2 和 K_3 不会产生任何影响。如果我们假定自由参数 K_1 与电场大小无关，那么我们就可以首先确定自由参数 K_1。通常来说，我们可以通过实验观测的液氙探测器产生的光子数和反冲核的电子单位距离能损 $(dE/dx)_{\mathrm{el}}$ 之间关系，来反向求解 K_1。于是最终的发光损失 q_{sc} 可以通过下面的方程式来表示：

$$q_{\mathrm{sc}} = \frac{r + N_{ex}/N_i}{1 + N_{ex}/N_i} = \frac{1}{1 + N_{ex}/N_i}\left(1 - \frac{\ln(1 + K_1\frac{dE}{dx})}{K_1\frac{dE}{dx}} + \frac{N_{ex}}{N_i}\right) \tag{5–2}$$

表达式中，N_{ex}/N_i 和 K_1 都可以通过实验数据来反向拟合出来。

我们在上一章中曾经讨论过，比值关系 N_{ex}/N_i 一直存在争议。在本文中，我们更加倾向于使用实验观测的 $N_{ex}/N_i = 0.2$ 来做数据拟合。根据这个比率，我们可以得到 $K_1 = 2.53\ \ \mathrm{MeV}^{-1}\cdot\,\mathrm{g}\cdot\mathrm{cm}^{-2}$。同时为了避免争议，我们也试图通过其他的不同的 N_{ex}/N_i 比率来确定 K_1：$K_1 = 3.25\ \mathrm{MeV}^{-1}\cdot\mathrm{g}\cdot\mathrm{cm}^{-2}$ 与 $N_{ex}/N_i = 0.06$，$K_1 = 0.50\ \mathrm{MeV}^{-1}\cdot\mathrm{g}\cdot\mathrm{cm}^{-2}$ 与 $N_{ex}/N_i = 1.09$

使用这三套不同的参数，我们将所得到的发光效率与电子单位距离能损 $(dE/dx)_{\mathrm{el}}$ 之间的关系，绘制在图 5–1中。其中的阴影区域表示我们所关注的能量区域的电子单位距离能损 $(dE/dx)_{\mathrm{el}}$。从该图我们可以看出，不管我们使用什么参数，所得到的结果在我们所关注的能量区域几乎一致。因此，在下文中，我们将统一使用 $N_{ex}/N_i = 0.2$ 和 $K_1 = 2.53\ \mathrm{MeV}^{-1}\cdot\mathrm{g}\cdot\mathrm{cm}^{-2}$。

最终，我们可以来计算反冲核在液氙探测器中的相对发光效率 $\mathcal{L}_{\mathrm{eff}}$。

在这里我们需要强调一下我们所采用的 Lindhard 系数更加接近事实。下面我们花一点篇幅从原则来考察一下 Lindhard 系数与液氙的相对发光效率之间的关系。相对发光效率 $\mathcal{L}_{\mathrm{eff}}$ 理论上描述了在没有外加电场存在时候的液氙探测器中核反冲事件与电子反冲事件的发光效率的关系。由相对发光效率 $\mathcal{L}_{\mathrm{eff}}$ 的定义式，方程 Eq. (1–6)，我们可以进一步推出在没有外加电场存在时，其表达式可

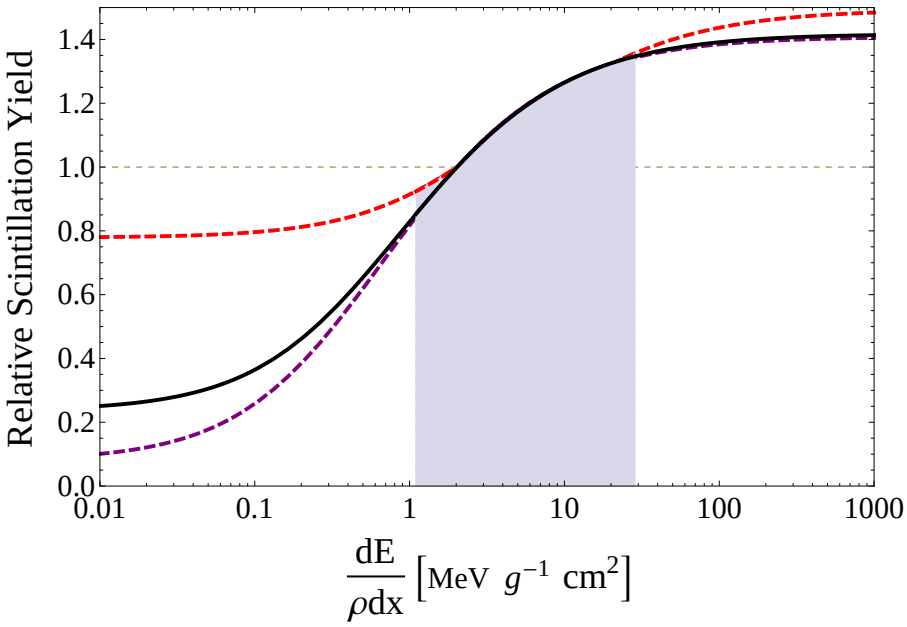

图 5–1 液氙的相对发光效率与 LET 的依赖关系

以化简为，

$$\mathcal{L}_{\text{eff}}(E_{\text{nr}}) = \frac{S1(E_{\text{nr}})}{E_{\text{nr}}} \frac{1}{L_y} \,. \tag{5–3}$$

同时，根据 Platzman 方程 Eq. (4–1)，我们知道反冲事件在液氙探测器中的电子能损大致可以产生三个效应：氙原子激发，氙原子电离出离子和电子对，以及热电子。我们假设比率为 r 的那部分离子和电子对会重新结合，于是我们可以得到发光信号的强度为，

$$S1 = k \times (N_{ex} + r \times N_i) \,, \tag{5–4}$$

在上述方程中，k 是一个与光电倍增管（PMT）相关的量，但是与反冲事件的类型无光。将上述方程 Eq. 5–4带入到相对发光效率的定义方程 Eq. 5–3中，我们可以得到 Lindhard 系数 q_{nc} 与相对发光效率 $\mathcal{L}_{\text{eff}}$ 之间的关系，

$$\mathcal{L}_{\text{eff}}(E_{\text{nr}}) = q_{\text{nc}}(E_{\text{nr}}) \times \frac{n_{ex} + r(E_{\text{nr}}) \times n_i}{n_{ex} + r(E_{\text{er}}) \times n_i} \,, \tag{5–5}$$

在方程中，我们令 $n_{ex} = N_{ex}/E^{ee}$ 并且 $n_i = N_i/E^{ee}$。

在我们的模型中，我们认为不管对于电子反冲事件还是核反冲事件，比率 N_{ex}/N_i 都是一致的。于是我们可以通过使用 Thomas-Imel model 来具体计算上式中分别对于电子反冲事件和核反冲事件的 r。根据我们的计算，核反冲事件的 r 要大于电子反冲事件的 r。这个结论也可以根据核反冲的电子单位距离能损大于电子反冲的电子单位距离能损而唯象的得出。最终我们可以断言，Lindhard 系数 q_{nc} 应该要比实验测量的液氙的发光效率 $\mathcal{L}_{\mathrm{eff}}$ 小。

另外，在文献 [45] 中，Hitachi 也曾经指出："The experimental neutron recoil studies show the scintillation efficiency ratio of recoil Xe ions to that for γ-rays, RC/γ. To compare the calculation with the measurements, one needs to account for the fact that the scintillation efficiency for γ-rays are less than 1." 既然相对发光效率 $\mathcal{L}_{\mathrm{eff}}$ 是核反冲事件相对于电子反冲事件的一个数值，而根据实验，我们知道核反冲时间的发光效率要大于电子反冲事件，我们同样可以得出 Lindhard 系数 q_{nc} 应该要比实验测量的液氙的发光效率 $\mathcal{L}_{\mathrm{eff}}$ 小。

综合上述计算和分析，根据我们的计算结果，液氙的相对发光效率 $\mathcal{L}_{\mathrm{eff}}$ 可以近似由下列表达式描述：

$$\mathcal{L}_{\mathrm{eff}}(E_{\mathrm{nr}}) = q_{\mathrm{nc}}(E_{\mathrm{nr}}) \times (1.417 - 0.245 \ln(1 + 4.822 E_{\mathrm{nr}}^{0.840}) E_{\mathrm{nr}}^{-0.840}) \cdot \quad (5\text{–}6)$$

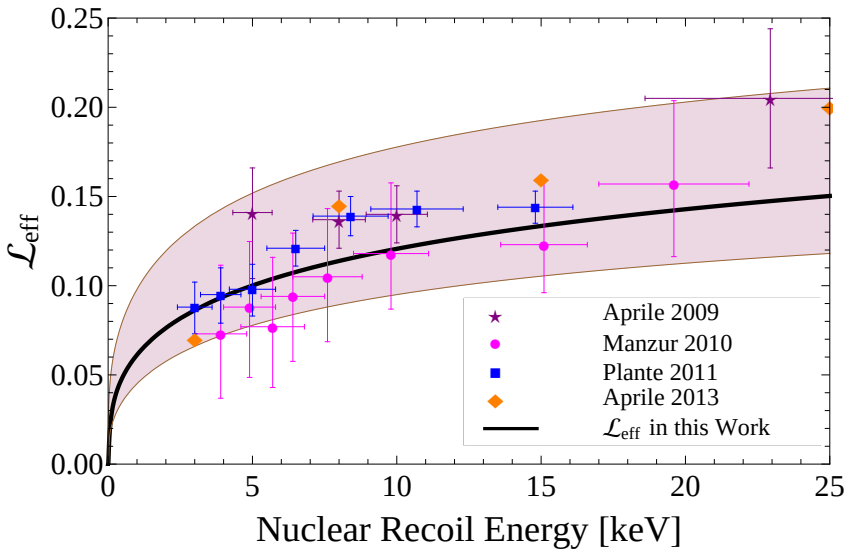

图 5–2 液氙的相对发光效率与实验数据的比较

我们将上述结果以及相关的实验数据同时绘制在图5–2中。其中的理论计算的 2σ 误差区域包括来自于电子单位距离能损 $(dE/dx)_{\rm el}$ 拟合的误差和来自于蒙特卡洛模拟过程中的统计误差。图中的是实验数据来与如下：蓝色正方形是来自于 Columbia 实验组的测量 [35]；品红色圆点是来自 Yale 实验组的测量 [15]；紫色的五角星来自于 XENON100 实验组的测量 [36, 43]。我们看到，我们的理论结果与实验测量数据符合很好。更重要的是，我们给出了在实验很难观测的区域的反冲核的发光效率的趋势。我们认为，极低能量的反冲核（能量低于 3 千电子伏特）在液氙探测器中的发光效率随着能量的降低，发光效率急剧下降，直到为零。

5.2　液氙探测器中的电离效率

5.2.1　产生一对自由电子和氙正离子的平均能量

相对反冲核在液氙探测器中的相对发光效率 $\mathcal{L}_{\rm eff}$，要想求解的电离效率 $\mathcal{Q}_{\rm y}$ 要相对复杂一些。即使我们已经知道了反冲核在液氙探测器中的电子能损 $\eta(E_{\rm nr})$，我们仍然要弄清楚产生一对自由电子和氙正离子所需要的平均能量，这个能量通常被称为 W-值。

因为上一章中提到的 Platzman 方程 Eq.(4–1) 仅仅对各个参数做了唯像的说明，所以我们没有办法直接从中获得 W-值。因此我们只能通过实验的方法来大致估计 W-值的大小。自上世纪 70 年代开始，若干个实验组对液氙介质中的 W-值做过实验观测 [70, 86–91]。科研人员曾经分别用过 α 源, γ-射线, X-射线以及单能的电子流来作为反冲源，进行观测。他们的观测结果可以通过表格 Table (5–1) 所展示。很显然，不同实验组所测量的 W-值五花八门，各不相同。这其中主要原因在于不同的实验对实验结果不同的解读。从放射源的角度来分析，具有较高电子单位距离能损 $(dE/dx)_{\rm el}$，同时本身能量较低的放生源是相对比较优良的产生电离电子的放射源。而低能电子流就符合这个条件。

下面我们对采用低能电子流作为放射源的实验，Takahashi 等人的实验 [70] 和 Seguinot 等人的实验 [91]，做进一步分析。在 1975 年，Takahashi 等人 [70] 使用能量大约在 1 兆电子伏特（MeV）的电子流测量的液氙中的 W-值，得出 $W = 15.6\pm0.3$ eV。他们的结果与液氙的带间能级差 9.3 电子伏特之间的关系是 $W = 1.68E_g$。而 1992 年，Seguinot 等人 [91] 通过加速电子到 100 千电子伏特（keV）左右作为放射源测量了液氙中的 W-值，给出

Radiation Source	W-value (eV)	Year	Reference
X-Ray	7.3	1973	Robinson and Freeman [86]
^{210}Po	17.3	1973	Kinno and Kobayashi [87]
^{63}Ni	16.5±1.4	1974	Takahashi *et al* [88]
^{207}Bi	15.6±0.3	1975	Takahashi *et al* [70]
X-Ray	15.2	1977	Huang and Freeman [89]
^{207}Bi	15.1±1.79	1991	Aprile *et al* [90]
Electron beams	9.76±0.70	1992	Seguinot *et al* [91]

表 5–1 不同实验测量的液氖中的 W-值

$W = 1.05E_g = 9.76\pm0.70$ eV。两者相差巨大，而 Seguinot 等人的结果也曾经引起一定争议 [92, 93]。但是 Seguinot 声称他们的结果对于低能电子流更加精确。

Takahashi 等人根据 Platzman 方程 Eq. (4–1) 对他们的结果做出了相应的理论解释：他们认为 $E_i = 1.13E_g$，同时给出理论计算值 $N_{ex}/N_i = 0.06$；然后通过 Shockley 模型计算得到 $\epsilon = 0.48E_g$。最终他们的理论解释结果为 $1.66E_g$，与他们的实验测量值 $1.68E_g$ 大致相符。而 Seguinot 等人并没有对他们的结果做出理论解释。但是如果忽略 Platzman 方程 Eq. (4–1) 中的热电子，同时假定 $E_i = E_g$ 并且 $N_{ex}/N_i = 0.06$，或者 $N_{ex}/N_i = 0.20$，我们可以得到在这种情况下的 W-值的理论预测在 $1.05E_g$ 和 $1.18E_g$ 之间，这与 Seguinot 等人的测量结果 $1.05E_g$ 相符合。

虽然 Takahashi 等人的测量结果被广为引用，我们觉得 Seguinot 等人的测量结果可能对于低能的电子反冲和核反冲更加精确。首先我们认为在 Platzman 方程 Eq. (4–1) 中的热电子的能量是来自于运动粒子，反冲电子或者反冲核，与自由电子的碰撞。当反冲电子或者反冲核的能量较低的时候，热电子从碰撞中所获得能量有限（$\sim m_{el}/m_{ncl}$）。因此，低能电子反冲事件或者核反冲事件中的电子能损应该只产生极其少量的热电子热量。另外，热电子本身也是实验上不可观测，而 E_g，E_{ex} 以及 N_{ex}/N_i 等值都可以通过独立实验来测量。因此我们在后续的讨论中会采用 Seguinot 等人的测量结果 $W = 1.05E_g = 9.76\pm0.70$ eV。

5.2.2　电离效率

当我们选定了 W-值之后，我们可以通过修正的 Thomas-Imel 方程来预测云室所能捕获的电子数量和外加电场，或者是反冲核能量之间的依赖关系，继而我们可以最终求得低能反冲核在液氙探测器中的电离效率 $\mathcal{Q}_{\mathrm{y}}$。

$$\mathcal{Q}_{\mathrm{y}}(E_{\mathrm{nr}}) = \frac{E_{\mathrm{nr}} q_{\mathrm{nc}}(E_{\mathrm{nr}})}{W} \times \frac{Q}{Q_0}(E_{\mathrm{nr}}) \times \frac{1}{E_{\mathrm{nr}}} = \frac{q_{\mathrm{nc}}(E_{\mathrm{nr}})}{W} \times \frac{Q}{Q_0}(E_{\mathrm{nr}})\,. \tag{5–7}$$

在我们计算低能反冲核在液氙探测器中的电离效率 $\mathcal{Q}_{\mathrm{y}}$ 之前，我们需要先确定方程 Eq. (4–7) 中的两个未定的自由参数 K_2 和 K_3。通过实验 [13] 中所测得的 56.5 千电子伏特（keV）的核反冲事件所产生的电子数目，我们可以拟合得出 K_2 和 K_3。在这里，我们采用的 W-值是 Seguinot 等人所测得的 9.76 电子伏特（eV），而核反冲的电子能损则是我们前文所计算得到的。这样，如果设定 E_d 的单位是 kV/cm，我们得到 $K_2 = 14.755$，同时 $K_3 = 0.004\ \mathrm{MeV}^{-1}\cdot\mathrm{g}\cdot\mathrm{cm}^{-2}$。我们把理论预言和实验结果同时绘制在图 5–3中。

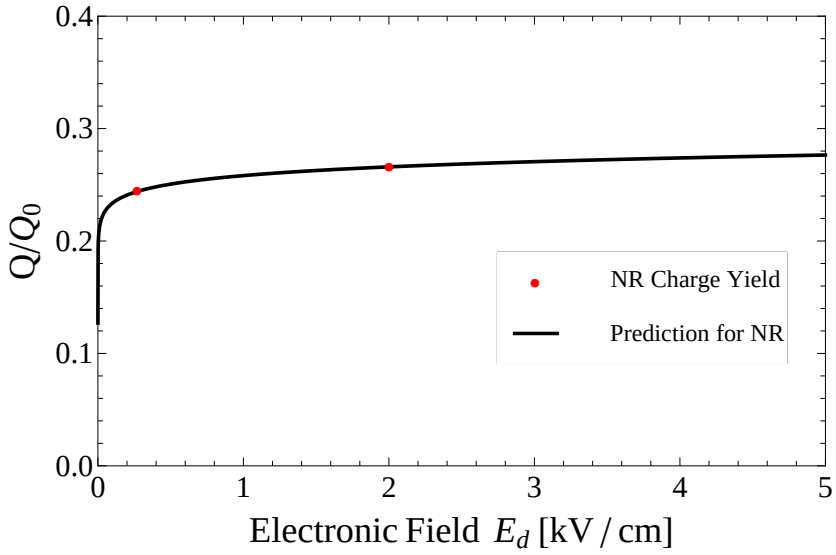

图 5–3 特定能量的核反冲事件的电离效率与电场的依赖关系

现在我们已经确定了方程 Eq. (4–7) 中的自由参数，现在我们可以来预测低能核反冲在液氙探测器中产生的电子比率与反冲核的初始能量之间的关系。我们对外加电场为 2 kV/cm 和 0.27 kV/cm 分别作了预测，并把结果绘制在图 5–4中。

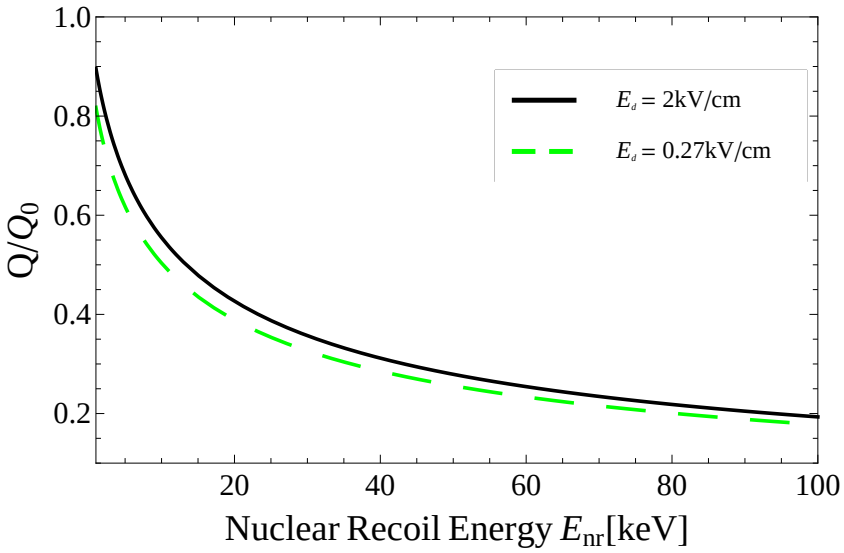

图 5–4 核反冲事件中产生的电子逃离与氙粒子结合的概率

结合上面所计算的核反冲的电子能损 $\eta(E_{\mathrm{nr}})$，W-值 [91]，以及修正的 Thomas-Imel 方程，我们最终可以通过方程 Eq. (5–7) 来计算低能核反冲在液氙探测器中产生的电子数与反冲核的初始能量之间的关系，即电离效率与初始能量之间的函数图。我们把预测结果用黑色实线绘制在图 5–5中。注意，因为核反冲的电离效率与外加电场关系不大，我们这里仅绘制了外加电场为 2 kV/cm 的结果。

同样，在图 5–5中，我们也把不同实验组的实验数据一起绘制进来。他们分别是：棕色三角形来自于 Yale 实验组的观测 [15]；蓝色正方形来自于 Columbia 实验组的观测 [13]；紫色圆形来自于 Case 实验组的观测 [13]；品红色菱形来自于 [14]；红色六角星来自于 XENON100 [43]。显然我们的预测与实验数据符合得很好。

在我们的结果当中，一个很重要的预言在于，低能反冲核在液氙探测器中的电离效率，随着初始能量的降低而升高，到了反冲核初始能量大约为 2 到 3 千电子伏特的时候达到一个最大值。这是因为随着反冲核动能的降低，其在液氙探测器中的电子能损逐渐降低，但是所产生电子的浓度也逐渐降低，于是更多的电子可以漂移到云室当中。正是由于这个性质，利用电离信号来重新构建反冲核的初始动能，可以大大降低液氙探测器的能量阈值。

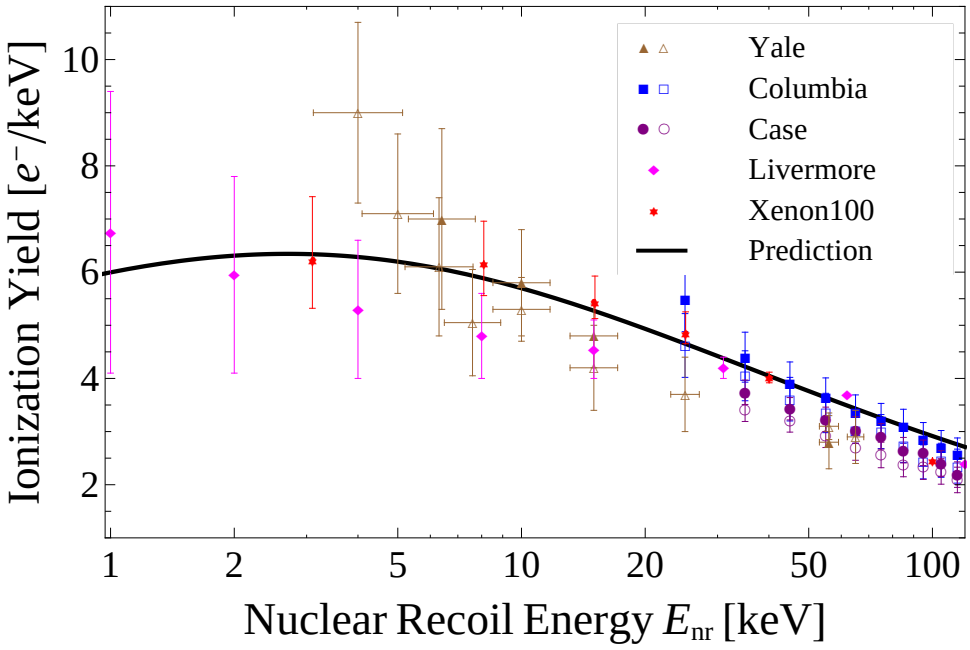

图 5–5 核反冲事件在液氙探测器中的电离效率

5.3　理论模型的进一步讨论

在本文中，我们对低能反冲核在液氙探测器中的发光效率和电离效率做了详尽的讨论和研究。这个研究更多的是出于为大质量弱相互作用粒子暗物质直接探测服务的目的。虽然我们的计算还远远谈不上是从头计算，或者第一性原理计算，但已经是目前最精确和详细的理论分析计算。我们的计算中，只引用了四个参数，包括氙原子之间的屏蔽库伦势，液氙中原子的空间分布，液氙的热运动能量以及电子单位距离能损。除了电子单位距离能损略有争议之外，其他三个参数近乎完美。

我们的模型所预言的结果与实验所观测的数据在很大程度上是符合的。我们对 $\mathcal{L}_{\rm eff}$ 和 $\mathcal{Q}_{\rm y}$ 的理论预测与中子散射实验的测量结果符合的很好。在无实验数据区域（低于 3 千电子伏特的区域），我们所预测的 $\mathcal{L}_{\rm eff}$ 迅速降低。该现象与之前的假设相矛盾。我们所预测的 $\mathcal{Q}_{\rm y}$ 随着原子反冲能量的降低而升高，在 2 到 3 千电子伏特的区域达到最大值。这个预测结果可以将探测器的探测极限进一步降低到大约 1 千电子伏特左右。由于电子信号相对易于探测，该预测有

可能被实验进一步证实或者证伪。

另外，我们也发现如果能对某些因素做更进一步的考虑，这个计算结果有可能更加精确。首当其冲的就是电子单位距离能损 $(dE/dx)_{\mathrm{el}}$。对于低能区的电子单位距离能损 $(dE/dx)_{\mathrm{el}}$，目前在理论和实验上都很难给出精确的数据。不同的理论模型给出的预言在低能区差异很大，而且与实验观测 [51] 的趋势并不相符合。比如说，实验中的结果发现，电子单位距离能损 $(dE/dx)_{\mathrm{el}}$ 更接近与反冲核的能量的 0.84 次方成比例 $E^{0.84}$ ，而非 $E^{0.5}$。在我们的程序中，我们采用了实验观测的结果。

我们工作当中另外一个误差来源在于我们程序中所使用的原子核二体碰撞近似。众所周知，低能的反冲核在液氩探测器中，很有可能同时与多个液氩原子发生作用。要更好的模拟这个过程，可能需要分子动力学相关的模拟。不过这个已经超出了我们本文的讨论范围。

对于核反冲在液氩探测器中电离效率，我们需要强调的是，因为模型中的自由参数是根据实验数据确定的，所以即使是使用不同的 Lindhard 系数，使用我们的模型都有可能得到与实验测量相符合的 Q/Q_0 比率。所以我们对 Thomas-Imel 方程的推广，更重要的是使其可以成功预测核反冲事件在液氩探测器中产生的可收集电子的数量趋势。

参考文献

[1] P. Salucci M. Persic and F. Stel. The universal rotation curve of spiral galaxies: 1. the dark matter connection. *Mon. Not. Roy. Astron. Soc.*, 281:27, 1996.

[2] A. Refregier. Weak gravitational lensing by large-scale structure. *Ann. Rev. Astron. Astrophys.*, 41:645–668, 2003.

[3] D. N. Spergel et al. Wilkinson microwave anisotropy probe (wmap) three year results: Implications for cosmology. *Astrophys. J. Suppl.*, 170:377, 2007.

[4] A. G. Riess et al. Observational evidence from supernovae for an accelerating universe and a cosmological constant. *The Astronomical Journal*, 116.3:1009, 1998.

[5] S. Perlmutter et al. Measurements of ω and λ from 42 high-redshift supernovae. *The Astrophysical Journal*, 517.2:565, 1999.

[6] D. Hooper G. Bertone and J. Silk. *Phys. Rep.*, 405:279, 2005.

[7] WMAP Collaboration. *Astrophys. J. Suppl. Ser.*, 192:14, 2011.

[8] H.C. Cheng et al. *Phys. Rev. Lett.*, 89:211301, 2002.

[9] A. Bottino et al. *Phys. Rev. D*, 69:037302, 2004.

[10] J. Ellis et al. *Phys. Rev. D*, 71:095007, 2005.

[11] D. Akimov. Techniques and results for the direct detection of dark matter. *Nucl. Instrum. Meth A*, 628:50–58, 2011.

[12] XENON100 Collaboration. Dark matter results from 225 live days of xenon100 data. *Phys. Rev. Lett.*, 109:181301, 2012.

[13] XENON100 Collaboration. Simultaneous measurement of ionization and scintillation from nuclear recoils in liquid xenon for a dark matter experiment. *Phys. Rev. Lett.*, 97:081302, 2006.

[14] P. Sorensen et al. *arXiv:1011.6439 [astro-ph.IM]*, .

[15] A. Manzur et al. Scintillation efficiency and ionization yield of liquid xenon for monoenergetic nuclear recoils down to 4 kev. *Phys. Rev. C*, 81:025808, 2010.

[16] D. Hooper G. Bertone and J. Silk. Particle dark matter: Evidence, candidates and constraints. *Physics Reports*, 405:279–390, 2005.

[17] F. Zwicky. Die rotverschiebung von extragalaktischen nebeln. *Helvetica Physica Acta*, 6:110–127, 1933.

[18] J. P. Ostriker et al. *Astrophys. J. Letters*, .

[19] J. Einasto et al. Dynamic evidence on massive coronas of galaxies. *Nature*, 250: 309–310, 1974.

[20] S. M. Faber and J. S. Gallagher. Masses and mass-to-light ratios of galaxies. *Ann. Rev. Astron. and Astrophys.*, 17:135–187, 1974.

[21] Y. Sofue and V. Rubin. Rotation curves of spiral galaxies. *Ann. Rev. Astron. and Astrophys.*, 39:137–174, 2001.

[22] M. Bartelmann and P. Schneider. Weak gravitational lensing. *Physics Reports*, 340:291–472, 2001.

[23] A. Gonzalez D. Clowe and M. Markevitch. Weak-lensing mass reconstruction of the interacting cluster 1e 0657-558 direct evidence for the existence of dark matter. *The Astrophysical Journal*, 604:596, 2004.

[24] J. R. Primack G. R. Blumenthal, S. M. Faber and M. J. Rees. Formation of galaxies and large-scale structure with cold dark matter. *Nature*, 311:517–52, 1984.

[25] R. Battesti et al. Axion searches in the past, at present, and in the near future. *Lecture Notes in Physics*, 741:199–237, 2008.

[26] M. Kamionkowskib G. Jungmana and K. Griestd. Supersymmetric dark matter. *Physics Report*, 267:195–373, 1996.

[27] M. W. Goodman and E. Witten. Detectability of certain dark-matter candidates. *Phys. Rev. D*, 31:3059–3063, 1996.

[28] J. D. Lewin and P. F. Smith. Review of mathematics, numerical factors, and corrections for dark matter experiments based on elastic nuclear recoil. *Astropar. Phys.*, 6:87, 1996.

[29] E. Aprile and T. Doke. Liquid xenon detectors for particle physics and astrophysics. *Rev. Mod. Phys.*, 82:2053–2097, 2010.

[30] A. I. Bolozdynya. Two-phase emission detectors and their applications. *Nucl. Instrum. Meth A*, 422:314–320, 1999.

[31] J. Kikuchi M. Yamashita, T. Doke and S. Suzuki. Double phase (liquid/gas) xenon scintillation detector for wimps direct search. *Astropart. Phys.*, 20:79–84, 2003.

[32] UKDMC Collaboration. Status of zeplin ii and zeplin iv study. *Nucl. Phys. B*, 124:229–232, 2003.

[33] XENON100 Collaboration. The xenon100 dark matter experiment. *Astropart. Phys.*, 35:573, 2012.

[34] X. Ji A. Tan H. Gong, K. L. Giboni and L. Zhao. The cryogenic system for the panda-x dark matter search experiment. *JINST*, 8:01002, 2013.

[35] XENON100 Collaboration. New measurement of the relative scintillation efficiency of xenon nuclear recoils below 10 kev. *Phys. Rev. C*, 79:045807, 2009.

[36] G. Plante et al. New measurement of the scintillation efficiency of low-energy nuclear recoils in liquid xenon. *Phys. Rev. C*, 84:045805, 2011.

[37] DAMA Collaboration. First results from dama/libra and the combined results with dama/nai. *Eur. Phys. J. C*, 56:333, 2008.

[38] CoGeNT Collaboration. Results from a search for light-mass dark matter with a p-type point contact germanium detector. *Phys. Rev. Lett.*, 106:131301, 2011.

[39] CDMS Collaboration. *arXiv:1304.4279[hep-ex]*, .

[40] J. I. Collar and D. N. McKinsey. *arXiv:1005.0838 [astro-ph.CO]*.

[41] V. N. Lebedenko et al. Result from the first science run of the zeplin-iii dark matter search experiment. *Phys. Rev. D*, 80:052010, 2009.

[42] P. Sorensen et al. The scintillation and ionization yield of liquid xenon for nuclear recoils. *Nucl. Instrum. Meth. A*, 601:339, 2009.

[43] XENON100 Collaboration. *arXiv:1304.1427*, .

[44] J. Lindhard et al. Integral equations governing radiation effects.(notes on atomic collisions, iii). *Kgl. Danske Videnskab., Selskab. Mat. Fys. Medd.*, 33:10, 1963.

[45] A. Hitachi. Properties of liquid xenon scintillation for dark matter searches. *Astropart. Phys.*, 24:247, 2005.

[46] D. M. Mei et al. A model of nuclear recoil scintillation efficiency in noble liquids. *Astropart. Phys.*, 30:12, 2008.

[47] F. Bezrukov et al. Interplay between scintillation and ionization in liquid xenon dark matter searches. *Astropart. Phys.*, 35:119, 2011.

[48] J. F. Ziegler et al. Srim - the stopping and range of ions in matter (2010). *Nucl. Instrum. Meth. B*, 268:1818, 2010.

[49] S. Agostinelliae et al. Geant4-a simulation toolkit. *Nucl. Instrum. and Meth. A*, 506:250, 2003.

[50] G. F. Knoll. *Radiation detection and measurement*. Wiley. com, 2010.

[51] A. Fukuda. Srim - the stopping and range of ions in matter (2010). *J. Phys. B: At. Mol. Opt. Phys*, 14:4533, 1981.

[52] L. D. Landau and E. M. Lifshitz. *Mechanics*. Butterworth-Heinemann Ltd Press, Oxford, U.K., 1976.

[53] K. Wamba. *Ph.D thesis, Stanford University*.

[54] J. Eichler. *Lectures on ion-atom collisions: From nonrelativistic to relativistic velocities*. Elsevier Science, 2005.

[55] D. J. Ficenec et al. Observation of electronic excitation by extremely slow protons with applications to the detection of supermassive charged particles. *Phys. Rev. D.*, 36:311, 1987.

[56] J. D. Jackson. *Classical Electrodynamics (3rd Edition)*. John Wiley Sons Inc., 1999.

[57] N. Bohr. *Philos. Mag.*, page 10.

[58] P. Sigmund and A. Schinner. Binary theory of electronic stopping. *Nucl. Instrum. Meth. B*, 195:64, 2002.

[59] W. Brandt and M. Kitagawa. Effective stopping-power charges of swift ions in condensed matter. *Phys. Rev. B*, 25:5631, 1982.

[60] P. M. Echenique et al. Nonlinear stopping power of an electron gas for slow ions. *Phys. Rev. A*, 33:897, 1986.

[61] J. Lindhard et al. On the properties of a gas of charged particles. *Kgl. Danske Videnskab., Selskab. Mat. Fys. Medd.*, 28:8, 1954.

[62] J. Lindhard and M. Scharff. Energy dissipation by ions in the kev region. *Phys. Rev.*, 124:128, 1961.

[63] I. S. Tilinin. Quasiclassical expression for inelastic energy losses in atomic particle collisions below the bohr velocity. *Phys. Rev. A*, 51:3058, 1995.

[64] N. R. Arista. Energy loss of ions in solids: Non-linear calculations for slow and swift ions. *Nucl. Instr. and Meth. B*, 195:91–105, 2002.

[65] H. Geissel Y. Laichter and N. H. Shafrir. On the nuclear charge and atomic mass of attenuated mean fission fragments. *Nucl. Instrum. Meth.*, 194:45–50, 1982.

[66] P. Bauer et al. Phase effect in the energy loss of h projectiles in zn targets: Experimental evidence and theoretical explanation. *Phys. Rev. Lett.*, 69:1137, 1992.

[67] A. Arnau et al. Phase effect in the energy loss of hydrogen projectiles in zinc targets. *Phys. Rev. B*, 49:6470, 1994.

[68] M. Bergsmann et al. Phase effect in stopping of h ions in mg. *Phys. Rev. B*, 62: 3153, 2000.

[69] R. L. Platzman. Total ionization in gases by high-energy particles: An appraisal of our understanding. *Int. J. Appl. Radiat. Is.*, 10:116, 1961.

[70] T. Takahashi et al. Average energy expended per ion pair in liquid xenon. *Phys. Rev. A*, 12:1771, 1975.

[71] T. Doke et al. Absolute scintillation yields in liquid argon and xenon for various particles. *Jpn. J. Appl. Phys.*, 41:1538, 2002.

[72] E. Aprile et al. Search for light dark matter in xenon10 data. *Phys. Rev. Lett.*, 107:051301, 2011.

[73] E. Aprile et al. Observation of anti-correlation between scintillation and ionization for mev gamma-rays in liquid xenon. *Phys. Rev. B*, 76:014115, 2007.

[74] P. Sorensen. A coherent understanding of low-energy nuclear recoils in liquid xenon. *J. Cosmol. Astropart.*, 09:033, 2010.

[75] P. Langevin. Recombinaison et mobilites des ions dans les gaz. *Ann. Chim. Phys.*, 28:433, 2007.

[76] L. Onsager. Initial recombination of ions. *Phys. Rev.*, 54:554, 1938.

[77] G. Jaffe. On the theory of recombination. *Phys. Rev.*, 58:968, 1940.

[78] H. A. Kramers. On a modification of jaffe's theory of column-ionization. *Physica.*, 18:665, 1952.

[79] J. Thomas and D. A. Imel. Recombination of electron-ion pairs in liquid argon and liquid xenon. *Phys. Rev. A*, 36:614, 1987.

[80] A. Mozumder. Free-ion yield and electron-ion recombination rate in liquid xenon. *Chem. Phys. L*, 245:359, 1995.

[81] S. P. Chabod. Charge collection efficiency in ionization chambers operating in the recombination and saturation regimes. *Nucl. Instr. and Meth. A*, 604:632, 2009.

[82] S. Howe L. S. Miller and W. E. Spear. Charge transport in solid and liquid ar, kr, and xe. *Phys. Rev.*, 166:871, 1968.

[83] T. Doke et al. Let dependence of scintillation yields in liquid argon. *Nucl. Instr. and Meth. A*, 269:291, 1988.

[84] V. Chepel and A. Henrique. Liquid noble gas detectors for low energy particle physics. *J. of Instr.*, 8:04001, 2013.

[85] C. E. Dahl. *Ph.D. thesis, Princeton University*.

[86] M. G. Robinson and G. R. Freeman. X-radiolysis ion yields and electron ranges in liquid xenon, krypton, and argon: Effect of electric field strength. *Can. J. Chem.*, 51:641–649, 1973.

[87] S. Konno and S. Kobayashi. The w-value in liquid xenon is found to be 17.3 ev. *Sci. Pap. Inst. Phys. Chem. Res. (Jap.) V.*, 67:57–62, 1973.

[88] T. Takahashi et al. The average energies, w, required to form an ion pair in liquefied rare gases. *J. Phys. C*, 7:230, 1974.

[89] Sam S-S. Huang and G. R. Freeman. Effect of density on the total ionization yields in x-irradiated argon, krypton, and xenon. *Can. J. Chem.*, 55:1838–1846, 1977.

[90] E. Aprile et al. Performance of a liquid xenon ionization chamber irradiated with electrons and gamma-rays. *Nucl. Instr. and Meth. A*, 302:177–185, 1991.

[91] J. Seguinot et al. Liquid xenon ionization and scintillation studies for a totally active-vector electromagnetic calorimeter. *Nucl. Instr. and Meth. A*, 323:583–600, 1992.

[92] M. Miyajima et al. Comments on liquid xenon ionization and scintillation studies for a totally active-vector electromagnetic calorimeter. *Nucl. Instr. and Meth. A*, 352:548–551, 1995.

[93] J. Seguinot et al. Reply to comments on liquid xenon ionization and scintillation studies for a totally active-vector electromagnetic calorimeter. *Nucl. Instr. and Meth. A*, 361:623–624, 1995.

致 谢

首先我想感谢我的指导老师，季向东教授。没有他，我不可能如此顺利的进入学术界这个对于我来说全新的一个领域。不管在理论物理，还是在实验物理方面，他惊人的洞察力都帮助我进一步理解什么是物理，怎样做正确的科学研究。

对于我生命中最重要的朋友，杨乘程博士，我想说：若不是你，我根本不可能进入到学术领域；是你激励我在这样一个全新的领域里挺过来。同时我要感谢我的两个好朋友，王士铖和郑勇。他们在我读书期间给予我足够的支持，是我免于后顾之忧。

我非常感谢王宇杰博士对我的帮助。如果不是他犀利的语言，我无法了解到我自己的缺点和短处。当我刚刚进入这个领域的时候，我对这个领域的困难完全估计不足，是他帮助我了解到我应该做什么，怎样做，以及怎样设定我对自己的预期。这些都是我自己很难领悟到的。

我的合作者，熊小努，也给予了我很大的帮助。我们两个是完全不同的两种人。我更加感性，有时候会脱离实际，而小努非常理性，他总能在我想飞的时候把我带回这个实际的世界。另外，也是他帮助我明白怎样利用正确的数学工具，通过理论计算来实现我的想法。

同时我要感谢我在微软的很多同事，包括 Freeman Xu，Steven Xu，Densery Wang，Evonne Zhang，Jennifer Luo，Miles Li，Wei Zhao 以及 Tina Yao 等等。虽然 Tony Wang 已经离开微软加入了 Dell，我永远也不会忘记，当听到我考取了交通大学研究生的时候，他宴请我以及各位同事来庆祝。还有其他的一些朋友，比如说祝婉怡，刘心悦，李雪，居娴静等等，他们在我感觉到泄气或者沮丧的时候给予我足够的鼓励和帮助。非常感谢！

感谢还要送给我的同学们，他们年轻充满朝气，让我重新体验到校园生活：高飞，马尧，张永超，郭刚，龚昊伟，赵勇，鲁文斌，Leighton Arnold，邓黎杰，李洋，张科，张沈莉，张晓丹 …等等一众同学。

最后，当然最终要的，我要感谢我的父母。他们一直给予我关心和爱护。不管我想做什么，他们总是支持我，鼓励我。我爱他们。

I would like to first thank my advisor, Jı Xiangdong, without whom I could not start my academia career so smoothly. His insight in both theoretical and experimental physics does help me to know what is physics and how to do research in the right way. I would also thank him for supporting me in every aspect during my years at Shanghai Jiao Tong University.

To the nearest friend in my life, Dr. Helen Young, I would like to say, without you I would not join in academia at all. It is you who motivate me to survive in physics research. I also want to thank my best friends, Shicheng Wang and Yong Zheng, both of them give me enough support during the period I pursue my master diploma.

I am very grateful to Dr. Yujie Wang and I am so thankful for his "encouragement" every time when I talk with him. I'm a little crazy when I became a student in physics. Dr. Wang helps me to understand the difficulties I may encounter in this new field and encourage me doing the right thing.

My peer, Xiaonu Xiong, also gives me lots of help. We are totally different kind of persons. I'm ideal and sometimes impractical while he is rational and always draws me back to the real world. And it is he who helps me to understand how to calculate and how to realize my idea using right mathematic methods.

My thanks also go to Freeman Xu, Steven Xu and other colleagues, such as Densery Wang, Evonne Zhang, Jennifer Luo, Miles Li, Wei Zhao and Tina Yao etc., in Microsoft. Although Tony Wang has left Microsoft and joined Dell, I will never forget that he treated us to celebrate my success in the National Postgraduate Entrance Examination. Other friends, such as Wanyi Zhu, Xinyue Liu, Xue Li, Xianjing Ju, also give much support when I'm frustrated and depressed. I really appreciate it.

I feel so lucky to work with a group of young and active mates, Fei Gao, Yao Ma, Yongchao Zhang, Gang Guo, Haowei Gong, Yong Zhao, Robinson Lu, Leighton Arnold, Lijie Deng, Yang Li, Ke Zhang, Shenli Zhang, Xiaodan Zhang ···it is really a long list.

Finally, I want to thank my parents, who have always offered love, support and encouragement whatever I decided to do. They set me in a free environment to pursue a career that I think is right and worth to do. I love them.

Shanghai Jiao Tong University

Scintillation Efficiency and Ionization Yield of Low Energy Nuclear Recoils in Liquid-Xenon Dark Matter Detection

Author

Wei Mu

Advisor

Professor Dr. Xiangdong Ji

A thesis submitted in fulfillment of the requirements
for the degree of Master of Physics

in the

PandaX Dark Matter Experiment Group
Department of Physics and Astronomy

November 2014

Declaration of Authorship

I, Wei Mu, declare that this thesis titled, 'Scintillation Efficiency and Ionization Yield of Low Energy Nuclear Recoils in Liquid-Xenon Dark Matter Detection' and the work presented in it are my own. I confirm that:

- This work was done wholly or mainly while in candidature for a research degree at this University.
- Where any part of this thesis has previously been submitted for a degree or any other qualification at this University or any other institution, this has been clearly stated.
- Where I have consulted the published work of others, this is always clearly attributed.
- Where I have quoted from the work of others, the source is always given. With the exception of such quotations, this thesis is entirely my own work.
- I have acknowledged all main sources of help.
- Where the thesis is based on work done by myself jointly with others, I have made clear exactly what was done by others and what I have contributed myself.

Signed:

Date:

Abstract

Scintillation Efficiency and Ionization Yield of Low Energy Nuclear Recoils in Liquid-Xenon Dark Matter Detection

by Wei Mu

Liquid xenon (LXe) detectors, among many direct detection experiments which have been proposed and run in the last two decades, have shown particular promising in the detection of weakly interacting massive particles (WIMPs), an attractive candidate for Dark Matter (DM), by observing the atomic recoils after WIMPs' elastic scattering on nuclei. The elastic scattering will produce a recoiling xenon atom, also called nuclear recoil, with kinetic energy up to a few tens of keV. It excites and ionizes xenon atoms, giving rise to scintillation signals S1 through the de-excitation of excitons and recombination of electron-ion pairs, and ionization signals S2 through the electrons escaping from recombination, respectively.

Two crucial properties of LXe detectors are the so-called relative scintillation efficiency $\mathcal{L}_{\text{eff}}$ and ionization yield $\mathcal{Q}_{\text{y}}$, which serve as bridges between the detected S1 and S2 signals and the deposited energy of the WIMPs in LXe detector. $\mathcal{L}_{\text{eff}}$ or $\mathcal{Q}_{\text{y}}$, together with the detected S1 or S2 signals, is used to reconstruct and calibrate the initial nuclear recoils energy, hence study the properties of the WIMPs. The biggest challenge for experiments to measure $\mathcal{L}_{\text{eff}}$ and $\mathcal{Q}_{\text{y}}$ lies in very low energy nuclear recoils, particularly at the detection threshold, where most of the recoiling events will be if the mass of WIMPs is around several GeV/c^2. In this thesis,the LXe scintillation and ionization process are analyzed in details and a state-of-the-art theoretical analysis of the $\mathcal{L}_{\text{eff}}$ and $\mathcal{Q}_{\text{y}}$ in the very low energy region has been performed.

Based on Lindhard's basic integral equation and the binary collision approximation, a computer program, which reflects our understanding on the slowing down process of the recoiling nucleus in liquid xenon, is developed to calculate how much nuclear recoil energy is dissipated to electrons in the medium, hence produces scintillation and ionization signals at last, which is the so-called nuclear quenching factor q_{nc} or Lindhard factor. To obtain an accurate nuclear quenching factor at low energy region, existing theoretical models and experimental data for electronic energy dissipation: electronic stopping power S_e, are reviewed and analyzed. We improve transport cross section method and re-calculate the electronic stopping

power at low energy region. The theoretical prediction for S_e in liquid xenon agrees with the experimental data very well. To evaluate the electron-ion pair recombination rate, the different behaviors for the electron-ion pair recombination process regarding electron recoils, alpha recoils, and nuclear recoils, are studied and the Thomas-Imel box model is generalized to describe the recombination behaviors regarding nuclear recoils. At last the recombination rate can be expressed as a function of nuclear recoil energy and the applied electric field.

Combining the electronic energy dissipation from the computer simulation and the generalized Thomas-Imel box model, we predict the $\mathcal{L}_{\text{eff}}$ and $\mathcal{Q}_{\text{y}}$ at low energy region. The predictions from this work agree well with the measured $\mathcal{L}_{\text{eff}}$ and $\mathcal{Q}_{\text{y}}$ from the neutron scattering experiments. The predicted $\mathcal{L}_{\text{eff}}$ suggests a rapid drop when the recoiling energy comes below 3 keV where authors have pointed out the liquid xenon scintillation response should drop steadily at low energy. The predicted $\mathcal{Q}_{\text{y}}$ increases with the decreasing of the recoiling energy and reaches the maximum value at 2$\sim$3 keV, which may be examined by experiment in the future and lower the energy threshold for nuclear recoils to $\sim$1 keV.

Acknowledgements

I would like to first thank my advisor, Professor Dr. Xiangdong Ji, without whom I could not start my academia career so smoothly. His insight in both theoretical and experimental physics does help me to know what is physics and how to do research in the right way. I would also thank him for supporting me in every aspect during my years at Shanghai Jiao Tong University.

To the nearest friend in my life, Dr. Helen Young, I would like to say, without you I would not join in academia at all. It is you who motivate me to survive in physics research. I also want to thank my best friends, Shicheng Wang and Yong Zheng, both of them give me enough support during the period I pursue my master diploma.

I am very grateful to Dr. Yujie Wang and I am so thankful for his "encouragement" every time when I talk with him. I'm a little crazy when I became a student in physics. Dr. Wang helps me to understand the difficulties I may encounter in this new field and encourage me doing the right thing.

My peer, Xiaonu Xiong, also gives me lots of help. We are totally different kind of persons. I'm ideal and sometimes impractical while he is rational and always draws me back to the real world. And it is he who helps me to understand how to calculate and how to realize my idea using right mathematic methods.

My thanks also go to Freeman Xu, Steven Xu and other colleagues, such as Densery Wang, Evonne Zhang, Jennifer Luo, Miles Li, Wei Zhao and Tina Yao etc., in Microsoft. Although Tony Wang has left Microsoft and joined Dell, I will never forget that he treated us to celebrate my success in the National Postgraduate Entrance Examination. Other friends, such as Wanyi Zhu, Xinyue Liu, Xue Li, Xianjing Ju, also give much support when I'm frustrated and depressed. I really appreciate it.

I feel so lucky to work with a group of young and active mates, Fei Gao, Yao Ma, Yongchao Zhang, Gang Guo, Haowei Gong, Yong Zhao, Robinson Lu, Leighton Arnold, Lijie Deng, Yang Li, Ke Zhang, Shenli Zhang, Xiaodan Zhang ... it is really a long list.

Finally, I want to thank my parents, who have always offered love, support and encouragement whatever I decided to do. They set me in a free environment to pursue a career that I think is right and worth to do. I love them.

To My Father

Contents

List of Figures

List of Tables

Chapter 1

Dark Matter and Liquid Xenon Direct Detection of WIMP Dark Matter Particles

Even long before Sir Isaac Newton published his classic work "Philosophiae Naturalis Principia Mathematica", a great deal of efforts have been made towards explaining the profound mystery of the universe. As the advancements of theory and technology in the past century, physicists are able to explore the most micro and macro worlds, the particle physics and astro physics. Similar to the development in elementary particle, where theoretical and experimental efforts have yielded a Standard Model of particle physics, the experimental measurements of galactic rotation curves, the gravitational lensing, the cosmic microwave background (CMB), Large Scale Structure (LSS) and type Ia supernovae observations [5–9] together with the theoretical predictions from general relativity give rise to a standard model of cosmology. All the evidences from the standard model of cosmology indicate that a large number of components existing in the universe is invisible. Combining the theoretical predictions and the experimental measurements, it is expected that the universe consists of about 72% dark energy, about 23% non-baryonic dark matter which reflect the invisible mass, and about 4.6% baryons which constitute the ordinary matter.

Shortly after Zwicky proposed the dark matter hyperthesis to explain his measurements for the velocity dispersion of objects at the edge of the Coma cluster in 1933 [10], the nature and property of dark matter became one of the most intriguing fundamental problems in

modern physics. A great many physicists put large efforts in finding out the reasonable dark matter candidates from beyond the standard model, among which weakly interacting massive particle (WIMP) seems to be a well-motivated class of dark matter candidate. WIMP can be predicted by several models of physics beyond the Standard Model naturally [11–13]. For an instance, in supersymmetric (SUSY) model, the lightest particles satisfy most of the features of WIMPs [14, 15]. In theory, WIMPs are a kind of particles who are electrically neutral with masses ranging from GeV/c^2 to TeV/c^2 and interact with ordinary matters via the weak interaction like neutrinos. WIMPs can be directly detected by observing the signals from atomic recoils after their elastic scattering on nuclei in a detector.

In the last two decades, many direct detection experiments have been proposed and run [16], among which liquid xenon (LXe) detectors have shown particular promising. The recent XENON100 and LUX experiments have yielded the best detection limits in almost all regions of the possible WIMP masses, more sensitive than most other experiments using alternative detection media [17]. A list of xenon experiments, XMASS, PandaX, and XENON1T will soon join the direct search efforts. Most advanced LXe detectors [2, 18, 19] work in the two-phase mode with measurements of both scintillation (or direct scintillation light, denoted as S1) and ionization (proportional scintillation light, denoted as S2) signals at the same time. The scintillation and ionization signals, together with the relative scintillation efficiency ($\mathcal{L}_{\rm eff}$) and the ionization yield ($\mathcal{Q}_{\rm y}$) respectively, have been used to reconstruct and calibrate the nuclear recoil energy. Thus $\mathcal{L}_{\rm eff}$ and $\mathcal{Q}_{\rm y}$ are two crucial physical quantities for the energy calibration of WIMPs direct detection.

In this Chapter, we first review the evidences from cosmographic observations for non-relativistic, non-baryonic dark matter, and describe why WIMPs naturally become one of the most attractive candidates for dark matter. After that, we show the dark matter direct detection method, the basic implementation of xenon detectors and the crucial physical quantities for the LXe detector. In Chapter 2, we describe the slowing down process of the nuclear recoils in the detector and show how we calculate the electronic energy dissipation of the nuclear recoils. In Chapter 3, we review the theoretical researches and experimental measurements on the electronic stopping power in liquid xenon. At last, it shows how we determine the value for electronic stopping power for liquid xenon at low energy region and the result of electronic energy dissipation of nuclear recoils. In Chapter 4, we discuss scintillation and ionization process of two-phase xenon time projection chambers and describes how to evaluate the electron-ion pairs' recombination using a thoeretical model. At last, Chapter 5

gives out our calculation results on $\mathcal{L}_{\text{eff}}$ and $\mathcal{Q}_{\text{y}}$ and shows the potential improvement of the calculations and theoretical consideration.

1.1 Evidence for Dark Matter and Candidates

1.1.1 Missing Mass in the Universe and Dark Matter Hyperthesis

Starting from Newton's law of gravity, one can easily calculate the rotational velocity of the spherically symmetric matter at radius r, which follows the equation below:

$$v(r) = \sqrt{\frac{GM(r)}{r}} \tag{1.1}$$

where $M(r) = 4\pi \int \rho(r) r^2 dr$ and $\rho(r)$ is the mass density profile. However, Eq. (1.1) seems not to be that right for galaxy rotational curves, where the observed mass cannot support that high rotational velocity of the matter. A large number of cosmological observations show a large amount of missing mass in the universe, particularly in the Milky Way [20].

In 1933, when Zwicky studied the velocity dispersion in galaxy clusters [10], he noticed that the flat rotational curve at large radius indicates a relation where $M(r) \propto r$, which means that more than 10 times the mass than that in the luminous galaxies themselves is required to keep Eq. (1.1) balance. This result suggests an extended invisible halo, with $\rho(r) \propto 1/r^2$, beyond the optical disk exists in the Milky Way. Following Zwicky's work, more and more cosmological observations on the relation between the galaxy mass and the radius indicate the galaxy mass increases almost linearly with the radius up to 100 kpc and 1012 $M_{\odot}$ for spiral and elliptical galaxies [21, 22]. All of the observations suggest that the matters we are observing are only a small part of the total matters in those galaxies. In 1979, Faber and Gallagher reviewed the cosmological observations and studied the mass to light ratio for various types galaxies in Ref. [23]. In the review articles, they summarized the convincing evidences for the existence of those invisible mass in the galaxies. Nowadays, it becomes an accepted concept that the flat rotation curves of spiral galaxies, from the galaxy center out to large distance, refers to the combination of the gas, the galaxy disk and an extended invisible halo where the dark matter may lie [24]. The concept of dark matter gives a reasonable explanation of why the observed velocity distributions at large radii of galaxies does not satisfy Eq. (1.1).

Certainly, only the gravitational effect of the galaxy rotational curves cannot bring so much interest from physicists to dark matter. Dark matter also acts as a key factor to explain many kinds of cosmological effects, such as the cosmological constraints on the mass density Ω_m in the universe. Friedmann once proposed the equations to express a universe consisted of non-relativistic matter and a cosmological constant as below:

$$\frac{H^2}{H_0^2} \equiv \frac{1}{H_0^2}\left(\frac{\dot{a}}{a}\right)^2 = \Omega_m \left(\frac{a_0}{a}\right)^3 + \Omega_k \left(\frac{a_0}{a}\right)^2 + \Omega_\Lambda \ , \tag{1.2}$$

$$\frac{1}{H_0^2}\frac{\ddot{a}}{a} = -\frac{1}{2}\Omega_m \left(\frac{a_0}{a}\right)^3 + \Omega_\Lambda \ , \tag{1.3}$$

where Ω_m and Ω_Λ are the energy densities of the matter and the cosmological constant relative to the critical density $\frac{3H_0^2}{8\pi G}$, H_0 is the Hubble constant nowadays (70.8 km/s/Mpc), H and a are the Hubble constant and scale factor at time t, and Ω_k is a term for the spatial curvature of the universe. The relative densities are constructed such that $\Omega_m + \Omega_k + \Omega_\Lambda = 1$ which can be evaluated by Eq. (1.2) at today. As the development of instruments and telescopes, the Friedmann equations can be examined accurately by cosmological observation today when the acceleration of the universes expansion and the anisotropies in the cosmic microwave background (CMB) can be measured much more precise than before. According to recent observations on type Ia supernovae, the galaxy cluster and the CMB, the total energy density Ω_Λ is around 0.7 and mass density Ω_m in the university is around 0.3, which is shown in Fig. 1.1.

Using the weak gravitational lensing observations, one can measure the matter density much better, which also becomes one of the evidences of dark matter's existence. Through a weak gravitational lensing, the path of light from a distant galaxy distorts, because the light gets a deformation in the gravitational field of the background galaxies behind a cluster in question. Different from strong lensing, where a specific object is identified as being lensed and producing multiple images or gross distortion, the distortions from weak lensing are smaller. Studying the patterns of distortion in large numbers of lensed objects, one can obtain the amount of mass in that gravitational lens exactly. Ref. [25] gives a review on the behavior of weak gravitational lensing. Clowe *et al* presented a weak-lensing mass reconstruction of the interacting cluster 1E 0657-558 in Ref. [26], which can be regarded as a direct evidence of the existence of dark matter.

Another evidence for dark matter is from the cosmic structure formation at large scale. The

cosmic structure grows when over dense regions draw in surrounding matter. It creates a positive feedback for fluctuations of matter density in the early universe and is also a clue to the property of dark matter. The gravitational instability and small fluctuations of the initial density field of the universe cause the formation of large scale structure and the galaxy distribution in current universe. Thus the measurement of the distribution of galaxy clustering at large scales can be used to determine the mass density of universe. Experiments such as the Sloan Digital Sky Survey have revealed the extent of large scale structure in the universe to extend even beyond the super cluster size. From the observed large scale structure formation evolution, one can re-construct the initial mass density profile of the early universe, where dark matter, especially non-relativistic dark matter [27], is required.

1.1.2 Dark Matter and WIMPs

As mentioned in the previous section, a large number of evidences from the cosmological observations all give us the basic idea about the universe: 4.6% baryons, 23% dark components with mass (dark matter), and 72% vacuum energy (or so-called dark energy). The existence of dark matter becomes obvious. However, the nature and properties of the dark matter particles are still unknown and unclear. Evidently, to explore and predict the invisible component of the universe may always produce new physics and introduce new particles. Among all the theoretical candidates for the dark matter particles, there are two particles are promising: axions and weakly interacting massive particles, or WIMPs. In this thesis, we will focus on WIMPs while the details about axions can be found in Ref. [28].

Following the assumption that the dark matter is a thermal relic of the big bang [29], the WIMP hypothesis can be derived naturally. Consider a kind of particle χ whose mass is M_χ and annihilation cross section is σ_a. In the early universe, when the temperature $T \gg M_\chi$, these particles will have the same abundance as any other light particles in thermal equilibrium. After the universe cools to the temperature $T < M_\chi$, the equilibrium number of particles n_χ^{eq} falls. The number density should satisfy the equation:

$$\frac{dn_\chi}{dt} = -\langle\sigma_a v\rangle[(n_\chi)^2 - (n_\chi^{eq})^2] - 3Hn_\chi \ , \tag{1.4}$$

where $\langle\sigma_a v\rangle$ is the thermally averaged velocity times annihilation cross section. The first term on the right hand side of Eq. (1.4) shows that n_χ approaches n_χ^{eq} at a rate determined

by the annihilation cross-section times the particle flux, while the second term gives the drop in density due to expansion.

The expansion H is determined independently as the early universe is dominated by radiation. When annihilation begins, the first term is dominant. But as the universe expands and the particles' density falls, the expansion term begins to dominate. At this point annihilation stops, and the remaining particles freeze out with a constant density. Through the thermodynamics and expansion physics [29], one can find that the mass density at freeze out is independent of M_χ but inversely proportional to $\langle \sigma_a v \rangle$. If the particle is stable, then this relic density will still exist today. If we take an annihilation cross section corresponding to the weak interaction in particle physics [29],

$$\langle \sigma_a v \rangle = \alpha^2 (100 \text{ GeV})^{-2} \sim 10^{-25} \text{cm}^3 \text{s}^{-1} \tag{1.5}$$

we can obtain a relic density of $\Omega_\chi \sim 0.1$, within an order of magnitude of what we need for the dark matter particles. In other words, if a stable WIMP exists, it will be a kind of dark matter at, or at least near, the density required by the cosmological observation.

From another side, in particle physics, the supersymmetry (SUSY) hyperthesis is developed to unify the four known fundamental interactions in nature. Required by SUSY hyperthesis, every fundamental particle in the Standard Model of particle physics should have a super partner. The WIMP dark matter can be an excellent sample for the SUSY predicted lightest supersymmetric particle (LSP), which is stable and neutral. Therefore, WIMP becomes a naturally prediction from the SUSY hyperthesis.

1.2 The WIMP Direct Detection Methods and Basic Xenon TPC Operation

1.2.1 The WIMP Direct Detection Methods

From Section 1.1, we can see the existence of dark matter in the universe is supported by many cosmological observations and the WIMP becomes a promising candidate for dark matter. However, the nature and properties of dark matter are still undetermined, which motives experimental physicists to detect the WIMP dark matter particle directly. Since at

the level of the weak interaction, the WIMP dark matter particles' interaction cross section with normal matter is very small, most of the direct detection experiments focus on measuring the nuclear recoils signals produced by WIMPs scattering off from a target nucleus in the detector.

In 1985, Goodman and Witten proposed the detectability of WIMP dark matter particle the first time [30]. Assuming both the earth and the dark matter halo keep moving in the galaxy, when the dark matter detector on the earth is hit by a WIMP from the dark matter halo, the WIMP is assumed to be elastically scattered by a target nucleus in the detector which gains kinetic energy up to a few tens of keV [31]. Then the target nucleus becomes a recoiling nucleus. If the signals from the recoiling nucleus can be detected, it will give a strong support of direct evidence of WIMPs. Note, the WIMPs can also make elastically scattered by the outer electrons of the target atom, however, such kind of signals are weak, hence can be ignored.

The biggest challenge of the direct detection experiments of WIMPs is to discriminate between the nuclear recoils signals caused by WIMP and the signals caused by background radiation, such as cosmic rays. For example, the γ rays from cosmos and neutrons from radioactive source can produce electron recoils and nuclear recoils with energy similar to those from WIMPs. In practice, there are two methods to distinguish these signals.

- The interaction cross section of WIMPs is very small, therefore, the WIMP is assumed to be scattered only one time in the detector, whereas other penetrating particles, such as γ and neutrons, will scatter multiple times in a detector. Additionally, the detectors can be placed in deep underground laboratories to shelter the radiations from cosmos;
- Most background radiations will cause electron recoils and deposit energy to the electrons in the detector, whereas WIMPs mainly cause nuclear recoils. Therefore, as long as the nuclear recoils signals can be discriminated from electron recoils, the WIMPs signals can be figured out.

1.2.2 Basic Liquid Xenon TPC Operation

The nature and properties of WIMP dark matter particles require the dark matter search experiments be sensitive and the detectors be able to discriminate between the nuclear resoil

signals and the electron recoil signals. Due to these requirements, Liquid Xenon (LXe) detectors have shown particular promising among lots of direct detection experiments proposed and run in the last two decades [16]. In this section, we firstly review the advantages of liquid xenon as the detector medium and then show the properties of the basic two-phase LXe time projection chamber (TPC).

Since the WIMP dark matter particles' interaction cross section with normal matter is very small, the search sensitivity of the detector will scale with the mass of the detector. Liquid xenon, compared with the crystal scintillator such as NaI or the semiconductor such as Ge, is easy to be scaled. The target medium in a LXe TPC is liquid xenon and the instrumentation scales with the surface area while the sensitivity scales with volume, making these detectors both easy and economical to scale to very large size [32]. As mentioned the successful dark matter detectors today should be able to discriminate signals from electron recoils or nuclear recoils, which can be realized by the two-phase xenon detector. Firstly, xenon itself is easily purified and strongly self-shielding, because xenon is a noble gas and chemical purification is straight forward. Additionally, xenon has no long-lived radioactive isotopes, therefore, extremely low background rates are possible. Secondly, the liquid xenon is an excellent scintillator, while at the same time a sufficient amount of ionization signals can be collected with an applied electric field. Due to the different ionizing density of nuclear and electron recoils in liquid noble elements, the background discrimination can be realized by measuring simultaneously the ionization and scintillation signals from the liquid noble elements. Usually, in this kind of detector, the scintillation signals are detected when the photons are produced while the ionization signals are detected via the proportional scintillation produced in the gas phase after the produced charges are drifted to the gas chamber. Thus this kind of xenon detectors use both liquid and gas as working medium, due to which this kind of detectors are called two-phase detectors.

Interactions in liquid xenon detector can produce both 175 nm scintillation photons and free electrons, where the scintillation signal is prompted and produced in the ∼100 ns following the interaction, which is denoted as S1, and the ionization signal can be collected by drifting the free electrons to the gas chamber through an applied electric field, which is denoted as S2. The delay between the prompt scintillation and the arrival of electrons at the gass chamber collector gives the distance to the interaction, hence the name "time projection chamber" (TPC). Normally, photo-multiplier tubes (PMTs) are used to measure the S1 signals. The PMTs are placed above and below the medium volume to detect the prompt scintillation

signals. The number of primary ionization electrons is very small and cannot be detected efficiently with charge sensitive devices. In two-phase LXe TPC, the primary electrons are drifted from the liquid chamber to gas chamber through a drift electric field E_d in the liquid chamber. Once the free electrons reach the gas chamber, the signals are amplified by means of proportional scintillation (or electroluminescence) using a strong electric field in the gas chamber [33] and becomes the proportional scintillation signal S2, which is also 175 nm scintillation photons and detected by the PMTs. The distinct ratio between the scintillation and ionization, S2/S1, produced by a WIMP (or neutron) interaction and other electromagnetic interaction provides background rejection for the WIMP dark matter searches, allowing a rejection of the majority of the γ and β particles background with an efficiency around 99.5% at 50% nuclear recoil acceptance.

Currently, the experiments using this kind of two-phase LXe TPCs include the XMASS in Japan [34], ZEPIN in the United Kingdom [35], the XENON experiment in the United States [36], and the PandaX experiment in China [37].

1.2.3 Scintillation Efficiency and Ionization Yield of Liquid Xenon Detector

As mentioned, most advanced LXe TPC dark matter detectors work in the two-phase mode with measurements of both S1 and S2 signals. The S1 and S2 signals, together with the relative scintillation efficiency ($\mathcal{L}_{\rm eff}$) and the ionization yield ($\mathcal{Q}_{\rm y}$) respectively, have been used to reconstruct the nuclear recoil energy. Thus $\mathcal{L}_{\rm eff}$ and $\mathcal{Q}_{\rm y}$ are crucial physical quantities for the energy calibration of WIMPs detection.

The so-called *scintillation efficiency* serves as a bridge between the scintillation signal S1 and the depositing energy of the WIMPs in liquid xenon. The energy of a recoiling nucleus is dissipated into the kinetic energy of xenon atoms, excitation energies of excitons and electron-ion pairs, which give rise to phonons (heat), scintillation, as well as ionization. Scintillation efficiency is defined as the fraction of the recoiling energy converted into the scintillation signal. The detector independent value *Relative Scintillation Efficiency* $\mathcal{L}_{\rm eff}$ has been widely used to relate scintillation signal to nuclear recoil energy, defined as [17],

$$\mathcal{L}_{\rm eff}(E_{\rm nr}) = \frac{S_{\rm ee}}{S_{\rm nr}} \frac{S1(E_{\rm nr})}{E_{\rm nr}} \frac{1}{L_y} \ , \tag{1.6}$$

where $S1(E_{\rm nr})$ is the scintillation yield from nuclear recoil with initial energy $E_{\rm nr}$, while L_y is the scintillation yield per keV from electronic recoils with initial energy 122 keV (^{57}Co γ calibration line as the standard candle). The coefficient $S_{\rm ee}/S_{\rm nr}$ corrects for the finite external electric field applied to the detector so that $\mathcal{L}_{\rm eff}$ is drift field independent. The $\mathcal{L}_{\rm eff}$ value actually represents the ratio between scintillations of the nuclear and electronic recoils. This ratio is believed to be independent of any specifics of xenon detectors.

Serving as a link between the ionization signals S2 and the deposited energy of the WIMPs in liquid xenon, the *Ionization Yield* $\mathcal{Q}_{\rm y}$ is defined as the number of observed electrons per unit recoil energy (e^-/keV):

$$\mathcal{Q}_{\rm y}(E_{\rm nr}) = \frac{Q(E_{\rm nr})}{E_{\rm nr}} \ , \tag{1.7}$$

where $Q(E_{\rm nr})$ is the number of electric charges collected from nuclear recoil with initial energy $E_{\rm nr}$. This value is expected to depend on the external electric field but be independent of any specifics of xenon detectors.

A series of experiments [19, 38, 39] have been performed using the mono-energy neutron sources to measure the relative scintillation efficiency ($\mathcal{L}_{\rm eff}$) or ionization yield ($\mathcal{Q}_{\rm y}$) in LXe detectors. However, experimental measurement is difficult for low energy nuclear recoils, which requires forward neutron scattering. As seen in various experiments, the lower the recoiling energy is, the larger the systematic uncertainties will be introduced. The current lowest energy being measured for $\mathcal{L}_{\rm eff}$ is 3 keV nuclear recoil [39], and to lower energy, the relative scintillation efficiency has to be extrapolated as a constant artificially [17]. For the measurement of $\mathcal{Q}_{\rm y}$, there are even less available experimental data and the lowest energy for being measured $\mathcal{Q}_{\rm y}$ is about 4 keV [19] and for lower energy region, it can only be obtained through Monte-Carlo simulation.

In real world, if the WIMPs have mass around 10 GeV/c^2, as some experiments have indicated [40–42], most of the LXe detector events will have nuclear recoil energy around 2 keV or even less, which is right the region where the $\mathcal{L}_{\rm eff}$ and $\mathcal{Q}_{\rm y}$ are unclear. In fact, Collar and McKinsey have pointed out that the liquid xenon response should drop steadily at low-energy because of a kinematic cutoff for production of scintillations [43] which is conflicted with the experimental extrapolation. Using the Fermi momentum for the xenon atom, this value is estimated around 20∼40 keV. For this reason, the XENON100 bound for the light-mass WIMPs has been challenged. They also quoted Monte Carlo studies for the data on the

broad spectrum neutron sources, which indicate a steep drop of the response below 10-20 keV [44, 45] (see, however, a more recent broad spectrum fit from XENON100 [46]).

Obviously, it is hard to obtain accurate data for $\mathcal{L}_{\text{eff}}$ or $\mathcal{Q}_{\text{y}}$ experimentally. In the following chapters, we will study the slowing down process of nuclear recoils in liquid xenon and the scintillation and ionization process to obtain the theoretical predictions for $\mathcal{L}_{\text{eff}}$ and $\mathcal{Q}_{\text{y}}$ as accurate as possible.

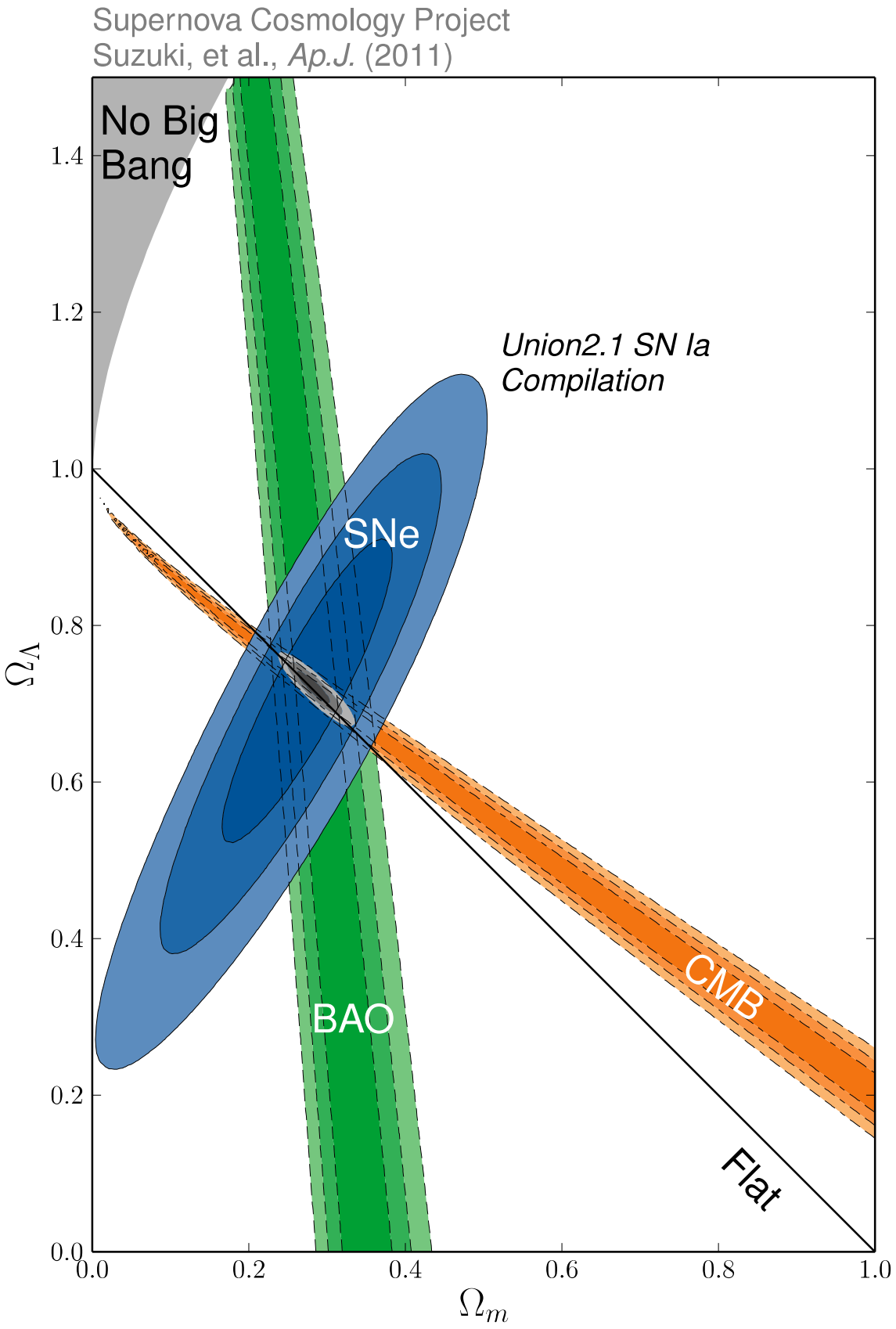

FIGURE 1.1: Cosmological constraints on the mass density Ω_m in the university and the cosmological constant from supernovae, the cosmic microwave background, and galaxy clusters. Figure is taken from from http://supernova.lbl.gov/Union/

Chapter 2

Energy Dissipation of Nuclear Recoils in Liquid Xenon Detector

To evaluate $\mathcal{L}_{\rm eff}$ or $\mathcal{Q}_{\rm y}$ theoretically, a common practice is to firstly apply the Lindhard factor (nuclear quenching factor $q_{\rm nc}(E_{\rm nr}) = \eta(E_{\rm nr})/E_{\rm nr}$) [47] to estimate the fraction of the nuclear recoils energy given to electrons $\eta(E_{\rm nr})$ and then to calculate $\mathcal{L}_{\rm eff}$ or $\mathcal{Q}_{\rm y}$ [48–50]. Simulation programs, such as TRIM [4] or GEANT4 [51], can also be used to derive $q_{\rm nc}$ in a medium. However, both the most cited Lindhard factor and the computer simulations have not been calibrated for low energy recoils, which makes the following evaluations on $\mathcal{L}_{\rm eff}$ and $\mathcal{Q}_{\rm y}$ questionable. Although Lindhard's integral equation [47] provides a clear physics picture for theoretical calculations or computer simulations, the obscure assumptions or approximations behind the results, for example the quoted $q_{\rm nc}$ are quite different in Ref. [48–50] and parameters like displacement energy used in the simulations are still undetermined, motivate us to derive $q_{\rm nc}$ ourselves before calculating $\mathcal{L}_{\rm eff}$ or $\mathcal{Q}_{\rm y}$.

In this Chapter, we analyze the slowing down process of the recoiling nucleus in liquid xenon medium. Then we introduce Lindhard's basic integral equation which shows the theoretical treatments for this process and express the algorithm of a computer program which can simulate the slowing down process pretty accurately.

2.1 Recoiling Nucleus Slowing Down Process

2.1.1 Particles' Slowing Down in Liquid Xenon

In fact, different particles, such as alpha particles, γ rays, neutrons, or heavy nuclei, interacting in liquid xenon involve totally different physics pictures. For details, one can review Ref. [52]. Before talking about the slowing down process, we will firstly give a brief review on the interactions between different particles with a detector medium.

As positively charged helium nuclei, the alpha particles interact with the electrons cloud of the medium atoms via the Coulomb interaction when passing through a medium. As a result, once an electron in the electrons cloud obtain enough energy from the interaction, it can be lifted to a higher energy level within the atom, or can be completely striped from the atom. The alpha particles will continuously encounter such kind of interactions along their trajectory in the medium. Hence, their energy will convert to the ionization or excitation energies and the energetic alpha particles will slow down and finally be thermalized. Since the interaction between the nuclei and an individual electron is tiny and occurs in all directions simultaneously, the interaction only acts as a small "friction" on the alpha particles along their trajectory. Therefore, the particles are not affected by a single interaction and the trajectory of the alpha particles is usually a straight line.

For electron beam, it becomes a different physics picture. Unlike alpha particles, the trajectory of electrons beam may be quite tortuous because the interaction between the incident electrons and the electrons in the electron cloud may be large enough to change the trajectory of the incident electron beam. Additionally, the incident electron and the electron in the medium have the same mass, therefore, the rate of their energy loss is also slower than that of alpha particles.

Regarding γ rays, it is a little complicated. Normally, there are three types of interactions with medium: photoelectric absorption, Compton scattering and pair production. The photoelectric absorption occurs when a γ ray is completely absorbed by the atom and an energetic electron is ejected from one of the bound shells of the atom, where free electrons can be detected. Generally speaking, the low energy γ rays (such as 122 keV γ rays from ^{57}Co) has the highest cross-section and dissipate energy in this way. The Compton scattering occurs when the incident γ ray is deflected and transfers part of its energy to an electron, also the free electrons will be detected. This usually happens in the γ ray energy

around 1 MeV (e.g. 662 keV γ ray from ^{137}Cs). The pair production process can produce an electron-positron pair from the incident γ ray where both electrons and positrons can be detected. It occurs when the γ ray energy exceeds twice the rest-mass energy of an electron (1.02 MeV). The effect becomes dominant for γ rays with energy of several MeV.

Depending on the energy, neutrons show different behaviors in liquid xenon medium. For fast neutrons, nuclear recoils will be produced which is similar to the WIMP. Due to this behavior, experimental measurements of $\mathcal{L}_{\text{eff}}$ or $\mathcal{Q}_{\text{y}}$ are normally using mono-energy neutron sources. If the energy of the neutron beam is high enough, the inelastic scattering of neutron may also occur, where nuclear interaction occurs and the nucleus may be excited to higher energy level. This kind of energy transfer will be finally released as γ rays after the excited nucleus de-excites. Regarding slow neutrons, the dominate interactions are elastic scattering with the nuclei in the medium. Most of the population of slow neutrons are thermal neutrons with the average energy of 0.025 eV at room temperature.

When it comes to the heave particles or recoiling nuclei, it is a different stroy. Let's consider the case for LXe detector in the dark matter detection scenario. When a xenon nucleus is hit by a WIMP dark matter particle, it will get several tens kinetic energy and becomes a recoiling atom. When the recoiling xenon atom moves through the medium, it will be elastically scattered by other xenon atom, which is similar to the binary collision in the classic mechanism, in the medium and change it's trajectory. In the meantime, during the binary nuclear collision occurs, the recoiling xenon will interact with the electrons via inelastic scattering, hence transfer energy to the electrons in the medium due to which the electrons may be excited or ionized. At the same time, due to the elastic collisions between the recoiling xenon nucleus and the xenon nucleus in the medium, the recoiling xenon atom will transfer part of its kinetic energy to a second xenon atom. If the second xenon atom obtains enough kinetic energy from original recoiling xenon atom it can move in the medium and we call this kind of xenon atom as a "secondary" recoiling xenon atom. Hence a collision cascade is generated. During the slowing down process, not only the original recoiling xenon atom can dissipate energy to electrons, but also the "secondary" recoiling xenon atoms can produce electron excitation or ionization. As a consequence, after all the recoiling atoms are thermalized in the medium, the initial energy of the recoiling xenon atom will be dissipated into the kinetic energy of xenon atoms, excitation energies of excitons and electron-ion pairs, which give rise to phonons (heat), scintillation and ionization, respectively. The whole process is in principle quantum mechanical, involves many-body physics and is quite complicated.

2.1.2 Lindhard's Basic Integral Equation

To calculate the electronic energy dissipation during the slowing down process of heavy particle or a recoiling nucleus, Lindhard *et al* proposed an integral equation based on energy conservation law to describe the energy transfer in the collision cascade process [47]. For nuclear recoils, this integral equation can be derived via the following assumptions or considerations:

- Considering the recoiling nucleus has the kinetic energy $E_{\rm nr}$;
- Considering the energy η given to electrons in the medium is zero before the collision cascade process;
- Taking the final average value of η to be $\eta(E_{\rm nr})$ after all the recoiling xenon atoms are thermalized in the medium;
- Assuming the quantity $\eta(E_{\rm nr})$ is additive, i.e. for each separate slowing down process, all recoiling nuclei set in motion contribute additively to η;
- Ignoring effects, such as the physical state of the medium, the recombination of electron-ion pairs and so forth;

In this case, the quantity $\eta(E_{\rm nr})$ for the original recoiling nucleus with kinetic energy $E_{\rm nr}$ can be expressed in another way:

- Supposing the recoiling nucleus moves a path length dR in the medium with N atoms per unit volume;
- Considering the probability $NdRd\sigma_{n,e}$ for a collision specified by energy transfer T_n to the mass center of the struck atom, at the same time part of the energy T_{ei} is transferred to electrons in the medium;
- The collision reduces the original energy $E_{\rm nr}$ to the value $E_{\rm nr} - T_n - \sum T_{ei}$, i.e. the recoiling nucleus will now have a $\eta(E_{\rm nr})$-value equal to $\eta(E_{\rm nr} - T_n - \sum T_{ei})$;
- When collision also produces a "secondary" atom, where the struck atom gets the $\eta(E_{\rm nr})$-value $\eta(T_n - U)$, where U is the energy wasted in disrupting the atomic binding;

Finally, the electrons produced are described by another $\eta(E_{\rm nr})$-value, which we denoted as $\eta_e(E_{\rm nr})$, and their contributions to $\eta(E_{\rm nr})$ after the collision in question are then $\sum \eta_e(T_{ei} - U_i)$, where U_i are the corresponding ionization energies. The above probability timed the total $\eta(E_{\rm nr})$-value after the collision gives the contribution fo this collision to $\eta(E_{\rm nr})$. Then we integrate over all collisions. Something left is a probability $1 - NdR \int d\sigma_{n,e}$ that no collision occurs. In this event, the $\eta(E_{\rm nr})$-value remains $\eta(E_{\rm nr})$.

Through above contributions, then an integral equation for original $\eta(E_{\rm nr})$-value can be shown as:

$$\eta(E_{\rm nr}) = NdR \int d\sigma_{n,e}\{\eta(E_{\rm nr} - T_n - \sum T_{ei}) + \eta(T_n - U) + \sum \eta_e(T_{ei} - U_i)\} + (1 - NdR \int d\sigma_{n,e})\eta(E_{\rm nr}) \ ,$$

which leads to the basic integral equation

$$\int d\sigma_{n,e}\{\eta(E_{\rm nr} - T_n - \sum T_{ei}) - \eta(E_{\rm nr}) + \eta(T_n - U) + \sum \eta_e(T_{ei} - U_i)\} = 0 \ . \tag{2.1}$$

Based on Lindhard's basic integral equation Eq. (2.1), the following Lindhard factor is derived theoretically to estimate the fraction of the energy given to electrons $q_{\rm nc}(E_{\rm nr}) = \eta(E_{\rm nr})/E_{\rm nr}$, which is also called nuclear quenching factor:

$$q_{\rm nc}(E_{\rm nr}) = \frac{\eta(E_{\rm nr})}{E_{\rm nr}} = \frac{kg(\epsilon)}{1 + kg(\epsilon)} \ , \tag{2.2}$$

where $\eta(E_{\rm nr})$ is the energy transferred to electrons when the initial nuclear recoil energy is $E_{\rm nr}$. $g(\epsilon)$ is an empirical expression which can be found in Ref. [31] and k is the proportionality constant between the electronic stopping power $(dE/dx)_{\rm el}$ and the velocity of the projectile (recoil atom). For xenon, Lindhard proposed a value $k = 0.166$ [47]. Considering the specific track structure of the nuclear recoils caused by the collision cascade, Hitachi re-calculated the electronic stopping power of recoiling xenon atoms in a liquid xenon target and derived a smaller value $k = 0.110$ [48]. However, both authors seem to overestimate the total electronic energy dissipation due to ignoring the faster fall-off behavior of the electronic stopping power in low energy region, which has been observed by some experiments [1].

On the other hand, simulation programs, such as TRIM [4] (TRansport of Ions in Matter), have been developed to simulate the ion transport processes in a medium, which could be used to estimate collision energy loss of the recoiling atom. But these programs are usually good

for high ion energies, and implemented without specific considerations on the microscopic properties of the liquid xenon. In addition, there are quite some parameters which are unclear in low energy region. For example, some unknown parameters, such as displacement energy or binding energy of an atom, will have big impact on the final result, however, in TRIM, they are set artificially. Therefore, this kind of simulation program is not calibrated in low energy region. So far, no theoretical approach has been realistic enough to account for the nuclear quenching factor q_{nc}, and to predict the behavior at the keV-scale recoiling energy.

2.2 Computer Simulation of the Slowing Down Process

To derive the more accurate nuclear quenching factor q_{nc}, we have to consider the specific microscopic properties of the liquid xenon and use unclear parameters as few as possible. In this Section, we describe a Monte Carlo program which can simulate the xenon atom's recoil behavior inside the liquid xenon medium, where the energy dissipation in a collision cascade is considered specially.

Generally speaking, the computer simulations for particles' moving through a medium have been known for decades, for an example, the well-known SRIM package has been updated frequently and widely used [4]. However, for specific particles and medium, such kind of simulations do not take special consideration. In this work, we intend to improve the previous simulations for the low energy (∼keV energy region) nuclear recoils relevant for direct dark matter detection in several aspects. Of course, this type of simulations has not yet been completely *ab initio*. For instance, the electronic excitations are intrinsically inelastic quantum mechanical processes, and the charge states of the collision atoms might have significant changes during the collisions. However, a complete account of all these features requires treatment of many-body quantum dynamics, and is beyond the present scope. Considering all of these effects becomes an impossible mission for a computer program. Luckily, even though these effects could be important for low energy recoils, we can account for them in some average sense to ensure the result does not be drastically affected by the approximations.

2.2.1 Simplification for the Slowing Down Process

Unlike electron recoils whose kinetic energies are all dissipated into electronic energy of the media, the energy dissipation process of nuclear recoils is more complicate. When a xenon nucleus is scattered by a WIMP dark matter particle and recoils inside the liquid xenon medium, atomic motions, electronic excitations and ionizations are generated, and the whole process is in principle a many-body quantum mechanics problem. To find the equivalent electronic energy dissipation to electron recoils, it is necessary to make reasonable simplifications to render a theoretical treatment feasible. Similar to the previous works, one of the simplifications we are using is to regard the motions of the xenon atoms classically, like billiard balls. Since the xenon atom's de Broglie wavelength (less than 0.0025 Å) in the concerned energy region (0.5∼25 keV) are much smaller than the atomic scale and the distance (3.5∼6.2 Å) [53] between two neighboring nuclei, the quantum effects can be ignored. Hence, we allow the xenon atoms move along classical trajectories determined by the inter-atomic potential $U(r)$, projectile nuclei energy E and the impact parameter b, in the atomic collision processes. At the same time, the nucleus-electron interaction is treated as a small "friction" on the nucleus along the trajectory because the mass of the electron is much smaller than that of the nucleus and electrons cannot change the trajectory of the nucleus significantly. Therefore, we can suppose that the atomic scattering generates large momentum transfer, hence has a large influence on the atom trajectory, but little energy dissipation, whereas the atom-electron interaction generates little momentum transfer but large energy dissipation. The latter can be considered as a small energy perturbation to the atomic motion. This in some sense is similar to the famous Born-Oppenheimer approximation in quantum mechanics.

Since the slowing down process of a recoiling nucleus is a collision cascade, we have to track the whole collision process of the initial recoiling nucleus and the "secondary" recoiling nuclei using a Monte Carlo simulation program. For each event, the recoiling xenon atom begins with an initial energy, position and direction, randomly generated with certain constraints, which will discuss these in the following section. As we analyzed in last paragraph, the xenon atom can be regarded to move in a slightly curved trajectory between two binary atomic collisions and change direction mainly as a result of the nuclear binary collisions. During the atom's motion, the kinetic energy is dissipated to the neighboring atoms in discrete amounts through elastic binary atomic collisions and to the electrons continuously through inelastic

electronic reactions. The later process is superimposed on to the former and is averaged over all possible electronic excitations. At last, the trajectory of a moving xenon atom is terminated when its kinetic energy drops below a predefined energy where the remaining energy entirely results in heat.

The goal for this program is to calculate the total electronic energy loss, therefore, in this program we need not to track the detailed inelastic electronic excitations and the path of the recoiling nuclei in the collision cascade. We only need to record the electronic energy dissipation between every binary atomic collision. In this program, we compute the electronic energy dissipation in every binary atomic collision based on the quantity, electronic stopping power S_e, and sum them up through the whole cascade,

$$\eta(E_{\rm nr}) = \sum_{i=0}^{N} \int_0^{\lambda(E_i)} S_e(E_i) dx \ , \tag{2.3}$$

where $\lambda(E_i)$ is the free flight path length of a recoiling atom with initial energy E_i, and $S_e(E_i)$ is the energy loss to electronic excitations per unit path, also called electronic stopping power and written as $(dE/dx)_{\rm el}$, N is the total number of binary atomic collisions that the recoiling atom can result in with the initial kinetic energy $E_{\rm nr}$. Clearly, this is an approximate picture because the electronic energy loss here is appended to the collision cascade as a statistical as well as quantum-mechanical average.

2.2.2 Nuclear Binary Collision Mechanism

In this simplification program, the energy transfer between two nuclei is assumed to be through the binary atomic collision. This kind of collision can be regarded like billiard balls. When considering the energy transfer in binary atomic collisions, we use the classical elastic scattering approximation. Elastic scattering slows down the recoiling atom through momentum transfer to the target atom and changes the track structure of the original trajectory. At the same time, both the original recoiling atom and the struck atom become the "secondary" recoiling atoms which may trigger more "secondary" recoiling atoms, hence produce a collision cascade. Based on the binary collision kinematics shown in Fig. 2.1, we have the energy transfer to the target in a collision [54]

$$T = E_0 \sin^2(\theta_c/2) \ , \tag{2.4}$$

where T and E_0 is the transferred energy and projectile energy of the initial nucleus in lab frame. The scattering angle in the center-of-mass frame θ_c can be derived from the following expression [54]

$$\theta_c = \pi - 2b \int_{r_0}^{\infty} \frac{1}{r^2 \sqrt{1 - U(r)/E_c - b^2/r^2}} dr \ , \tag{2.5}$$

where b is the impact parameter and E_c is the energy in the center-of-mass frame. The lower limit r_0 is the nearest distance between the projectile and target nuclei determined by the following equation

$$1 - \frac{U(r)}{E_c} - \frac{b^2}{r_0^2} = 0 \ . \tag{2.6}$$

We choose the screened Coulomb potential for the inter-atomic interaction,

$$U(r) = \frac{Z^2 e^2}{r} \Phi \left(\frac{r}{a} \right) \ , \tag{2.7}$$

where $\Phi(\frac{r}{a})$ is the Hartree-Fock screening function and $a = \frac{1}{2}(\frac{3\pi}{4})^{2/3} \frac{a_0}{2Z^{0.23}}$ is the Hartree-Fock screening radius for xenon (a_0 is the Bohr radius). The empirical expression for the screening function is [4],

$$\Phi(x) = 0.1818e^{-3.2x} + 0.5099e^{-0.9423x} + 0.2802e^{-0.4028x} + 0.02817e^{-0.2016x} \ . \tag{2.8}$$

In our simulation, b is randomly generated according to the spatial distribution of xenon atoms as we will explain latter. The scattering angle θ_c and the energy transfer to the target are calculated through Eq. (2.5) and Eq. (2.4).

The free flight path of the recoiling atom between two successive collisions is another parameter when calculating the electronic energy dissipation. Since the interaction between the recoiling nucleus and the electrons only slows the recoiling nucleus slightly, the slightly curved trajectory of the recoiling nucleus is caused by the inter-nuclei Coulomb force. In this program, to identify the length of the trajectory between the binary atomic collision, we set the curve to connect two points: the initial position of the projectile and the ending position where the projectile and the target nuclei are closest. The length of the flight path is a curvilinear integral from the two atoms' initial distance $r = R$ to their closest point $r = r_0$ along the trajectory

$$\lambda = \int_{r_0}^{R} \sqrt{dr^2 + r^2 (d\chi)^2} \ , \tag{2.9}$$

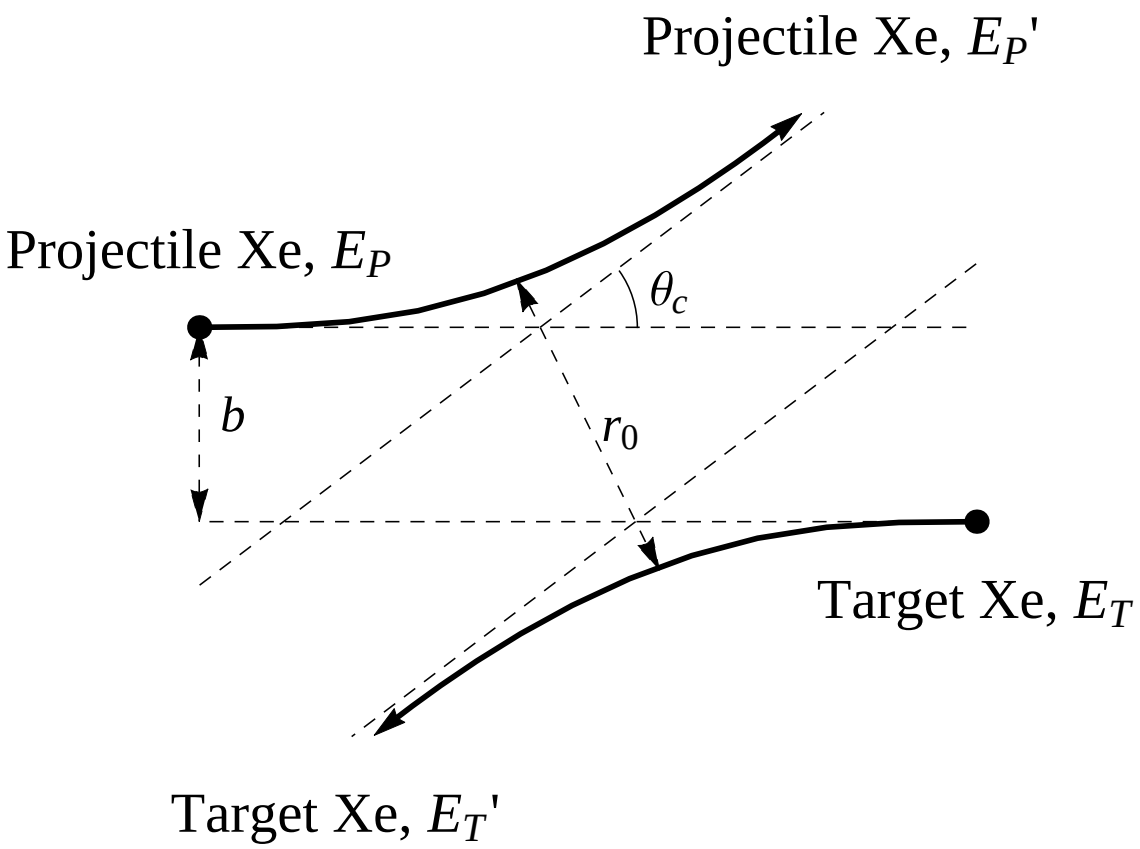

FIGURE 2.1: Kinematics for classical binary collision of Xe atoms in the center of mass coordinates.

where $\chi = \theta_c/2$ is polar angle. Applying the trajectory equation from Eq. (2.5), λ could be rewritten as

$$\lambda = \int_{r_0}^{R} dr \sqrt{1 + \frac{b^2}{r^2(1 - U(r)/E_c - b^2/r^2)}} \,. \tag{2.10}$$

2.2.3 Pair Correlation Function of Liquid Xenon

In most simulation programs like GEANT4 [51] and TRIM [4], the medium is simplified as homogeneous in which the atoms are randomly distributed according to a uniform probability distribution. Here we consider a more realistic spatial distribution of nuclei in liquid xenon. The difference is mainly in the locations of the neighboring atoms. Since the collisions in liquid mainly involve these atoms, a realistic probability distribution at small distance scale is important in determining the free flight paths and the impact parameters. For a homogeneous medium like liquid xenon, the spatial distribution of the atoms is characterized by the radial distribution function, also called pair correlation function (PCF) $g(r)$, which is defined

as the probability of finding a particle at distance r from a reference particle. Generally speaking, the pair correlation function is determined by the inter-atomic interactions and the environmental temperature. The function can be calculated theoretically using molecular dynamic simulations or measured experimentally in neutron diffraction. Here we take $g(r)$ from Ref. [53], as shown in Fig. 2.2.

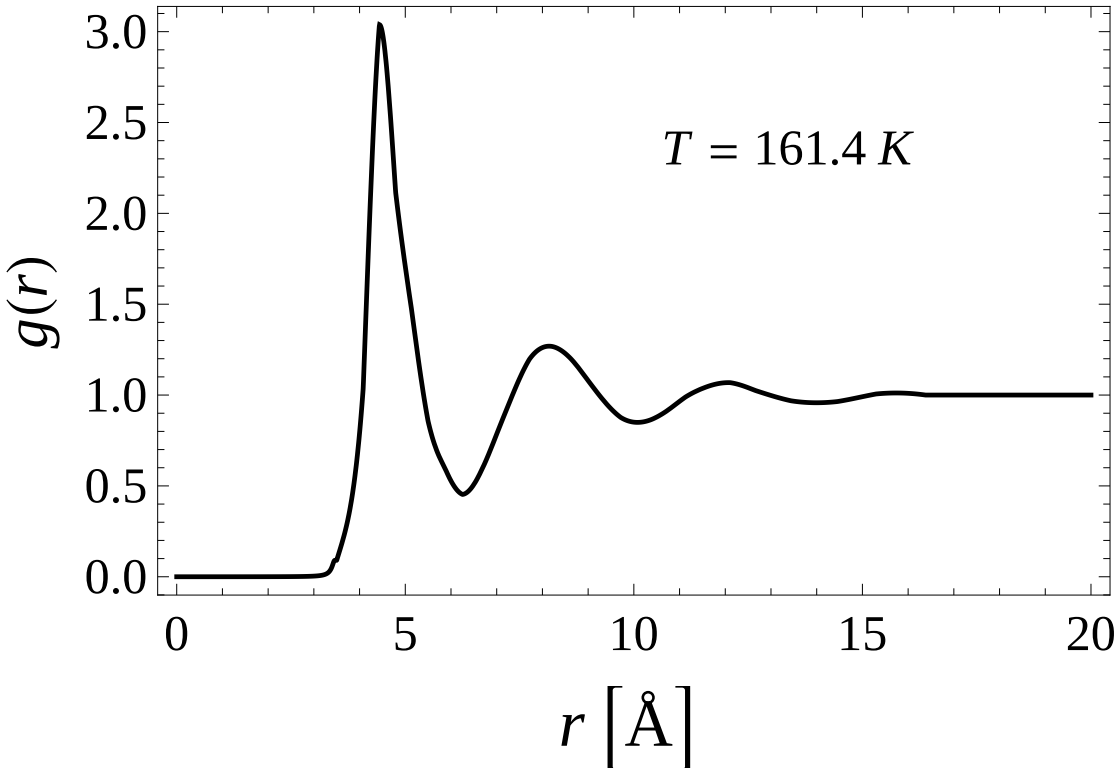

FIGURE 2.2: Pair correlation function $g(r)$ of the xenon atoms in the liquid phase at 161.4 K. The PCF shows the nearest neighbor atoms of the projectile atom mostly distributes between the inter-atom distance R form 3.5 to 6.2 Å with central value at 5.0 Å.

Considering a xenon atom getting the initial momentum from either a WIMP dark matter particle or a recoiling xenon nucleus, it then becomes a projectile atom which may result in further binary collisions. The target xenon atom participating in the subsequent collision can be selected from the 5 to 6 nearest neighbors of the projectile in the forward direction of the projectile particle. To simulate the nearest neighbor target, we can use only two parameters: a distance (R) to the projectile atom and an angle (Θ) between the radial and projectile moving directions. The distance R is distributed according to the pair correlation function $g(r)$, and generated using Acceptance-Rejection method. After the nearest neighbors are generated, we choose the one whose distance to the projectile nucleus is smallest as the target for the binary atomic collision. The angle Θ is distributed in a way that makes atoms to distribute isotropic. Note, for an individual binary atomic collision, the angles Θ should

follow the spatial distribution of the neighbors. However, in a large number of binary atomic collisions, the angles are expected to satisfy above distribution due to the isotropic nature of the liquid. Once a pair of R and Θ is determined, we calculate the impact parameter as

$$b = R \sin \Theta \ . \tag{2.11}$$

After the nearest neighbor or the target atom is identified, we can consider the collision cascade process. When the projectile nucleus is scattered, its kinetic energy is transferred partially to the target and the moving direction is changed. The two nuclei will be regarded as new projectile particles and further scattered by the other target nuclei, and so on. During the binary atomic collisions, the electrons-nuclei interaction is treated as a small friction, which results in energy dissipation from the projectile to the electrons of its neighbors [55]. We generally ignore the charge state of the atoms by assuming all atoms interact with a screened potential described previously, which is a good approximation at low energy.

2.2.4 Kinematic Cutoff Energy

Now we need to define a kinematic cutoff energy or a threshold energy below which the energy transfer from the moving particle to atomic electrons is forbidden, which means we regard this part of energy finally becomes phonons (heat). This cutoff in a sense simulates the minimal energy cutoff discussed in Ref. [43], which is a quantum mechanical effect. Ficenec *et al.* have discussed the quantum effect in their research on electronic excitation by extremely slow protons in Ref. [56]. In that work, the authors estimate the threshold energy using simple two-body kinematics and regard that energy transfer from the ionizing particle to an atomic electron is forbidden if the minimum excitation energy of the system E_g exceeds the maximum possible energy transfer to the electron. Based on this assumption, they derive a threshold velocity for the moving particle,

$$v_{th} = E_s / 2 m_e v_F, \tag{2.12}$$

where m_e is the electron mass and v_F is the Fermi velocity of the atomic electrons. Identifying E_g with the gap energy in liquid xenon (9.3 eV), the cutoff energy is calculated as 20$\sim$40 keV. However, the experimental measurements has shown that this type of estimation does not work, although a down-ward trend in the scintillation starts to appear at that

energy. In Ref. [56], the authors notice that even extremely slow protons with velocity far below the calculated threshold velocity can excite atomic electrons. XENON100 experiment has observed scintillation and ionization when the recoil xenon energy is down to 3 keV.

Theoretical arguments indicate that classical process with a continuous energy transfer can be brought to reconciliation with the quantum mechanical mechanism of discrete energy transfer through some statistical sense [57]. In our case, the kinematic cutoff shall be reflected through a fast fall-off of the electronic stopping power at low energy, vanishes entirely below the gap energy. As we shall see, since our model for electronic stopping power will not include this cutoff, we take care of the kinematic cutoff effect using the following criteria instead: if the kinetic energy of the initial projectile xenon is lower than the gap energy in liquid xenon (9.3 eV), no electronic excitations or ionizations will be produced. We will terminate the trajectory when the kinetic energy of the moving particle is approaching the thermal energy of atoms in liquid xenon (0.021 eV).

Chapter 3

Electronic Stopping Power and Electronic Energy Dissipation

The average energy loss of a moving atom or ion to electronic excitations or ionization of the medium can be described by the so-called electronic stopping power $(dE/dx)_{\mathrm{el}}$, or linear energy transportation which equals electronic stopping power divided by the medium density. As mentioned in Chapter 2, the electronic stopping power is very important when evaluating the electronic energy transfer during the slowing down process of the recoiling nuclei. In principle, the electronic stopping power, as a function of the projectile's kinetic energy, can be measured experimentally. However, there is few data at the low energy region of our interest, where the information is crucial for direct WIMP dark matter detection. Thus we have to rely on theoretical models and limited experimental data at moderate energies to make progress. Since this is one of the main uncertainties in the present study, we will consider this issue in details in this Chapter.

In this Chapter, we review the theoretical treatment for the electronic stopping power and the experimental measurements for the electronic stopping power of xenon for xenon atom in history. After that, we show some improvement for the theoretical calculation of electronic stopping power and show what we have used in the final calculation.

3.1 Theoretical models for electronic stopping power

The problem of a moving particle dissipating its energy in the condensed matter is one of the continuing interests in physics. The energy dissipation is normally divided into two parts: loss of energy to electrons and atomic recoils respectively, corresponding to the electronic stopping power S_e and the nuclear stopping power S_n. Normally, the nuclear stopping power S_n is only significent for heavy particles or nuclear recoils. The energy loss to electrons is reflected by the value electronic stopping power $S_e = (dE/dx)_{\mathrm{el}}$, defined as the average energy loss per unit length, or the value linear energy transfer LET, defined as the electronic stopping power divided by the medium density. Study of the electronic stopping power for a charged particle passing through a matter medium has been a great interest for more than one century [58]. There is a huge literature about this subject, ranging from classical theories to quantum mechanical ones, as well as semi-classical and semi-empirical ones. The original approach of Bohr has been extended by including screening, high-order-Z and shell corrections, high-speed quantum and relativity corrections as well as projectile excitation and ionization, which is reviewed in Ref. [59], resulting the so-called binary stopping theory which seems to describe the experimental data on a wide variety of ion-target and ion-energy.

Our interest is in the low energy region with kinetic energies of projectile particles between 1 and 100 keV. The physics here is usually more complicated than that at high energies region because perturbative approaches usually do not work. In history, many theoretical models have been proposed to simplify the complicated situation in low energy region, among which the linear response method [60] and transport cross section method [61] are widely used to theoretically calculate electronic stopping power. Both methods regards the incident particle, when moving through the medium, passes through the electron gas of constant density [62] and dissipates energy to the electrons. Calculations based on either methods show that S_e is nearly proportional to the velocity v of the incident particle. Following the pioneering works, authors try to derive more accurate results by correcting these models from aspect of the incident particle, such as effective stopping power charges concept [60] or nonlinear density functional calculation [61], where the velocity proportional relation still exists after the corrections.

3.1.1 Transport Cross Section Theory

To well describe the case of slow ions whose velocity is smaller than the Fermi velocity of the electrons in the medium, the so-called transport cross section method has been proposed. When the velocity of the incident particle v is far below the electrons' Fermi velocity v_F in the medium, the interaction between the incident particle and the electrons in the medium can be regarded as that the electrons are scattered in the field of the incident particle. The electrons' momentum increment causes the energy dissipation of the incident particle to the electrons in the medium. Based on this method, the electronic stopping power expression is derived as:

$$S_e = n_0 v_F \sigma_{tr}(v_F) v \ , \tag{3.1}$$

where n_0 is number density of the electrons in the medium which is related to the Fermi velocity through:

$$v_F = \frac{(3\pi^2 n_0)^{1/3}\hbar}{m_e} \ . \tag{3.2}$$

In Eq. (3.1), $\sigma_{tr}(v_F)$ is the usual transport cross section which is given by:

$$\sigma_{tr}(v_F) = \int (1-\cos\theta) d\sigma = \frac{4\pi}{k_F^2} \sum_{l=0}^{\infty} (l+1) \sin^2(\delta_l(v_F) - \delta_{l+1}(v_F)) \ , \tag{3.3}$$

where θ is a scattering angle and δ_l is the phase shift of the lth partial wave for scattering of electrons at the Fermi surface from the screened potential of the incident particle. If the electron density n_0 is constant, the electronic stopping power will be proportional to the incident velocity v.

Based on this assumption and considering the electrons distribution on the incident particle, Echenique *et al.* [61] have made a nonlinear density-function calculation, which shows the variations of stopping power with incident particle charge, the Z oscillations, which gives a relatively accurate electronic stopping power.

Lindhard and Scharff (L-S), presumably based on the transport cross section and classical scattering approximation, found that at low energy [63] the electronic stopping power can be expressed as:

$$S_e = \sqrt{8}\pi e^2 a_0 \zeta_0 Z N_0 \frac{v}{v_0} \ , \tag{3.4}$$

where a_0 and v_0 are Bohr radius and Bohr velocity respectively and ζ_0 is an empirical parameter, which is set to $\zeta_0 = Z^{1/6}$ in Lindhard's paper although this can be a model-dependent parameter. N_0 is the number density of the target medium. The above expression assumes that the projectile and target atoms are the same, and the electron density follows Thomas-Fermi distribution.

In a quasi-classical treatment for inelastic energy losses by Tilinin [64], the Coulomb repulsion between the nuclei of colliding particles has been shown to decrease greatly the electronic stopping in the small projectile energy, where the large impact-parameter collisions become dominant and the amount of the atomic electrons involved in inelastic interaction is reduced drastically. He used a screening potential to calculate the energy dependent coefficient $\tau(E)$ in the L-S electronic stopping power, which goes to one at large energy, but becomes substantially smaller at small E. Tilinin's study shows that at low energy region the stopping power decreases like v^3 instead of v.

3.1.2 Linear Response Theory

When a moving atom passes through the electron gas formed by the electrons of the atomic outer shell, it perturbs them and induces a fluctuation of the electron density. The electrons are reassembled around the projectile atom such that the electrons in the forward direction of the projectile atom are more dense than those in the backward direction. This density difference produces an induced electronic field. The moving atom must overcome the force exerted by this electric field and dissipates its energy in the form of the atomic electron excitations in the medium.

The most cited work along this direction is that of Brandt and Kitagawa (B-K) effective charge theory [60], which has been further improved by other authors. Brandt and Kitagawa introduced the concept of effective charges for ions. Using the effective charge, the electronic stopping power S_e of a heavy ion can be scaled from proton's stopping power S_p, at the same velocity in the same medium as below:

$$S_e(Z_1, Z_2; v) = [Z_1^*(v)]^2 S_p(Z_2; v) \ , \tag{3.5}$$

where Z_1 is the atomic number of the projectile ion or atom while $Z_1^*(v)$ is the effective charge number of the projectile ion or atom at velocity v, and Z_2 is the atomic number of

the medium. Using B-K effective charge theory, one can evaluate the stopping power using the effective charge of a heavy projectile particle through the proton data.

3.1.3 Comparison between Theoretical Predictions and Experimental Data

Although many authors have spent decades trying to understand and calculate the electronic stopping power, the calculations are not consistent with each other and deviate from the experimental data quite much [1] in low energy region. Based on thousands of experimental data and the various theories, Ziegler *et al.* [4] proposed semi-empirical results which are consistent with available data and summarized them in a Stopping/Range Table, which also shows a velocity proportional property of stopping power at low energy. As shown in Fig. 3.1, the SRIM data is substantially lower than the prediction of L-S and B-K theories, but higher than that of Tilinin. However, no theoretical prediction can show the right fall off tendency of the electronic stopping power in low energy region.

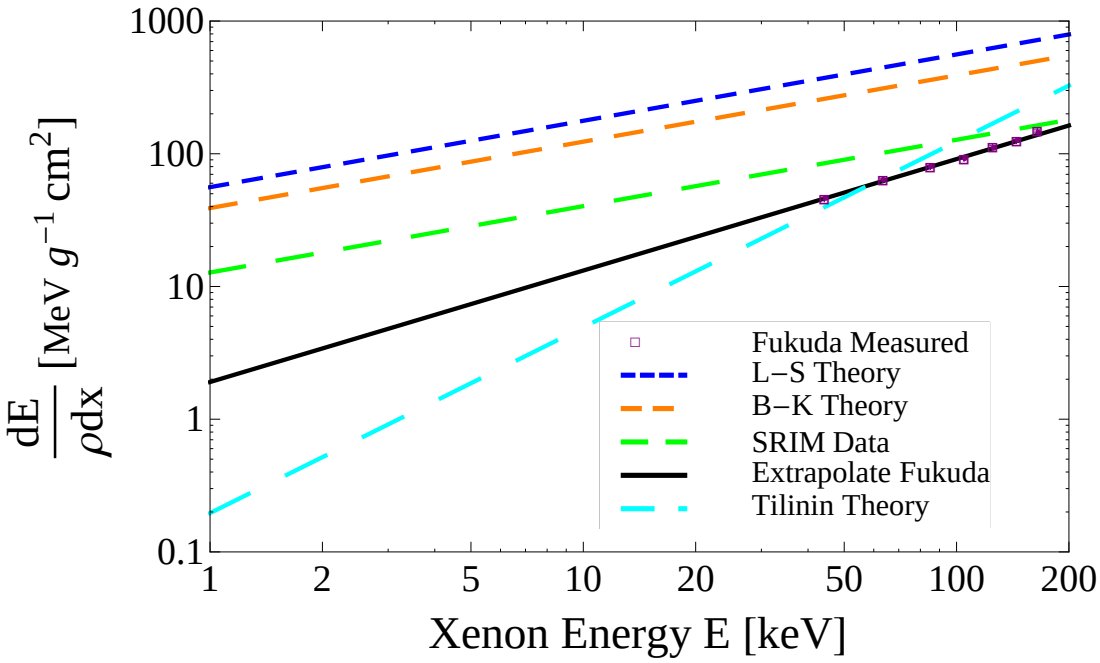

FIGURE 3.1: Comparisons between different theoretical predictions and experimental data [1] on the electronic stopping power for a xenon atom in LXe. The electronic stopping-power fitted from Fukuda's measured data ($S_e(E) = 1.906 \times E^{0.84}$) is shown as solid line, whereas other predictions are shown as dashed lines with different colors.

3.2 Improvement for Transport Cross Section Method

3.2.1 Effective Electron Density

Assume a slow projectile particle is moving through an electron gas of density n_0 with velocity v much less than the Fermi velocity v_F of the electron gas. Along its trajectory, the projectile through Coulomb interaction transfers momentum to electrons of the medium hence loses energy. The trajectory is distorted through binary elastic collision when the projectile approaches a target nucleus in the electron gas to the nearest distance. Considering the scenario that the electrons are scattered in the field of the projectile particle, the electrons' momentum increase can be evaluated using the so-called transport cross section $\sigma_{\mathrm{tr}}(v_F)$. In this way, one finds the expression for the electronic stopping power as Eq. (3.1). Given a constant electron density n_0, the transport cross section approach predicts that the electronic stopping power is proportional to the projectile velocity v which is similar to other theoretical predictions.

For conductor like metal elements, where there are many delocalized free electrons which form the uniform electron gas, the transport cross section approach gives very good theoretical predictions. It provides an accurate theoretical expression for the experiment measured Z_1-oscillation behavior (the electronic stopping power of a medium oscillates with the variation of the atomic number Z_1 of the projectile particle) [61, 65]. However, it becomes a different case when applying this approach to insulators like liquid noble elements. There are two issues one must take into account:

- Whether the electrons in the medium can be regarded as uniform electron gas or not;
- How to evaluate the density for the electrons in such kind of medium, or in another word, how many electrons are involved in the interaction with the projectile.

Firstly, the insulators, such as liquid noble elements, have few free electrons and most of the electrons are bounded to every isolated atom. Obviously, the density of the bound electrons which form the electron cloud varies with the distance between the electrons and the nucleus. The closer to the nucleus, the denser of the electron cloud will be. Secondly, when the low energy projectile moves through the electron cloud, it cannot penetrate the electron cloud as deeply as that with high energy. In this case, the trajectory of the projectile in the electron

cloud should be considered when evaluating the electron density which will be involved in the interactions. Now the physics picture becomes clearer: to determine the electron density for transport cross section approach regarding insulator media, one has to consider both the distribution of the bound electron of an atom and the trajectory of a low energy projectile.

To find the electron density of an isolated atom, the existing most accurate approach may be the Hartree-Fock (HF) method, also called the self-consistent field method (SCF). But this method is not that practical and makes the problem much more complicate since a detailed account of the electron distribution is unnecessary, besides being clearly a cumbersome task, and what is required is an averaged picture. Therefore, we directly use the Poisson equation to find out the density of the electron cloud,

$$\rho(r) = \epsilon \nabla^2 \Phi(r) \ , \tag{3.6}$$

where $\Phi(r)$ is the potential around the atom in the medium. No matter which potential is chosen, the electron density will rely on the distance to the nucleus. The bigger the distance is, the smaller the electron density will be. By choosing the right potential, we can evaluate the electron density of the electron cloud pretty accurately.

Since the low energy projectile cannot penetrate the electron cloud deeply, only part of the electrons in the cloud are scattered by the projectile. Considering this behavior, we only take the electrons along the trajectory into account. This treatment can also avoid the argument how many electrons should be involved in calculating the electron density. When a projectile particle moves through a dense medium, the trajectory is determined by the binary collision between projectile and target nuclei in the medium which can be described by the inter-atomic potential $U(r)$, projectile' energy E_p and the impact parameter b between the projectile and the target. In the meantime, the interaction with electrons can be regarded as small "fraction" along the trajectory. Ignoring the "fraction", the trajectory can be expressed by following equation in polar coordinate $\theta - r$ in classical binary collision approximation [54],

$$\frac{d\theta}{dr} = -\frac{b}{r^2}\left(1 - \frac{2U(r)}{E_p} - \frac{b^2}{r^2}\right)^{-1/2} \ . \tag{3.7}$$

From Eq. (3.7), we can find out the nearest distance r_0 between the projectile and target nuclei by solving the equation,

$$1 - \frac{2U(r)}{E_p} - \frac{b^2}{r^2} = 0 \ . \tag{3.8}$$

Assume the radium of the atom in the medium is R, then the projectile can penetrate the spherical shell from R to r_0. We take into account that the electrons located in the spherical shell are involved in the interaction with the projectile. And then we can calculate the average electron density in the spherical shell using Eq. (3.6), which we call effective electron density for insulator media in transport cross section approximation.

Now the only problem left is that for a projectile particle, the specific initial energy E_p and the inter-atomic potential $U(r)$ are defined clearly whereas the impact parameter b between the projectile and the target is a random number. Which impact parameter b should be choose to calculate the effective electron density? It is obvious that there is no special impact parameter b. Therefore, in our treatment, for different initial projectile energy E_p, we try to calculate an average electron density along every trajectory which is determined by every specific impact parameter, and then average all the electron density for different trajectory. We regard the final average one as the effective electron density.

3.2.2 Improvement for Existing Transport Cross Section Theory

Now we can calculate the electronic stopping power using transport cross section method together with the effective electron density. Applying the method to liquid xenon, we finally calculate the electronic stopping power of liquid xenon for xenon atom. In this work, we use the Van der Waals radius of xenon atom (216 pm) as R. To determine r_0, we choose Moliere potential as the inter-atomic potential $U(r)$ and we regard the distribution of the impact parameter b as quadratic uniform. Then we can calculate the average electron density n_0 and electron Fermi velocity v_F. When calculating transport cross section, we use Moliere potential in the Schrödinger equation to find the phase shift of the partial wave.

We calculate the electronic stopping power of liquid xenon from 1 keV to 100 keV. After that, we fit the power-law exponent and the coefficient to our calculation. The best fit yields:

$$S_e(E_p) = \begin{cases} 2.85 \times E_p^{0.78} & E_p < 50 \text{ keV} \\ 5.53 \times E_p^{0.61} & E_p >= 50 \text{ keV} \end{cases} \tag{3.9}$$

A comparison of experimental data with the predication from the corrected transport cross section method are shown in Fig. 5.2. Along with our calculation, we have also shown the theoretical prediction from other authors and the experimental data in mediate energy

region. The blue dashed curve is the result from Lindhard-Scharff (L-S) theory [63]. The orange dashed curve shows the result from Brandt-Kitagawa (B-K) theory [60]. The green and cyan dashed curves are results from SRIM [4] and Tilinin's [64] predictions respectively. The red dots are from the Fukuda's measurement [1]. This result shows the electronic stopping power of liquid xenon tends to drop more quickly in low energy region and tends to approach the same result as SRIM in high energy region.

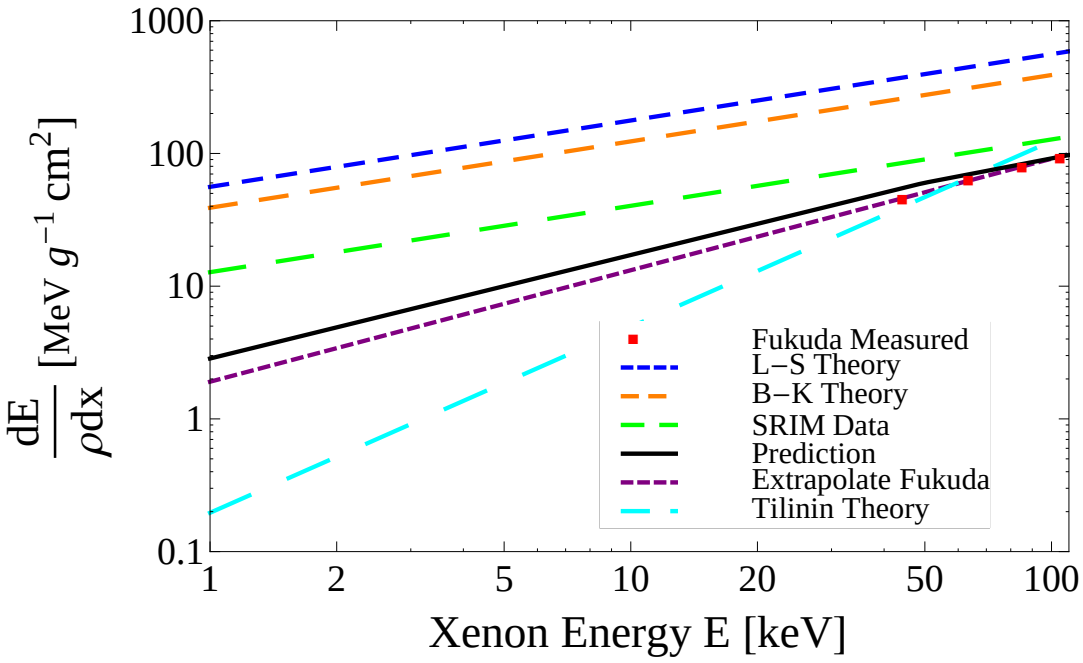

FIGURE 3.2: Comparisons between different theoretical predictions, which are shown as dashed lines with different colours, and experimental data [1] on the electronic stopping power for a xenon atom in LXe. The stopping power fitted from Fukuda's measured data $S_e(E_p) = 1.906 \times E_p^{0.84}$ is also shown.

3.3 Electronic Stopping Power in Real World

To get some idea about the reliability of these theories, we compare them with the available experimental data [1, 66], as shown in Fig. 3.1. The data here is based on the stopping power in gas phase measurements at low energy region (40 keV to 200 keV) [1]. In this experiment, the xenon ions are accelerated by a Cockcroft and Walton type accelerator and pass through a differentially pumped large gas cell, which contained the xenon gas whose stated purity is 99.9%. After the ions transit the target, they are measured in an electrostatic energy analyzer and the electronic stopping power is derived. In the error analysis, the impurities, multiple

scattering and nuclear stopping power have been taken into account. The experimental data are listed in Table (3.1)

Gas	Xe^+ energy (keV)	Stopping Power (10^{-15} eV cm^2 atom^{-1})
Xe	44.22	9.98±0.20
	63.43	13.85±0.27
	85.07	17.43±0.35
	104.68	20.18±0.40
	124.89	24.62±0.48
	144.68	27.34±0.54
	164.54	32.26±0.63

TABLE 3.1: The experiment measured electronic stopping power in xenon gas for 40-200 keV xenon ions

Of course, what we need is the stopping power in the liquid phase. Some authors [67–69] have discussed and measured the phase effect of electronic stopping power in metal gas and solid phases. Based on the measurements, the stopping cross section in the gas phase is about ∼50-70% higher than that in the solid phase. However, for the noble gases, the Van der Waals forces are too weak to effect the energy loss of ions [4]. Therefore, there is no significant difference between the stopping power in gas and solid phases for xenon. While both LS and BK theories over-predict the stopping power considerably, SRIM is not surprisingly much closer to the data. However, the energy dependence of the SRIM data is not totally consistent with the experiment. The data indicates a slightly faster fall off at lower energy than v, but not as faster as Tilinin's result, which seems to under-predict the electronic stopping power.

To make progress, we assume that in the energy region of our interest, the electronic stopping power drops with the same trend as that is measured at higher energy, with a power law behavior, E^α. We fit the power-law exponent and the coefficient to the lowest four measured points, and then extrapolate the result to the low-energy region. The best fit finds

$$S_e(E) = 1.906 \times E^{0.84}\ \text{MeV} \cdot \text{g}^{-1} \cdot \text{cm}^2\ . \tag{3.10}$$

The result is also shown in Fig. 3.1 as the black solid line, which lies in between Ziegler's result and Tilinin's in our concerned energy region. As an estimate of the uncertainty.

Since electronic stopping power is very important in the estimation of the electronic energy dissipation, we also try to determine a range of extrapolations defined by two boundary curves. To get the accurate boundary curves, we try the following two methods.

Method A, choose 2σ points and fit them. Below are the detailed steps:

- We randomly generate 10,000,000 numbers in the 2σ region for every selected point. For example, the experiment measured electronic stopping power for 44.22 keV Xenon in Xenon is 45.77 MeV$\cdot$g$^{-1}\cdot$cm^2 and the 2σ error is $\pm$1.84 MeV$\cdot$g$^{-1}\cdot$cm^2. We generate 10,000,000 random numbers between 45.77+1.84 and 45.77-1.84;
- We randomly pick out a value from the 10,000,000 random numbers for every experiment measured point, and form new data set.
- We fit the power law $S_e(E) = K \times E^N$ to the generate data set to obtain the parameter K and N;
- We repeat above steps for 1,000 times to get 1,000 expressions for electronic stopping power;
- We plot the 1,000 electronic stopping power expressions together to get the 2σ error band, which is shown in Fig. 3.3

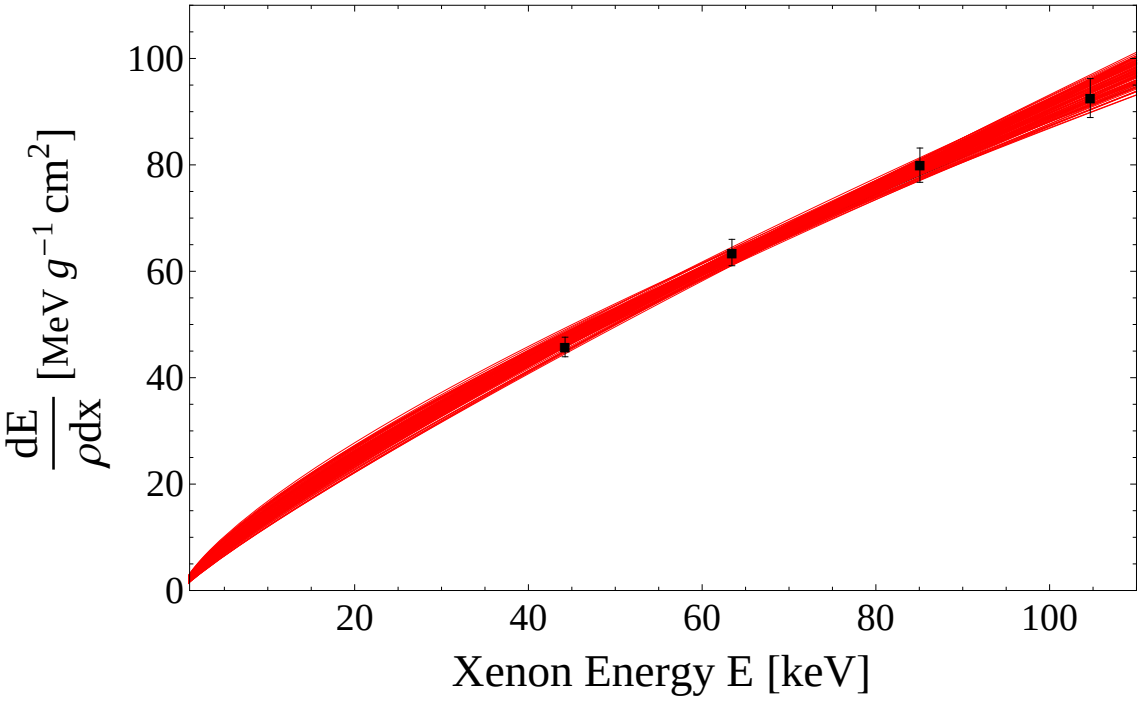

FIGURE 3.3: The red band is the 2σ error band generated and the black square points are experimental data with 2σ error.

Method B, using χ^2 distribution to fulfill uncertainties control. Below are the detailed steps:

- Based on our test and the theoretical prediction, the exponent N in the electronic stopping power expression should lie in between 0.5 and 1.5, and the coefficient K should lie in between 1 and 3, we randomly generate the 10,000,000 numbers between 0.5 and 1.5 to form data set for the N and randomly generate the 10,000,000 numbers between 1 and 3 to form data set for the K;

- We randomly pick out a set of value from the data set for N and K respectively to generate an expression for the electronic stopping power;

- We use Chi-square distribution to check whether the randomly generated electronic stopping power expression lies in the experiment measured 2σ region. If the Chi-square value is less than 4, we regard the expression lies in the experiment measured 2σ region and will keep it, or we will reject it. For example, generated electronic stopping power expression is $f(E)$ and the experimental data is $f_{\exp}(E)$. Then using the following condition to check whether the expression lies in the 2σ region:

$$\frac{1}{2}\sum_{i=1}^{4}\frac{(f(x_i)-f_{\exp}(x_i))^2}{\sigma_i^2}\leq 4\ , \tag{3.11}$$

  where the denominator 2 is the data point number minus free degree.

- We repeat above steps for 100,000 times and get more than 600 expressions for electronic stopping power. At the same time, we try to plot the distribution of K-N in Fig. 3.4.

- We plot the electronic stopping power expressions generated in step4 together to get the 2σ error band, which is shown in Fig. 3.5.

Additionally, we try to composite Fig. 3.3 and Fig. 3.5 together, we notice that the 2σ region generated using the two different method are almost the same, which is shown in Fig. 3.6

Based on above scenario:

- If we use the boundary of N to evaluate 2sigma region, we get $S_e^{'}(E) = 2.796 \times E^{0.75}$ for upper boundary and $S_e^{''}(E) = 1.518 \times E^{0.89}$ for lower boundary;

- If we use the envelop of the 2sigma region to evaluate the 2sigma error, we get $S_e^{'}(E) = 2.729 \times E^{0.77}$ upper boundary and $S_e^{''}(E) = 1.551 \times E^{0.87}$ for lower boundary;

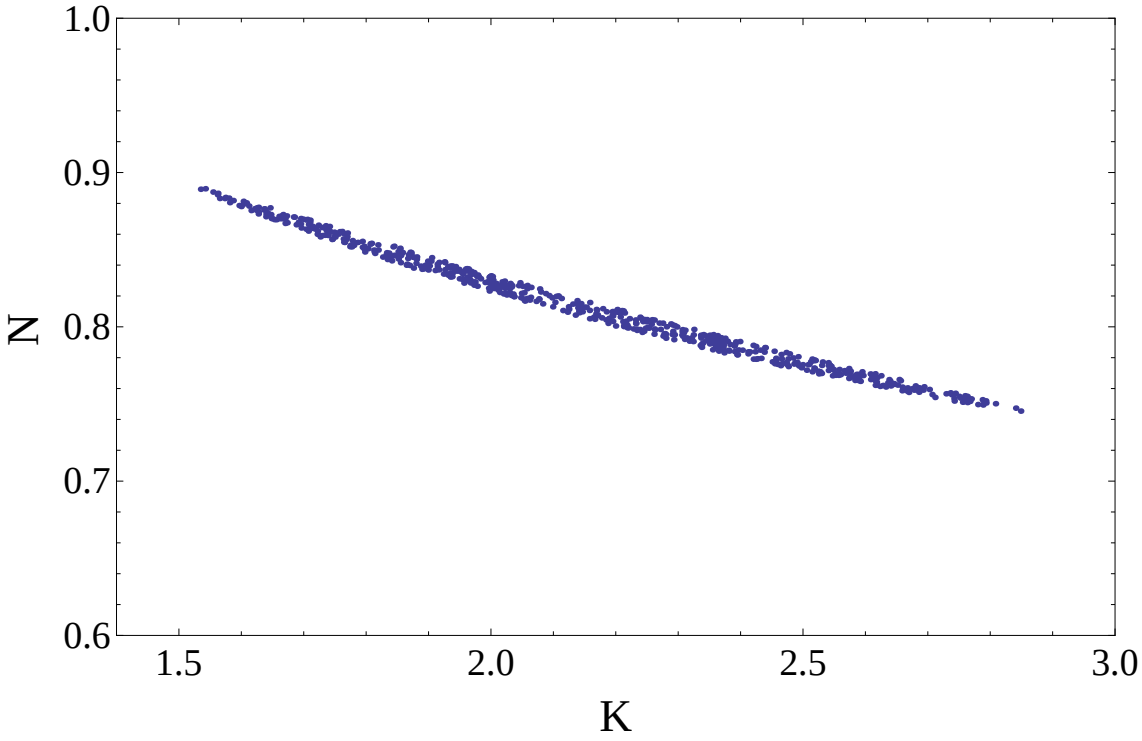

FIGURE 3.4: K-N distribution which can satisfy the 2σ error band.

The 2σ bound is shown as the yellow region in Fig. 3.1. In this thesis, we perform simulations using the above fits, and estimate one of the systematic uncertainties using the 2σ bound of the stopping power.

Finally, we note that for the particle energy drops below the band gap in liquid xenon, $S(E)$ shall be identically zero. We could have imposed this condition on the fit. As described before, we will implement this condition through the nature cutoff in Monte Carlo simulation in calculating the total nuclear quenching.

3.4 Electronic Energy Dissipation and Nuclear Quenching Factor

Once we have the electronic stopping power and the trajectory of the recoiling nucleus, we can compute the electronic energy loss in one nuclear binary collision by integrating the stopping power over the free flight path. And summarizing the electronic energy losses, we can get the total electronic energy loss $\eta(E_0)$ in the collision cascade.

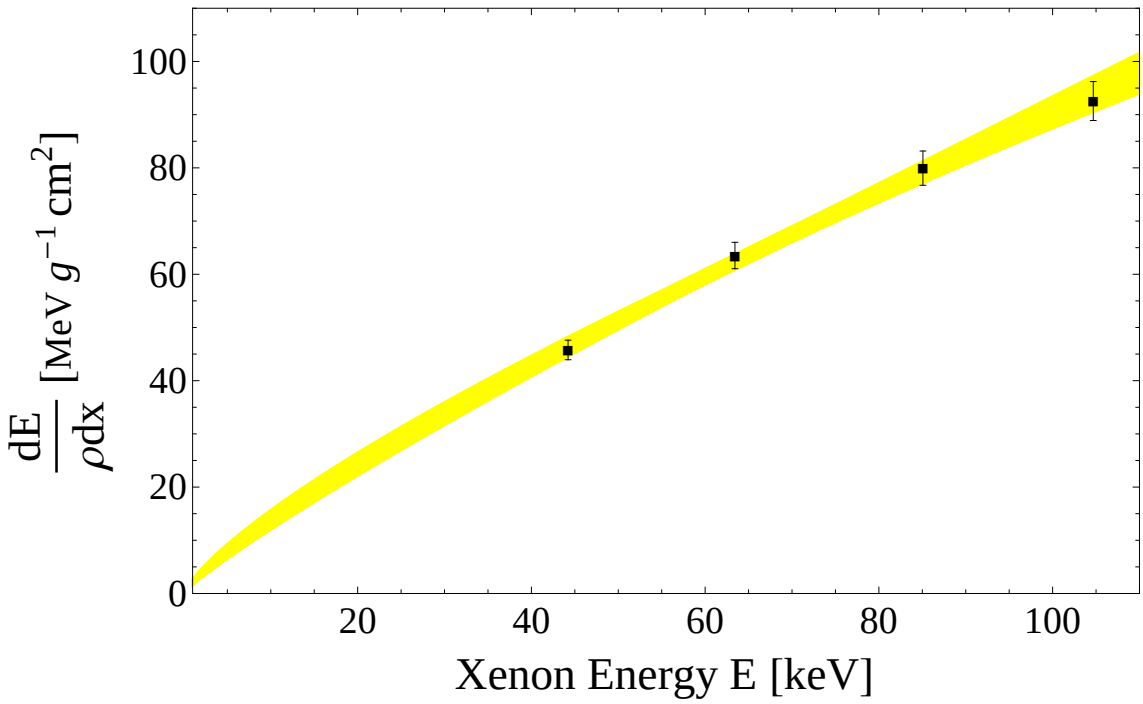

FIGURE 3.5: The yellow band is the 2σ generated and the black square points are experimental data with 2σ error.

Using the above result, we calculate $q_{\rm nc}$ through Monte Carlo simulations. Through 10,000 scattering events, we get a fair average for a discrete set of energies range 0.5∼25 keV, which has a phenomenological fit:

$$q_{\rm nc}(E_{\rm nr}) = \frac{e^{-0.033E_{\rm nr}^{-0.958}}}{1 + 13.789E_{\rm nr}^{-0.189}} \ . \tag{3.12}$$

We plot it in Fig. 3.7 as the black solid line. We have also shown the 2σ band calculated with the 2σ fit of the electronis stopping power. To calibrate our code, we perform simulations using the SRIM electronic stopping power with TRIM parameters in attempt to reproduce the TRIM results. We plot the original TRIM result as the green dashed curve and our reproduction in purple dashed curve. The small difference is due to using of realistic atomic distribution in LXe. We also plot the widely used Lindhard factor [48–50] as the blue dashed curve for comparison, using the most quoted $k = 0.166$. Our $q_{\rm nc}$ is smaller, but not that much smaller, than the quoted Lindhard factor and the TRIM result although the corresponding electronic stopping powers are much bigger. This is because the integral equation approach is questionable at low energy, whereas TRIM uses an artificial (or equivalent) cut-off energy beyond which all atom kinetic energy goes to heat. The important feature of our result is that $q_{\rm nc}$ is smaller than $\mathcal{L}_{\rm eff}$, consistent with the phenomenological observation that the

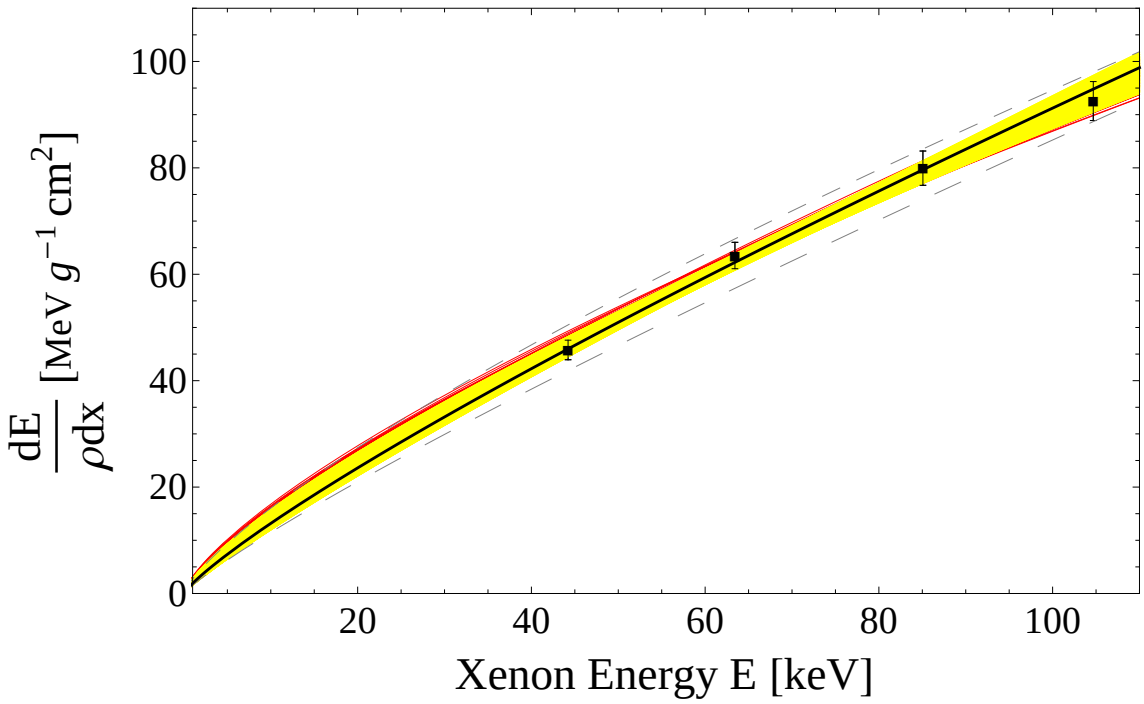

FIGURE 3.6: The gray dashed line bound the 2σ error region.

scintillation efficiency for nuclear recoils is larger than that of the electron recoils.

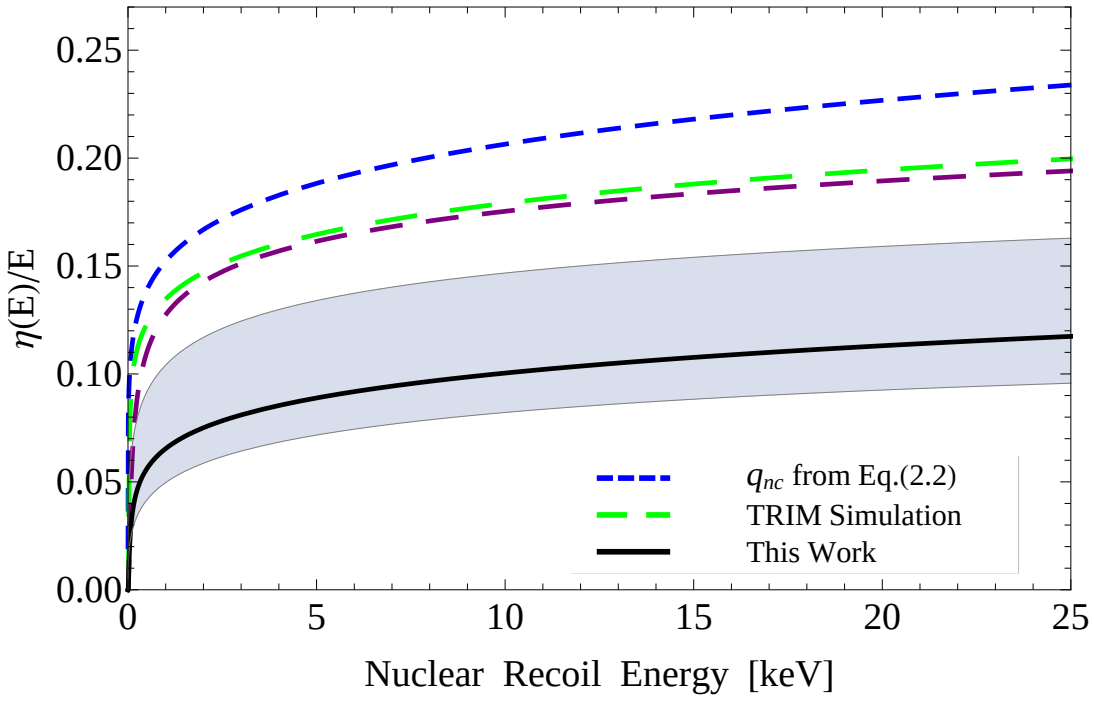

FIGURE 3.7: The $q_{\rm nc}$, of liquid xenon obtained from different theoretical predictions. The lower black solid curve and shade is the result from our calculation by using the electronic stopping power fitted to the available experimental measured data.

Chapter 4

Recombination of Electron-Ion Pairs in Liquid Xenon Detector

Since we can estimate the equivalent electronic energy dissipation for nuclear recoils from the simulation and the electronic stopping power for liquid xenon, it is time for us to do more research about the scintillation and ionization process to evaluate how much S1 or S2 signals produced from nuclear recoils.

In this Chapter, we firstly review the scintillation and ionization process. We then study the anti-correlation behavior between the scintillation signals and the ionization signals to find out which factor determines the electron-ion pair's recombination. After that, we perform further research on the recombination behavior of the electron-ion pairs with or without applied electric field. Finally, we generalize the Thomas-Imel box model to describe this behavior.

4.1 Scintillation and Ionization Process

4.1.1 Excitons, Charges and Platzman Equation

For any particle moving in a medium, after all the particles have thermalized, a certain number of excitons and electron-ion pairs will be produced in the collision cascade process. In 1961, Platzman proposed an equation based on the energy conservation law to describe this process, which is called Platzman equation [70]. Platzman assumes the total dissipated

electronic energy can be divided into three parts: ionization, excitation and sub-excitation electrons:

$$E^{ee} = N_i E_i + N_{ex} E_{ex} + N_i \epsilon \ , \tag{4.1}$$

where E^{ee} is the electronic energy dissipation, N_i is the number of electron-ion pairs produced at an average energy expenditure of E_i, and N_{ex} is the number of excitons at an average energy expenditure of E_{ex}. ϵ is the average kinetic energy of sub-excitation electrons, in fact which can be absorbed into E_{ex} and E_i.

This equation is firstly proposed for high energy radiation. In the original paper, Platzman only gave a rough approximation for the parameters such as E_{ex}, E_i, and others. As the development of the technology, the value E_{ex} and E_i can be measured pretty good, which we will discuss in the following sections. However, the values for N_{ex} and N_i are still controversial. Regarding N_{ex}/N_i, Some authors regard 0.06 the theoretical value [71] and 0.2 the measured one [72] for electron recoils while in Ref. [32, 73], $N_{ex}/N_i \sim 1$ is claimed for nuclear recoils from the direct charge measurement. But these values are fitted to the data based on much larger $q_{\rm nc}$ in Ref. [48–50], which is inconsistent with the requirement $q_{nc} \leq \mathcal{L}_{\rm eff}$ (we will discuss in the next Chapter). However, the main stream view about N_{ex}/N_i is that it is independent of whether the electromagnetic energy is from electron or nuclear recoils [72]. Of course, there is no strong evidence for or against this assumption. Most measurements were done with electron recoils, yielding a small N_{ex}/N_i value, 0.06 to 0.2. Measurements done with nuclear recoils depends on the nuclear quenching factor and recombination model. In Ref. [73], the value about 1 was obtained if using larger nuclear quenching factor. However, as we advocated in this thesis, the realistic nuclear quenching factor should be about a factor of 2 smaller than the Lindhard's. Thus N_{ex}/N_i in the recoils can be made consistent with that in the electron recoil.

Ideally, every exciton is expected to produce one photon and every electron will drift to gas chamber and give out a free electron, where the process can be describe as: After the excitons relax, the lowest ${}^3\Sigma_u^+$ and ${}^1\Sigma_u^+$ self-trapped excitonic molecular states, Xe_2^*, get formed. Then they scintillate in VUV region through the transition to the ground state ${}^1\Sigma_g^+$ and give out S1 signal. On the other hand, forced by the external field, the free electrons can drift to the gas mode and give out S2 signal. However, the real world is not so perfect that the free electrons and ions will unavoidably recombine with each other, even under high external electric field.

The whole process can be described phenomenologically by the following equations [32]:

$$\begin{aligned} &\mathrm{Xe}^{+} + \mathrm{Xe} \rightarrow \mathrm{Xe}_2^{+}, \\ &\mathrm{Xe}_2^{+} + \mathrm{e}^{-} \rightarrow \mathrm{Xe}^{**} + \mathrm{Xe}, \\ &\mathrm{Xe}^{**} \rightarrow \mathrm{Xe}^{*} + \mathrm{heat} \\ &\mathrm{Xe}^{*} + \mathrm{Xe} + \mathrm{Xe} \rightarrow \mathrm{Xe}_2^{*} + \mathrm{Xe}, \\ &\mathrm{Xe}_2^{*} \rightarrow \mathrm{Xe} + \mathrm{Xe} + \mathrm{h}\nu \end{aligned} \tag{4.2}$$

In this case, there should be an anti-correlation relation between the S1 ans S2 signles.

4.1.2 Anti-correlation Behavior between S1 and S2

It seems that one can easily get the number for the photons or charges after the parameters in Platzman equation are identified or measured. However, it is more complicated than what one expects. After the particles are thermalized in the medium, the produced electrons released from xenon atoms in ionization events undergo a random motion under the influence of mutual electrostatic interactions. Part of the oppositely charged particles (electrons and ions) approach the others to a short distance and finally recombine which results in reduction of the ionization yield. In the presence of an external electric field, more of the pairs are permanently separated and more electrons are expected to escape from recombination as the electric field increases. However, both the electron-ion recombination and the electron escaping from the recombination exist at any finite field strength. Due to both behaviors exist coinstantaneously, the S1 signal will be enhanced when the applied electric field is week and the S2 signal will be suppressed while the recombination is strengthened. On the other hand, the S2 signal will increase when the applied electric field is strong and more electrons escape from the recombination while the S1 signals will get weakened. This is the so-called anti-correlation between S1 and S2, which refers to the phenomenon that the ionized electrons escape recombination with positive ones (Xe_2^+), thereby reducing the scintillation photons.

Thus the scintillation and ionization signals are correlated to each other, which makes the problem much more complex. That the ionization and scintillation signals in LXe are anti-correlated is studied and examined in Ref. [74] firstly and discussed further in Ref. [75]. The anti-correlation refers to the phenomenon that the ionized electrons escape recombination with positive ones (Xe_2^+), thereby reducing the scintillation photons. To know the exact

scintillant and ionization signals, we have to do more research on the recombination behavior of electron-ion pairs.

4.2 Theoretical Consideration of Recombination of Electron-Ion Pairs

To accurately estimate the yields of S1 and S2 signals respectively, the correct interpretation of data obtained from LXe detectors requires good understanding of the recombination processes in this medium. In fact, the physics of electron-ion pair's recombination in liquid xenon is not well understood yet. Phenomenologically speaking, three kinds of recombination may occur in LXe detector:

- Initial recombination, which refers to the process where an electron, freed from an atom and thus producing a positive ion, returns to its origin and recombines to produce a neutral atom again. Under no external electric field scenario, this mechanism is presumed to be the leading of the recombination of most pairs;
- Bulk recombination, which occurs when there are a continuum of charges of both electrons and ions presenting at the same location. A random electron combines with a random positive ion at a rate proportional to the densities of the electron and ion;
- Columnar recombination, which occurs when an energetic charged particle produces a column of ion pairs in an external electric field. As the electrons drift in one direction and the positive ions in the other, electrons and ions occasionally recombine.

Once we know something about the electron-ion recombination, we can perform a theoretical consideration to evaluate the process. From the phenomenological consideration of electron-ion recombination, a large number of theoretical studies [76–82] have been made for over a century. Among these, Thomas and Imel gave a detailed analytical expression in Ref. [80] after considering the recombination behavior for electron recoils or alpha recoils in liquid xenon.

4.2.1 Thomas-Imel Model for Electron Recoil

Thomas and Imel started from the diffusion equations for positive ion (n^+) and electrons (n^-) proposed by Jaffe in Ref. [78]:

$$\begin{aligned} \partial_t n_i^+ &= -\mu_+ \vec{E}_d \cdot \nabla n_i^+ + d_+ \nabla^2 n_i^+ - \alpha n_i^- n_i^+ \ , \\ \partial_t n_i^- &= -\mu_- \vec{E}_d \cdot \nabla n_i^- + d_- \nabla^2 n_i^- - \alpha n_i^+ n_i^- \ , \end{aligned} \tag{4.3}$$

where $\mu_\pm$ is the mean mobilities of the ions and electrons under external electric field, while $d_\pm$ and α are coefficients corresponding to the diffusion and recombination terms. To simplify the equations, they ignored the diffusion terms, which are considered to be much smaller than the electron drift, and also dropped the drift terms of the positive ion. Solving the equations in the box boundary conditions, Thomas and Imel obtained the following result:

$$\frac{Q}{Q_0} = \frac{N_i^{\rm esc}}{N_i} = \frac{1}{\xi}\ln(1+\xi); \qquad \xi = \frac{n_i \alpha}{4a^2 \mu_- E_d} \ , \tag{4.4}$$

where $\alpha/(4a^2\mu_-)$ is a constant determined by the dielectric constant, the electron mobility and the ionization volume length scale. The diffusion processes are neglected in case of a large external electric field because the diffusion speeds of electric charges are negligible compared to their drift speeds in the electric field. However, to get more reliable results at smaller electric field, we have to consider the electron mobility terms $\mu_- E_d$ in ξ.

Eq. (4.4) gives a pretty good expression for the electic field dependence of electron-ion recombination in liquid xenon. However, this equation ignores the drift velocity of the electrons in liquid xenon. In liquid xenon, when electrons are excited to the conduction band from the valence band by an energetic radiation, they become free electrons and drift in external electric field. At low fields, the electron drift velocity, v_d, is almost proportional to the field strength, E_d, with the electron mobility, μ, as the proportionality constant ($v_d = \mu E_d$). At high fields, about 10 kV/cm in liquid xenon [83], the electron drift velocity saturates and becomes independent of electric field strength. However, at low field, we shall consider the random fluctuations of electric fields acting on the free electrons. This electric fields cause the free electrons to diffuse out of the positive ion region with an average speed v_0, which means some electrons may escape from recombination even when no external field is applied. Additionally, using the electronic stopping power or LET as a rough estimation of the charge

density, we can generalize ξ as:

$$\xi = \frac{n_i \alpha}{4a^2(\beta v_0 + v_d)} \equiv \frac{K_1}{1 + K_2 \times E_d} \left(\frac{dE}{dx}\right)_{\text{el}} , \tag{4.5}$$

where β is some unknown constant.

Considering K_1 a field-independent parameter and fitted to experimentally measured LET dependence of the scintillation yields in liquid xenon [84], we get $K_1 = 2.53$ MeV^{-1}·g·cm^{-2}. Then, we fit K_2 to the experimental data for electron recoils and alphas in Ref. [2], and find $K_2 = 3$ KV^{-1}·cm. Here we do not try to re-calculate Q/Q_0 in Ref. [2] for the ionization yield when fitting the parameter K_2 since we just want to check if the generalized Thomas-Imel model can obtain the recombination trend accurately.

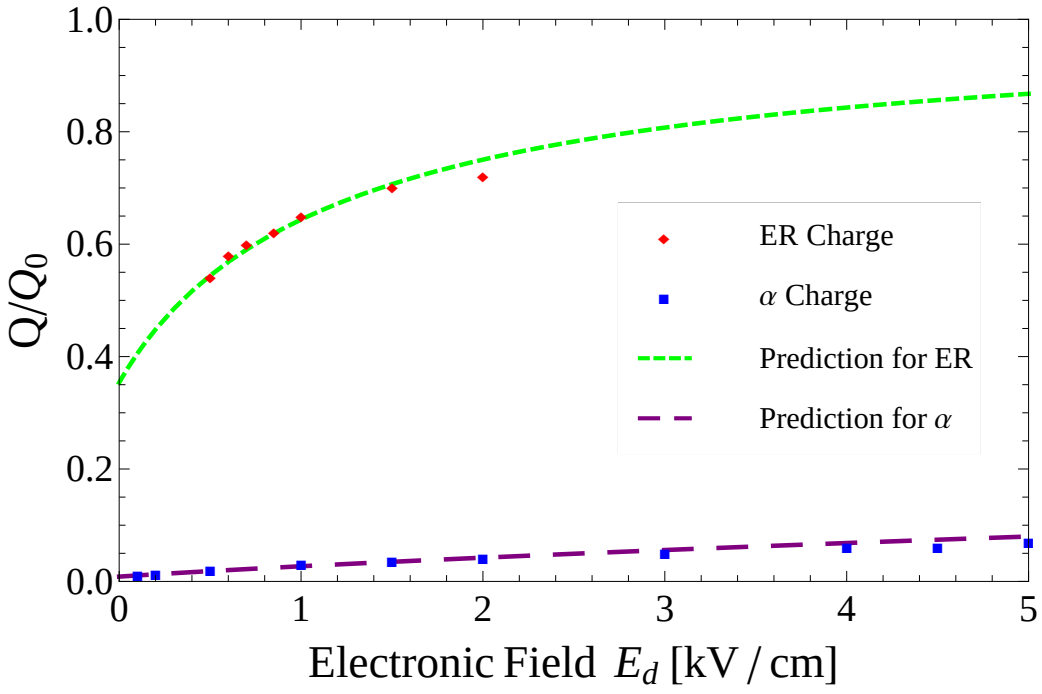

FIGURE 4.1: Reproduction of field dependence of ionization yield efficiency in LXe for 122 keV electron recoils (ER) and 5.5 MeV alphas. The data is extracted from Fig. 3 in Ref. [2].

Both electron recoils, which have lower LET value and suffer less recombination, and alphas, which have higher LET value and suffer more recombination, have clear field dependence shown Fig. 4.1. Thomas-Imel box model successfully reproduces the field dependence. It yields the recombination probability as a function of the ionization density and the external electric field, where a smaller number of escaping electrons are produced along a denser

track (higher LET), at the same time, the number of escaping electrons increases with the increasing of the applied electric field.

4.2.2 Generalization of Thomas-Imel Model to Nuclear Recoils

When it comes to nuclear recoils, the electric field dependence is quite different. The ionization density dependence of recombination still exists, however no significant field dependence of recombination has been measured [2]. There must be some unidentified physics effect, except for the different LET values, which may interfere the recombination behavior of nuclear recoils and has not been covered in original Thomas-Imel box model. Chepel *et al.* analyzed the track structures for electronic recoils and alphas recoils [85]. The tracks of electron recoils (with low LET) can be regarded as a line of widely populated positive ions with average distance close to the Onsager radius. The free electrons reach thermal energy at sufficiently large distances from the track escape from recombination, causing the increase of ionization yield for electron recoils in external electric field. For alphas (high LET), the track structure is a little different, which can be described as concentric cylinders consisting of a central core and a surrounding penumbra [48]. A continuous line of positive charges forms the core of the main trajectory. Compared with electron recoils, the charge density is much higher. However, both electron recoils and alphas have a line-like or column-like track structure, though the charge density along the trajectory is different.

For nuclear recoils, it is a totally different physical picture. Although the track structure of nuclear recoils is not fully understand, it is clear that nuclear recoils will cause a large number of secondary nuclear recoils through binary collisions during the slowing down process, which results in a tree-like track structure, where lots of secondary trajectories are surrounding the main trajectory. This behavior has been proved by computer simulations [4, 86]. The secondary trajectories enlarge the spatial distribution of the ions projecting to the main trajectory. Although the electric charges in the secondary trajectory is sparse, they screen the applied electric field significantly, which in some sense is similar to the electrostatic screening effect. It is reasonable to surmise that the screen effect can explain why the recombination for nuclear recoils depends weakly on external electric field. The significantly-varied physics pictures for different radiation particles hinder the development of a universal theory of recombination in LXe detector. Existing recombination models mainly consider the column-like or line-like radiation track structures, ignoring the specific track structure of

nuclear recoils. It is not surprising that existing recombination models cannot quantitatively explain the field dependence of recombination for nuclear recoils. To get more solid and reliable prediction, we have to extend the existing models.

Here, we generalize Thomas-Imel box model starting from the box boundary condition. The box boundary condition assumes both electrons and ions are distributed in a certain volume and model their evolution due to the charge drift and reactions. This model well covers the cylindrically symmetric distributions of electrons and ions along the trajectory of electron recoils and alphas, which have column-like structures. But for nuclear recoils, the tree-like track structure breaks the field dependence relation. The neglecting of the geometry of the secondary trajectories distribution for nuclear recoils causes the model fail to predict the recombination rate for nuclear recoils. Based on this, we can generalize Thomas-Imel box model by introducing a field-screen degree S in ξ to correct the electric field dependence:

$$\xi = \frac{K_1}{1 + K_2 \times E_d^{1/S}} \left(\frac{dE}{dx}\right)_{\text{el}} \tag{4.6}$$

where the screen exponent S is assumed to be proportional to the spatial distribution scale of the track structure. Since the Bohr impulse principle, normally used to assess the radiation core radius, is not applicable for nuclear recoils, we have to find another physical quantity to evaluate the scale of the nuclear recoils' track in this article. As we know, the secondary trajectories are caused by binary nuclear recoils, where nuclear stopping power (the energy loss to nuclei per unit path $(dE/dx)_{\text{ncl}}$), is a useful physical quantity to describe the nuclear collision. So we may relate S to $(dE/dx)_{\text{ncl}}$ through $S = K_3 \times (dE/dx)_{\text{ncl}}$. Finally, we obtain the generalized Thomas-Imel equation for nuclear recoils:

$$\frac{Q}{Q_0} = \frac{N_i^{\text{esc}}}{N_i} = \frac{1}{\xi}\ln(1+\xi); \qquad \xi = \frac{K_1}{1 + K_2 \times E_d^{1/(K_3 \times (dE/dx)_{\text{ncl}})}} \left(\frac{dE}{dx}\right)_{\text{el}}, \tag{4.7}$$

Fitting to experimental data, we can identify the free parameters K_1, K_2 and K_3, which we will discuss in the next Chapter.

Chapter 5

Scintillation Efficiency and Ionization Yield of Liquid Xenon for Low Energy Nuclear Recoils

Now we have the program to simulate the slowing down process of the recoiling nucleus and the electronic stopping power, which help us to evaluate the electronic energy dissipation $\eta(E_{\rm nr})$ and nuclear quenching factor $q_{\rm nc}$ during the slowing down process. We also have the theoretical model to estimate how much scintillation or ionization signals produces from the electronic energy dissipation. Combining all above, we can predict the relative scintillation efficiency $\mathcal{L}_{\rm eff}$ and ionization yield $\mathcal{Q}_{\rm y}$.

In this Chapter, we will show how to combine the nuclear quenching factor and the recombination model to get scintillation efficiency and the ionization yield for nuclear recoils in WIMP dark matter direct detection. At last, we discuss how to improve the calculation in the future.

5.1 Relative Scintillation Efficiency of Low Energy Nuclear Recoils in Liquid Xenon

As mentioned in Chapter 4, not all electronic excitations or electron-ion pairs will generate scintillation through the exciton de-excitation and electron-ion pair recombination. Some

quenching effects, such as electrons' escaping from electron-ion pair recombination and the collision loss at high ionization density as described in Birk's law will reduce the scintillation yield and must be considered when calculating the final scintillation efficiency. In other words, only part of electronic energy loss is transferred to measurable scintillation (S1) signal. Here, at low recoiling energy, the electrons escaping from electron-ion pair recombination is the main quenching effect, which can be described using the generalized Thomas-Imel Model. In this section, we will show how to get the free parameters in the model and show the predicted relative scintillation efficiency $\mathcal{L}_{\text{eff}}$.

We denote the effect of electron escaping from recombination, which reduces the scintillation yield, as q_{sc} in the following context. This effect has been measured experimentally as a function of electronic stopping power or LET. Combining with the electronic energy dissipation $\eta(E_{\text{nr}})$, the total scintillation efficiency of the nuclear recoil can finally be described by,

$$q(E_{\text{nr}}) = \frac{\eta_{\text{sc}}(E_{\text{nr}})}{E_0} = \frac{\eta(E_{\text{nr}})q_{\text{sc}}(E_{\text{nr}})}{E_{\text{nr}}} \ . \tag{5.1}$$

Obviously, the quenching effect also exists for the electron recoils from gamma rays, which must be taken into account when calculating the relative scintillation efficiency.

Since scintillation efficiency is measured at external zero field, the parameters K_2 and K_3 in Eq. (4.7) do not matter. If we consider the parameter K_1 as an electric field independent parameter, we can firstly identify the parameter K_1. The parameter K_1 can be obtained phenomenological from the LET dependence of the relative scintillation yields in liquid xenon. Thus the quenching effect due to electrons escaping can be expressed as:

$$q_{\text{sc}} = \frac{r + N_{ex}/N_i}{1 + N_{ex}/N_i} = \frac{1}{1 + N_{ex}/N_i}\left(1 - \frac{\ln(1 + K_1\frac{dE}{dx})}{K_1\frac{dE}{dx}} + \frac{N_{ex}}{N_i}\right) \tag{5.2}$$

where again N_{ex}/N_i and K_1 can be determined from experimental data.

When investigating the scintillation yields in liquid xenon, Tanaka *et al.* find that the scintillation yields depends on LET in Ref. [84]. From the result of a series scintillation yield measurements using heavy ion beam, they have obtained LET dependence of the relative scintillation yields in liquid xenon for relativistic heavy ions, using alpha particles as a standard for scintillation yield. Additionally, Doke *et al.* go further to measure the absolute scintillation yields in liquid argon and xenon for various particles [72], the results also shows the similar dependence relation between the scintillation yields and the LET. Their work can

help us find out the free parameters and exam the reliability of the theoretical model. Based on above works, we try to find the two parameters K and N_{ex}/N_i from the LET dependence of scintillation yields in liquid xenon firstly. To fit the model to experimental data, we start from the observable quantity N_{ex}/N_i. Many authors have discussed this value either theoretically or experimentally [32, 71, 72]. In Ref. [71], the authors give a theoretical prediction as $N_{ex}/N_i = 0.06$, which is the known minimum value for N_{ex}/N_i, while in Ref. [72], the authors provide an experimental measured value as $N_{ex}/N_i = 0.20$. Additionally, the XENON10 collaboration, fitting their calculation on nuclear quenching to experimental data, proposes the value as $N_{ex}/N_i = 1.09$ [73], which is the known maximum value for N_{ex}/N_i,. It is reasonable to surmise that the value 0.06 gives the lower limit and 1.09 the upper limit while 0.20 the possible compromise. We use these three values to separately fit the free parameter K to the experimental measured data in Ref. [72] as: $K = 3.25$ MeV^{-1}·g·cm^{-2} for $N_{ex}/N_i = 0.06$; $K = 2.53$ MeV^{-1}·g·cm^{-2} for $N_{ex}/N_i = 0.20$ and $K = 0.50$ MeV^{-1}·g·cm^{-2} for $N_{ex}/N_i = 1.09$.

Based on the three sets of free parameters, we show in Fig. 5.1 the LET dependence of the relative xenon scintillation yields to electronic recoils at 122 keV respectively. The shaded region correspond to the xenon LET with the kinetic energy of the xenon atom ranging from 0.5 keV to 25 keV. We can see the result from the parameter set $K = 0.50$ MeV^{-1}·g·cm^{-2} and $N_{ex}/N_i = 1.09$ deviates from the experimental measured data in Ref. [72] a little in very low LET region. However, in the region of our interest, the relative scintillation efficiency depends little on the sets of parameters. In this thesis, we will take this empirical result fitted to the experimental scintillation quenching as our input.

Finally, we can get the result for $\mathcal{L}_{\text{eff}}$, we have to convert the electronic excitation energy into scintillation energy using the scintillation quenching factor discussed in the previous section. The quenching efficiency depends on the LET and hence is in principle different in different stages of the cascade. However, it turns out that the effect of this LET dependence is small, one can just use the LET of the initial recoil energy to calculate the total scintillation without making a significant difference. Since the relative scintillation from the electron escaping model is weekly dependent on the free parameters, we will use the central values $K = 2.53$ MeV^{-1}·g·cm^{-2} and $N_{ex}/N_i = 0.20$ in the following consideration.

Based on above consideration, the final result for $\mathcal{L}_{\text{eff}}$ is shown as the solid line in Fig. 5.2, where we have taken into account the relative scintillation to 122 keV γ ray. The result can

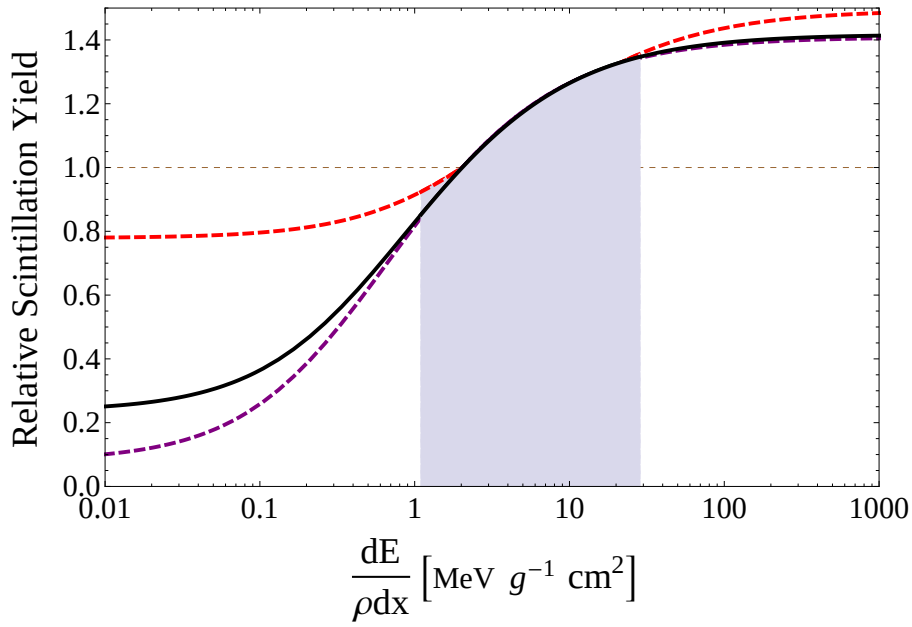

FIGURE 5.1: LET dependence of the relative scintillation yields to electronic recoils at 122 keV in liquid xenon from Thomas-Imel model. The black solid curve, which we consider as the best fit, corresponds to the free parameters set to $K = 2.53$ MeV^{-1}·g·cm^{-2} and $N_{ex}/N_i = 0.20$. The purple dashed curve is plotted when the parameters are set to $K = 3.25$ MeV^{-1}·g·cm^{-2} and $N_{ex}/N_i = 0.06$ while the red dashed curve $K = 0.50$ MeV^{-1}·g·cm^{-2} and $N_{ex}/N_i = 1.09$. The shaded region corresponds to the interest of direct DM detection (LET for 0.5 keV to 25 keV nuclear recoils energy).

be phenomenologically expressed as,

$$\mathcal{L}_{\rm eff}(E_{\rm nr}) = q_{\rm nc}(E_{\rm nr}) \times (1.417 - 0.245\ln(1 + 4.822E_{\rm nr}^{0.840})E_{\rm nr}^{-0.840})\cdot \tag{5.3}$$

The error band includes both the systematic 2σ uncertainty from the electronic stopping power fit and from the statistical error in the simulation. Along with our calculation, we have also shown the experimental data from different measurements. The blue squares are the result from the Columbia group measurement [38]. The magenta dots are from the Yale group measurement [19]. The purple stars and the orange diamonds are from the XENON100 collaboration with mono-energy neutron and broad spectrum neutron sources, respectively [39, 46]. The theoretical result compares very well with the experimental data (maybe too well?), although one has to keep in mind this is not a complete *ab initio* computation. The most important message of our calculation, however, is that the scintillation efficiency rapidly decreases with decreasing energy, particularly when less than 3 keV, and goes to zero as the energy goes to zero. This result is expected to be of more general validity because as the recoil energy becomes small, the atom loses its kinetic energy mainly through elastic

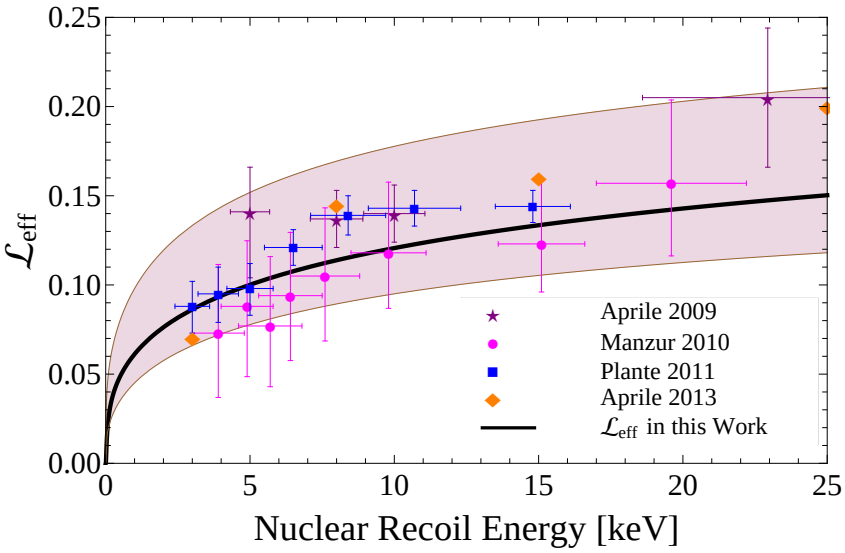

FIGURE 5.2: The relative scintillation efficiency $\mathcal{L}_{\rm eff}$ obtained from our calculation, compared with the available experimental data. Here, we use the nuclear quenching calculated by using electronic stopping power $S_e(E) = 1.906 \times E^{0.84}$ and the scintillation quenching obtained using the parameters $K = 2.53$ MeV^{-1}·g·cm^{-2} and $N_{ex}/N_i = 0.20$. The shaded band shows the system and statistical uncertainties with $\pm 2\sigma$. It is seen that $\mathcal{L}_{\rm eff}$ drops off very quickly when the recoil energy is below 3 keV.

scattering with other atoms, rather than generate electronic excitations. This behavior has in some sense already encoded in the electronic stopping power.

5.2 Ionization Yield from Nuclear Recoils in Liquid Xenon

5.2.1 Average Energy Required to Produce One Electron-Ion pair

It is a little complicated to derive the ionization yield $\mathcal{Q}_{\rm y}$ even after we have know the electronic energy dissipation $\eta(E_{\rm nr})$, because we have to know average energy required to produce one electron-ion pair, which is also called W-value.

Since the Platzman equation Eq. (4.1) only gives rise to a phenomenological expression for the W-value, we have to identify the W-value relying on experimental measurements. Experimentally, W-value for ionization have been measured in liquid xenon by several groups [3, 71, 87–91] over the past forty years. The authors use α sources, γ-rays, X-rays or monoenergetic electrons sources respectively and get quite different W-values for liquid xenon, which are listed in Table (5.1). It is not surprising that the literature values of W are scattered in these measurements since absolute charge measurements are inherently challenging.

Firstly, it is very difficult to identify the exact energy dissipation of the radiations precisely. Due to this reason, high linear energy transfer (LET) and low-energy radiations will be the good sources. Secondly, the electron-ion recombination exists, even for large drift electric fields, therefore it is hard to identify what fraction of generated electrons are collected. Because of that, one has to choose some low LET radiations as the sources and apply recombination theory to estimate the recombination rate, where the "experimental result" would depend also on which recombination theory is used.

Radiation Source	W-value (eV)	Year	Reference
X-Ray	7.3	1973	Robinson and Freeman [87]
^{210}Po	17.3	1973	Kinno and Kobayashi [88]
^{63}Ni	16.5±1.4	1974	Takahashi *et al* [89]
^{207}Bi	15.6±0.3	1975	Takahashi *et al* [71]
X-Ray	15.2	1977	Huang and Freeman [90]
^{207}Bi	15.1±1.79	1991	Aprile *et al* [91]
Electron beams	9.76±0.70	1992	Seguinot *et al* [3]

TABLE 5.1: The W-value in liquid xenon from different experiment measurements

Based on above discussion, we believe the low-energy electron beams are the better radiation sources to measure the W-value and we examine two individual experimental measurements from Takahashi et al. [71] and Seguinot et al. [3], both of which use electron sources. In 1975, Takahashi *et al.* use an internal-conversion electron source (1 MeV) to produce electron pulses in liquid xenon and compare the signal with a 5.5 MeV α particles signal in an argon-methane (5%) gas mixture, whose W-value is known [71]. Using the relative pulse heights for the two materials, the authors obtain the W-value in liquid xenon as $W = 15.6\pm0.3$ eV, where the ratio of the W-value to the band gap energy, E_g, of liquid xenon (9.3 eV) is 1.68. In 1992, Seguinot *et al.* use mono-energetic electron beams (∼100 keV) through a 12 μm thick foil of Mylar to ionize and excite liquid xenon [3]. In this experiment, MeV's to GeV's energies are deposited in a liquid xenon test cell. In the meantime, the authors also performed measurements using both fixed energy deposition with variable applied electric fields as well as fixed applied electric fields with variable energy deposition to check the impact from electron-ion recombination. Then the authors apply Jaffe-like formula and Thomas-Imel formula to estimate the recombination of electron-ion pairs. The W-value they get is much lower than previous measurements where $W = 1.05E_g = 9.76\pm0.70$ eV, which is just slightly higher than the band gap energy of liquid xenon. Seguinot's result has been disputed in Ref. [92, 93]. However, Seguinot *et al.* claim that their measurement is accurate for low-energy electron excitation of liquid xenon.

Takahashi *et al.* uses Platzman's phenomenological theory to explain their results: set $E_i = 1.13E_g$ implicitly and $N_{ex}/N_i = 0.06$ theoretically; calculate the ϵ using Shockley's model as $\epsilon = 0.48E_g$. Then they get the theoretical prediction for W-value as $1.66E_g$ which is consistent with their experimental value ($1.68E_g$). Seguinot *et al.* did not give a theoretical explanation for their results in their publishing. However, it appears that if one ignores the sub-excitation electrons in Eq. (4.1), and then set $E_i = E_g$ and $N_{ex}/N_i = 0.06$ (theoretical value in Ref. [71]) or $N_{ex}/N_i = 0.20$ (experimental value in Ref. [72]), we can get a theoretical prediction for W-value between $1.05E_g$ and $1.18E_g$ which agrees reasonable well with Seguinot's experimental value ($1.05E_g$).

Although, Takahashi's measurement is widely quoted, we suspect that Seguinot's measurement may be more reasonable for low energy electron recoils and nuclear recoils in the WIMPs energy range. The kinetic energy for the sub-excitation electrons, ϵ in Eq. (4.1), comes from the binary collision between an incident particle and a free (ionized) electron of the media. For low energy electron recoils or nuclear recoils, few electronic energy dissipated as kinetic energy of sub-excitation electrons compared with that from high-energy particle recoils, because the energy transferred to the free (ionized) electrons through binary collision between the incident nucleus (or low energy electron) and the ionized electrons is negligible ($\sim \mathrm{m_{el}/m_{ncl}}$) (or small). Therefore, the electronic energy dissipations may mainly produce electron ionization or excitation. Additionally, the sub-excitation electrons are unobservable through experiment while E_g, E_{ex} and N_{ex}/N_i are well measured or calculated and identified by different experiments or theories. Therefore, we choose to adopt Seguinot's measurement for W-value 9.76 eV in the following sections.

5.2.2 Ionization Yield $\mathcal{Q}_{\mathrm{y}}$

When know the W-value, we can use the generalized Thomas-Imel model to predict the field and energy dependence of the ionization efficiency, $r = Q/Q_0$, taking into account the effects of the ionization density and track structure of nuclear recoils. Consequently we find the ionization yield,

$$\mathcal{Q}_{\mathrm{y}}(E_{\mathrm{nr}}) = \frac{E_{\mathrm{nr}} q_{\mathrm{nc}}(E_{\mathrm{nr}})}{W} \times \frac{Q}{Q_0}(E_{\mathrm{nr}}) \times \frac{1}{E_{\mathrm{nr}}} = \frac{q_{\mathrm{nc}}(E_{\mathrm{nr}})}{W} \times \frac{Q}{Q_0}(E_{\mathrm{nr}}) \ . \tag{5.4}$$

Before calculating the ionization yield, we have to identify the left free parameter K_2 and K_3 in Eq. (4.7). Our goal is to quantitatively describe the electric field dependence of the recombination rate for nuclear recoils already observed, and then predict the energy dependence of the ionization yield for nuclear recoils in liquid xenon. Therefore, we first fit K_2 and K_3 to the experimentally measured electric-field dependence of the ionization yield in liquid xenon for 56.5 keV nuclear recoils [2]. The charges collected is from Fig. 4 in Ref. [2], the number of the total charges produced is re-calculated in our work from $Q_0 = E_{\rm nr} q_{\rm nc}(E_{\rm nr})/W$, where $q_{\rm nc}$ is calculated using the computer program and the electronic stopping power we discussed in previous sections, and $W = 9.76$ eV is measured by Seguinot *et al.* in Ref. [3]. The nuclear stopping power $(dE/dx)_{\rm ncl}$ used is from Ref. [4]. We obtain from the fit that $K_2 = 14.755$ when the unit for E_d is kV/cm, and $K_3 = 0.004$ MeV^{-1}·g·cm^{-2}. The experimental data and the fit curve from the generalized Thomas-Imel model are shown in Fig. 5.3.

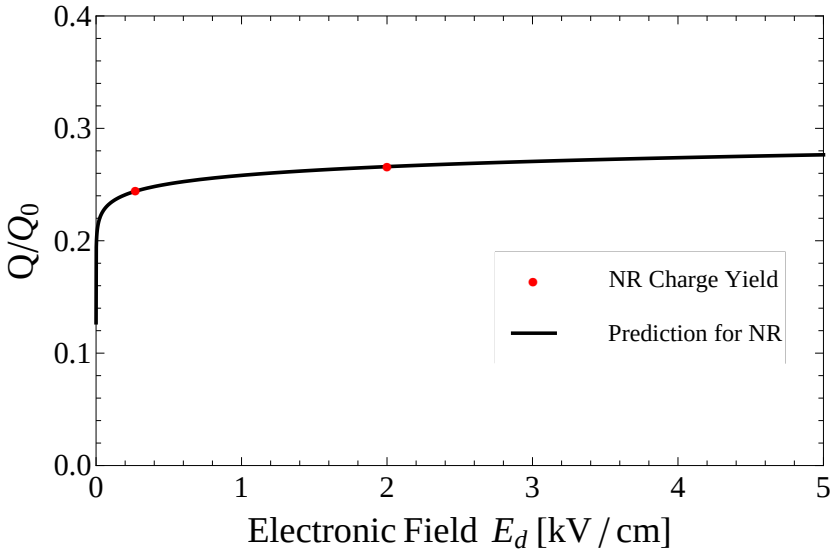

FIGURE 5.3: Reproduction of electric field dependence of the ionization yield efficiency in liquid xenon from 56.5 keV nuclear recoils (NR). The charges collected is from Fig. 4 in Ref. [2], the number of the total charges produced is calculated from $Q_0 = E_{\rm nr} q_{\rm nc}(E_{\rm nr})/W$, where $q_{\rm nc}$ is from this thesis, and $W = 9.76$ eV is measured by Seguinot *et al.* in Ref. [3]. The nuclear stopping power $(dE/dx)_{\rm ncl}$ used is from Ref. [4].

Using the fitted free parameters, we can predict the energy dependence of the ionization for nuclear recoils. The results for two electric fields, 2 kV/cm and 0.27 kV/cm are shown in Fig. 5.4. As the recoil energy gets lower, the density of the ions also decreases, the recombination effect becomes less important. In this case, the ionization efficiency increase.

We see this trend clearly starting from 40 keV. It reaches 100% at zero recoil energy. Again, the electric field dependence of the ionization efficiency is small in the nuclear recoils.

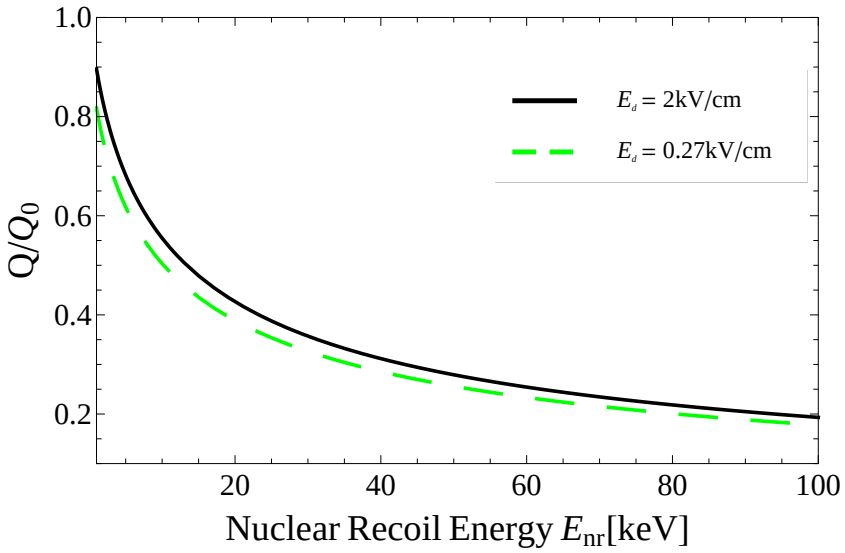

FIGURE 5.4: Energy dependence of the ionization yield efficiency, Q/Q_0, in liquid xenon under external electric fields 2 kV/cm (solid black curve) and 0.27 kV/cm (green dashed curve) for nuclear recoils. We can see the ionization yield for nuclear recoils in liquid xenon depends on electric field weakly.

Combining the total electronic energy dissipation $\eta(E_{\rm nr})$, W-value in Ref. [3] with the generalized Thomas-Imel model for electron-ions recombination in previous section, we can predict the ionization yield for nuclear recoils in liquid xenon detector using Eq. (5.4). The energy dependence of ionization yields $\mathcal{Q}_{\rm y}$ are shown as the black solid curve in Fig. 5.5, in the presence of a 2 kV/cm external electric field.

Along with our prediction, we have also shown the experimental data from different measurements: The brown triangles are from Yale group [19]; The blue squares are the result from the Columbia group measurement [2], from which our free parameters are fitted to the 56.5 keV data; The purple circles are from the Case group [2]; The magenta diamonds are from [18] and the red six-point-stars are from the XENON100 collaboration with mono-energy neutron and broad spectrum neutron sources [46]. Our prediction is in good agreement with the most recent data within experimental uncertainties.

The important feature in our result is that the ionization yield increases with decreasing energy, and reaches a maximum value at the recoiling energy in 2∼3 keV region. This maximum is produced by the increasing ionization efficiency and decreasing electronic energy

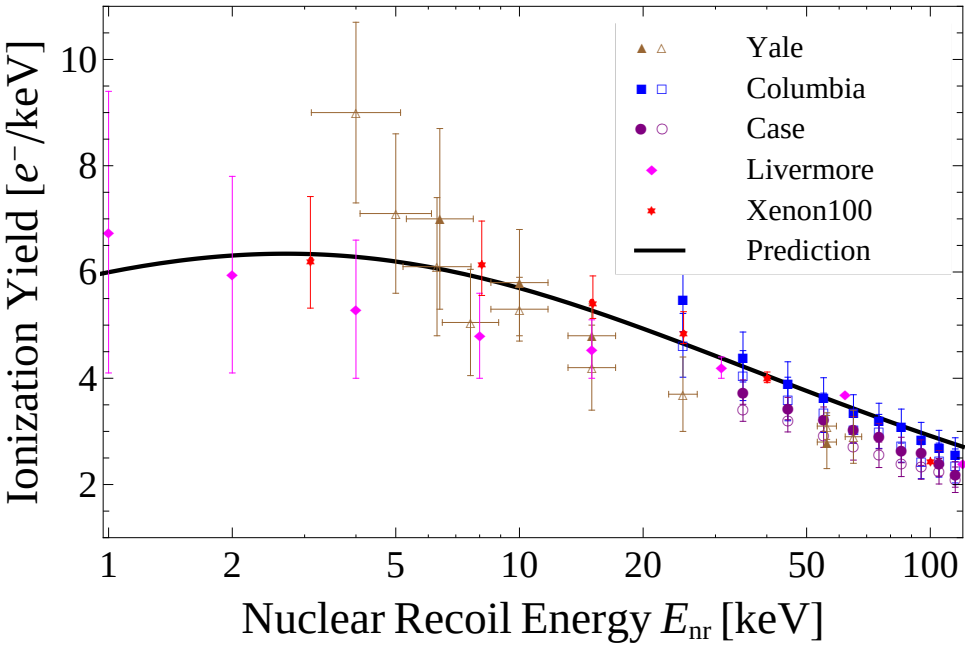

FIGURE 5.5: Energy dependence of the ionization yield, $\mathcal{Q}_y$, obtained from the generalized Thomas-Imel Model, compares with the available experimental data. Here, we use the Lindhard factor calculated in this thesis to evaluate the fraction of energy given to electrons and W-value 9.76 eV measured by Seguinot *et al.* in Ref. [3] to calculate the total charges produced.

dissipation at low recoil energy. It will be very interesting to test this prediction experimentally. Since the scintillation efficiency rapidly decreases with decreasing energy, particularly when less than 3 keV, the anti-correlation behavior of ionization yield helps to lower the low-energy threshold of liquid xenon detectors.

5.3 Discussion on the Theoretical Model

In this thesis, we have made a first realistic study of scintillation efficiency and ionization yield for the low-energy nuclear recoils in liquid xenon. The study has been motivated by the direct WIMP dark matter detection using liquid xenon as a detection medium. While the study is not completely *ab initio*, it represents the state-of-the-art theoretical considerations. This calculation only use four input parameters: screened Coulomb potential, spatial distribution of xenon atom, thermal energy and electronic stopping power in low-energy region, to calculate $\eta(E_{nr})$ hence q_{nc}. Except for the electronic stopping power, the other three parameters are undisputed.

The predicted results compare favorably with the data from neutron scattering, but differs somewhat from the Monte Carlo fitting to the broad-spectrum neutron data [44, 45]. The result for $\mathcal{L}_{\rm eff}$ suggests a rapid drop when the recoiling energy comes below 3 keV where authors have pointed out the liquid xenon scintillation response should drop steadily at low-energy which is a general feature that is independent of many details of the study. The result for $\mathcal{Q}_{\rm y}$ increases with the decreasing of the recoiling energy and reaches the maximum value at 2$\sim$3 keV, which may be examined by experiment in the future. Using the predicted $\mathcal{Q}_{\rm y}$ to re-construct the original nuclear recoil energy scale can lower the energy threshold for nuclear recoils to $\sim$1 keV for two-phase liquid xenon detectors. In one word, experimental physicist can potentially used either $\mathcal{Q}_{\rm y}$ or $\mathcal{L}_{\rm eff}$ independently or both $\mathcal{Q}_{\rm y}$ and $\mathcal{L}_{\rm eff}$ to determine the energy scale of the nuclear recoils.

There are a number of theoretical inputs which can be improved in the future to make the calculation more robust. The absolute value of the electronic stopping power used in the program has big impact on the accuracy of the result. Currently, almost every author uses the velocity proportional electronic stopping power as theoretical prediction. However, there are two major uncertainties. Firstly, the proportionality constant between the electronic stopping power and the velocity of the projectile particle is unknown in extremely low energy region. Theories, such as L-S theory or B-S theory, cannot get same results. Additionally, the theoretical predictions are much larger than the existing experimental measured data for liquid xenon. Secondly, based on the experimental results in Ref. [1], the electronic stopping power seems to drop more rapidly in the measured energy region (40 keV to 200 keV). By fitting the experimental data, the electronic stopping power seems to be proportional to $E^{0.84}$ instead of $E^{0.5}$ as predicted theoretically, where E is the kinetic energy of the projectile particle. In this work, we use the compromise by extrapolate to extremely low energy region from the experimental measured data.

Another uncertainty regarding this work lies in the binary collision approximation used in the program. As we know, the real problem with low energies is so complicate that the ion does not only have one binary collision, i.e. hitting just one atom at a time, but actually interacts with many atoms, who all move as it approaches and interact collectively. To get a more accurate result, one needs to use some methods such as molecular dynamics, which treat the collisions as many-body interaction. Currently, it is beyond the scope mentioned in this work.

For the ionization yield, we want to emphasize that the free parameters in our model are fitted to the existing experimentally measured ionization yield at 56.5 keV and extrapolated to low-energy region. So even though the total charges produced by nuclear recoils is very important to calculate the final ionization yield, it does not really count so much since we may use different fitting parameters to ensure the predicted ionization yield reliable in the generalized Thomas-Imel box model which gives a solid prediction for the trend of Q/Q_0.

Bibliography

[1] A. Fukuda. Srim - the stopping and range of ions in matter (2010). *J. Phys. B: At. Mol. Opt. Phys*, 14:4533, 1981.

[2] XENON100 Collaboration. Simultaneous measurement of ionization and scintillation from nuclear recoils in liquid xenon for a dark matter experiment. *Phys. Rev. Lett.*, 97: 081302, 2006.

[3] J. Seguinot et al. Liquid xenon ionization and scintillation studies for a totally active-vector electromagnetic calorimeter. *Nucl. Instr. and Meth. A*, 323:583–600, 1992.

[4] J. F. Ziegler et al. Srim - the stopping and range of ions in matter (2010). *Nucl. Instrum. Meth. B*, 268:1818, 2010.

[5] P. Salucci M. Persic and F. Stel. The universal rotation curve of spiral galaxies: 1. the dark matter connection. *Mon. Not. Roy. Astron. Soc.*, 281:27, 1996.

[6] A. Refregier. Weak gravitational lensing by large-scale structure. *Ann. Rev. Astron. Astrophys.*, 41:645–668, 2003.

[7] D. N. Spergel et al. Wilkinson microwave anisotropy probe (wmap) three year results: Implications for cosmology. *Astrophys. J. Suppl.*, 170:377, 2007.

[8] A. G. Riess et al. Observational evidence from supernovae for an accelerating universe and a cosmological constant. *The Astronomical Journal*, 116.3:1009, 1998.

[9] S. Perlmutter et al. Measurements of ω and λ from 42 high-redshift supernovae. *The Astrophysical Journal*, 517.2:565, 1999.

[10] F. Zwicky. Die rotverschiebung von extragalaktischen nebeln. *Helvetica Physica Acta*, 6:110–127, 1933.

[11] D. Hooper G. Bertone and J. Silk. *Phys. Rep.*, 405:279, 2005.

[12] WMAP Collaboration. *Astrophys. J. Suppl. Ser.*, 192:14, 2011.

[13] H.C. Cheng et al. *Phys. Rev. Lett.*, 89:211301, 2002.

[14] A. Bottino et al. *Phys. Rev. D*, 69:037302, 2004.

[15] J. Ellis et al. *Phys. Rev. D*, 71:095007, 2005.

[16] D. Akimov. Techniques and results for the direct detection of dark matter. *Nucl. Instrum. Meth A*, 628:50–58, 2011.

[17] XENON100 Collaboration. Dark matter results from 225 live days of xenon100 data. *Phys. Rev. Lett.*, 109:181301, 2012.

[18] P. Sorensen et al. *arXiv:1011.6439 [astro-ph.IM]*, .

[19] A. Manzur et al. Scintillation efficiency and ionization yield of liquid xenon for monoenergetic nuclear recoils down to 4 kev. *Phys. Rev. C*, 81:025808, 2010.

[20] D. Hooper G. Bertone and J. Silk. Particle dark matter: Evidence, candidates and constraints. *Physics Reports*, 405:279–390, 2005.

[21] J. P. Ostriker et al. *Astrophys. J. Letters*, .

[22] J. Einasto et al. Dynamic evidence on massive coronas of galaxies. *Nature*, 250:309–310, 1974.

[23] S. M. Faber and J. S. Gallagher. Masses and mass-to-light ratios of galaxies. *Ann. Rev. Astron. and Astrophys.*, 17:135–187, 1974.

[24] Y. Sofue and V. Rubin. Rotation curves of spiral galaxies. *Ann. Rev. Astron. and Astrophys.*, 39:137–174, 2001.

[25] M. Bartelmann and P. Schneider. Weak gravitational lensing. *Physics Reports*, 340: 291–472, 2001.

[26] A. Gonzalez D. Clowe and M. Markevitch. Weak-lensing mass reconstruction of the interacting cluster 1e 0657-558 direct evidence for the existence of dark matter. *The Astrophysical Journal*, 604:596, 2004.

[27] J. R. Primack G. R. Blumenthal, S. M. Faber and M. J. Rees. Formation of galaxies and large-scale structure with cold dark matter. *Nature*, 311:517–52, 1984.

[28] R. Battesti et al. Axion searches in the past, at present, and in the near future. *Lecture Notes in Physics*, 741:199–237, 2008.

[29] M. Kamionkowskib G. Jungmana and K. Griestd. Supersymmetric dark matter. *Physics Report*, 267:195–373, 1996.

[30] M. W. Goodman and E. Witten. Detectability of certain dark-matter candidates. *Phys. Rev. D*, 31:3059–3063, 1996.

[31] J. D. Lewin and P. F. Smith. Review of mathematics, numerical factors, and corrections for dark matter experiments based on elastic nuclear recoil. *Astropar. Phys.*, 6:87, 1996.

[32] E. Aprile and T. Doke. Liquid xenon detectors for particle physics and astrophysics. *Rev. Mod. Phys.*, 82:2053–2097, 2010.

[33] A. I. Bolozdynya. Two-phase emission detectors and their applications. *Nucl. Instrum. Meth A*, 422:314–320, 1999.

[34] J. Kikuchi M. Yamashita, T. Doke and S. Suzuki. Double phase (liquid/gas) xenon scintillation detector for wimps direct search. *Astropart. Phys.*, 20:79–84, 2003.

[35] UKDMC Collaboration. Status of zeplin ii and zeplin iv study. *Nucl. Phys. B*, 124: 229–232, 2003.

[36] XENON100 Collaboration. The xenon100 dark matter experiment. *Astropart. Phys.*, 35:573, 2012.

[37] X. Ji A. Tan H. Gong, K. L. Giboni and L. Zhao. The cryogenic system for the panda-x dark matter search experiment. *JINST*, 8:01002, 2013.

[38] XENON100 Collaboration. New measurement of the relative scintillation efficiency of xenon nuclear recoils below 10 kev. *Phys. Rev. C*, 79:045807, 2009.

[39] G. Plante et al. New measurement of the scintillation efficiency of low-energy nuclear recoils in liquid xenon. *Phys. Rev. C*, 84:045805, 2011.

[40] DAMA Collaboration. First results from dama/libra and the combined results with dama/nai. *Eur. Phys. J. C*, 56:333, 2008.

[41] CoGeNT Collaboration. Results from a search for light-mass dark matter with a p-type point contact germanium detector. *Phys. Rev. Lett.*, 106:131301, 2011.

[42] CDMS Collaboration. *arXiv:1304.4279[hep-ex]*, .

[43] J. I. Collar and D. N. McKinsey. *arXiv:1005.0838 [astro-ph.CO]*.

[44] V. N. Lebedenko et al. Result from the first science run of the zeplin-iii dark matter search experiment. *Phys. Rev. D*, 80:052010, 2009.

[45] P. Sorensen et al. The scintillation and ionization yield of liquid xenon for nuclear recoils. *Nucl. Instrum. Meth. A*, 601:339, 2009.

[46] XENON100 Collaboration. *arXiv:1304.1427*, .

[47] J. Lindhard et al. Integral equations governing radiation effects.(notes on atomic collisions, iii). *Kgl. Danske Videnskab., Selskab. Mat. Fys. Medd.*, 33:10, 1963.

[48] A. Hitachi. Properties of liquid xenon scintillation for dark matter searches. *Astropart. Phys.*, 24:247, 2005.

[49] D. M. Mei et al. A model of nuclear recoil scintillation efficiency in noble liquids. *Astropart. Phys.*, 30:12, 2008.

[50] F. Bezrukov et al. Interplay between scintillation and ionization in liquid xenon dark matter searches. *Astropart. Phys.*, 35:119, 2011.

[51] S. Agostinelliae et al. Geant4-a simulation toolkit. *Nucl. Instrum. and Meth. A*, 506: 250, 2003.

[52] G. F. Knoll. *Radiation detection and measurement*. Wiley. com, 2010.

[53] K. Wamba. *Ph.D thesis, Stanford University*.

[54] L. D. Landau and E. M. Lifshitz. *Mechanics*. Butterworth-Heinemann Ltd Press, Oxford, U.K., 1976.

[55] J. Eichler. *Lectures on ion-atom collisions: From nonrelativistic to relativistic velocities*. Elsevier Science, 2005.

[56] D. J. Ficenec et al. Observation of electronic excitation by extremely slow protons with applications to the detection of supermassive charged particles. *Phys. Rev. D.*, 36:311, 1987.

[57] J. D. Jackson. *Classical Electrodynamics (3rd Edition)*. John Wiley Sons Inc., 1999.

[58] N. Bohr. *Philos. Mag.*, page 10.

[59] P. Sigmund and A. Schinner. Binary theory of electronic stopping. *Nucl. Instrum. Meth. B*, 195:64, 2002.

[60] W. Brandt and M. Kitagawa. Effective stopping-power charges of swift ions in condensed matter. *Phys. Rev. B*, 25:5631, 1982.

[61] P. M. Echenique et al. Nonlinear stopping power of an electron gas for slow ions. *Phys. Rev. A*, 33:897, 1986.

[62] J. Lindhard et al. On the properties of a gas of charged particles. *Kgl. Danske Videnskab., Selskab. Mat. Fys. Medd.*, 28:8, 1954.

[63] J. Lindhard and M. Scharff. Energy dissipation by ions in the kev region. *Phys. Rev.*, 124:128, 1961.

[64] I. S. Tilinin. Quasiclassical expression for inelastic energy losses in atomic particle collisions below the bohr velocity. *Phys. Rev. A*, 51:3058, 1995.

[65] N. R. Arista. Energy loss of ions in solids: Non-linear calculations for slow and swift ions. *Nucl. Instr. and Meth. B*, 195:91–105, 2002.

[66] H. Geissel Y. Laichter and N. H. Shafrir. On the nuclear charge and atomic mass of attenuated mean fission fragments. *Nucl. Instrum. Meth.*, 194:45–50, 1982.

[67] P. Bauer et al. Phase effect in the energy loss of h projectiles in zn targets: Experimental evidence and theoretical explanation. *Phys. Rev. Lett.*, 69:1137, 1992.

[68] A. Arnau et al. Phase effect in the energy loss of hydrogen projectiles in zinc targets. *Phys. Rev. B*, 49:6470, 1994.

[69] M. Bergsmann et al. Phase effect in stopping of h ions in mg. *Phys. Rev. B*, 62:3153, 2000.

[70] R. L. Platzman. Total ionization in gases by high-energy particles: An appraisal of our understanding. *Int. J. Appl. Radiat. Is.*, 10:116, 1961.

[71] T. Takahashi et al. Average energy expended per ion pair in liquid xenon. *Phys. Rev. A*, 12:1771, 1975.

[72] T. Doke et al. Absolute scintillation yields in liquid argon and xenon for various particles. *Jpn. J. Appl. Phys.*, 41:1538, 2002.

[73] E. Aprile et al. Search for light dark matter in xenon10 data. *Phys. Rev. Lett.*, 107: 051301, 2011.

[74] E. Aprile et al. Observation of anti-correlation between scintillation and ionization for mev gamma-rays in liquid xenon. *Phys. Rev. B*, 76:014115, 2007.

[75] P. Sorensen. A coherent understanding of low-energy nuclear recoils in liquid xenon. *J. Cosmol. Astropart.*, 09:033, 2010.

[76] P. Langevin. Recombinaison et mobilites des ions dans les gaz. *Ann. Chim. Phys.*, 28: 433, 2007.

[77] L. Onsager. Initial recombination of ions. *Phys. Rev.*, 54:554, 1938.

[78] G. Jaffe. On the theory of recombination. *Phys. Rev.*, 58:968, 1940.

[79] H. A. Kramers. On a modification of jaffe's theory of column-ionization. *Physica.*, 18: 665, 1952.

[80] J. Thomas and D. A. Imel. Recombination of electron-ion pairs in liquid argon and liquid xenon. *Phys. Rev. A*, 36:614, 1987.

[81] A. Mozumder. Free-ion yield and electron-ion recombination rate in liquid xenon. *Chem. Phys. L*, 245:359, 1995.

[82] S. P. Chabod. Charge collection efficiency in ionization chambers operating in the recombination and saturation regimes. *Nucl. Instr. and Meth. A*, 604:632, 2009.

[83] S. Howe L. S. Miller and W. E. Spear. Charge transport in solid and liquid ar, kr, and xe. *Phys. Rev.*, 166:871, 1968.

[84] T. Doke et al. Let dependence of scintillation yields in liquid argon. *Nucl. Instr. and Meth. A*, 269:291, 1988.

[85] V. Chepel and A. Henrique. Liquid noble gas detectors for low energy particle physics. *J. of Instr.*, 8:04001, 2013.

[86] C. E. Dahl. *Ph.D. thesis, Princeton University.*

[87] M. G. Robinson and G. R. Freeman. X-radiolysis ion yields and electron ranges in liquid xenon, krypton, and argon: Effect of electric field strength. *Can. J. Chem.*, 51:641–649, 1973.

[88] S. Konno and S. Kobayashi. The w-value in liquid xenon is found to be 17.3 ev. *Sci. Pap. Inst. Phys. Chem. Res. (Jap.) V.*, 67:57–62, 1973.

[89] T. Takahashi et al. The average energies, w, required to form an ion pair in liquefied rare gases. *J. Phys. C*, 7:230, 1974.

[90] Sam S-S. Huang and G. R. Freeman. Effect of density on the total ionization yields in x-irradiated argon, krypton, and xenon. *Can. J. Chem.*, 55:1838–1846, 1977.

[91] E. Aprile et al. Performance of a liquid xenon ionization chamber irradiated with electrons and gamma-rays. *Nucl. Instr. and Meth. A*, 302:177–185, 1991.

[92] M. Miyajima et al. Comments on liquid xenon ionization and scintillation studies for a totally active-vector electromagnetic calorimeter. *Nucl. Instr. and Meth. A*, 352:548–551, 1995.

[93] J. Seguinot et al. Reply to comments on liquid xenon ionization and scintillation studies for a totally active-vector electromagnetic calorimeter. *Nucl. Instr. and Meth. A*, 361: 623–624, 1995.